Functional Imaging Techniques for Liver Kinetic Modeling

by

Chen Sirong

Department of Electronic and Information Engineering
The Hong Kong Polytechnic University

A thesis submitted in partial fulfillment of the requirements for the Degree of Doctor of Philosophy

July 2005

CERTIFICATE OF ORIGINALITY

I hereby declare that this thesis is my own work and that, to the best of my knowledge and belief, it reproduces no material previously published or written, nor material that has been accepted for the award of any other degree or diploma, except where due acknowledgement has been made in the text.

_____(Signed)

_____Chen Sirong_____(Name of student)

Abstract

Positron emission tomography (PET) has been proven very promising for the evaluation of malignant tumors. However, 40-50% of hepatocellular carcinoma (HCC), one of the most common malignancies worldwide, could not be detected by the well-established ^{18}F-fluorodeoxyglucose (FDG) PET. Recent research had demonstrated that ^{11}C-acetate (ACT) was a complementary tracer to FDG and these 2 tracers together could maximize the detection accuracy of this tumor. Quantitative functional imaging techniques were, therefore, conducted to further characterize the underlying kinetic basis of this tracer in the detection of HCC. To describe the ^{11}C-acetate molecular kinetic characteristics in liver, a three-compartment model with dual-input function was proposed and a new physiological parameter called the "local hepatic metabolic rate-constant of acetate (*LHMRAct*)" was introduced. Preliminary results revealed that the *LHMRAct* of HCC was significantly higher than that of the non-tumor liver tissue. This tracer kinetic modeling technique provided the first quantitative and kinetic evidence that ^{11}C-acetate was indeed metabolically incorporated in certain types of HCC.

Since in real pathology, both tumor and non-tumor liver tissue can be heterogeneous in the distribution and proportion of the two hepatic blood supplies: hepatic artery (HA) and portal vein (PV). To further improve the accuracy of quantitative analysis, the individual proportion of HA/PV in different

regions of interest (ROIs) was studied by investigating another parameter called the "relative portal venous contribution to the hepatic blood flow (a_v)". Results showed that the new model structure could provide better characterization of the ^{11}C-acetate kinetic behavior in liver. The analysis was also able to provide a better understanding of the blood supply mechanism in the liver, proposing that the new parameter a_v, as a quantitatively derived vascular factor, might also provide useful diagnostic information for the detection of HCC.

In the previous quantitative studies, all the individual model parameters were estimated by the weighted nonlinear least squares (NLS) algorithm. However, relatively large number of parameters needs to be estimated, which is a very challenging task. The computational time-complexity is high and some estimates are not quite reliable or even fail to convergence, which limits its application in clinical environment and is not practical for the generation of parametric images. In addition, liver system modeling with dual-input function is very different from the widespread single-input biomedical system modeling. Therefore, most of the currently developed estimation techniques are not applicable for the dynamic ^{11}C-acetate PET images in liver. Several novel parameter estimation techniques: graphed NLS (GNLS), dual-input-generalized linear least squares (D-I-GLLS) and graphed dual-input GLLS (GDGLLS) algorithms were presented. When compared with the standard NLS fitting procedure, these novel methods provide better and practical ways for the clinical parameter estimation. In addition, GNLS and GDGLLS are extremely powerful for the estimation of the two potential HCC indicators: *LHMRAct* and a_v in the noisy clinical environment.

For the quantification of the dual-input liver system, both time-activity curves (TACs) of HA and PV are desired for the model input function. However, directly measuring them by the widely adopted blood sampling or cannulation procedure is invasive. Moreover, accurate measuring the TAC of PV in the human liver is difficult to achieve, as the tracer arriving at the PV is delayed and dispersed, and furthermore, the TAC of PV is considerably contaminated by the surrounding liver tissue, which makes it virtually impractical to differentiate the PV curve by the currently developed techniques. To noninvasively and efficiently access the portal venous blood flow, the effectiveness of modeling the dual hepatic blood supply was investigated. The fitting results revealed that the proposed double modeling technique could successfully account for the hepatic dual-input. Therefore, the tedious or even impractical task of measuring the PV curve could be avoided, which is very valuable for providing the functional parametric images to evaluate HCC.

To perform the quantitative analysis, ROIs of both blood vessels and target regions need to be extracted. Manual placement of ROIs is subject to operator's skill and time-consuming. Furthermore, the small size of some ROIs makes the task even more difficult. Two segmentation approaches based on cluster analysis were proposed to segment the dynamic ^{11}C-acetate PET images in liver automatically. The curves extracted from the segmented ROIs were then fitted to the presented ^{11}C-acetate liver models. With the obtainment of the HCC indicators, this devastating tumor can, therefore, be detected automatically.

Author's Publications

The following technical papers are based on the results generated from this work.

Referred Journal Publications (full paper)

1. **Sirong Chen** and Dagan Feng, "Non-Invasive Quantification of the Differential Portal and Arterial Contribution to the Liver Blood Supply from PET Measurements Using ^{11}C-Acetate Kinetic Model", *IEEE Transactions on Biomedical Engineering*, Vol. 51, No. 9: pp1579-1585, 2004.
2. **Sirong Chen**, Chilai Ho, Dagan Feng, and Zheru Chi, "Tracer Kinetic Modeling of ^{11}C-Acetate Applied in the Liver with Positron Emission Tomography", *IEEE Transactions on Medical Imaging*, Vol. 23, No. 4: pp426-432, 2004.

Referred Journal Publications (communication papers/ abstracts)

1. **Sirong Chen** and Dagan Feng, "A Novel Technique for the Evaluation of Hepatocellular Carcinoma", *The Journal of Nuclear Medicine*, Vol. 45 (suppl.), No. 5: pp403, 2004.
2. **Sirong Chen**, Chilai Ho, and Dagan Feng, "Identifiability Analysis of the Differential Portal and Arterial Contribution to the Vascular Input Function of ^{11}C-Acetate Kinetic Model in Liver", *The Journal of Nuclear Medicine*, Vol. 44 (suppl.), No. 5: pp252-253, 2003.
3. **Sirong Chen**, Chilai Ho, Dagan Feng, and Zheru Chi, "Kinetic Modeling of ^{11}C-Acetate in Hepatocellular Carcinoma", *The Journal of Nuclear Medicine*, Vol. 43 (suppl.), No. 5: pp205, 2002.

Referred Conference Proceedings Publications

1. **Sirong Chen** and Dagan Feng, "New Parameter Estimation Approaches for Dual-Input ^{11}C-Acetate Liver Kinetic Model", *16th IFAC world congress*, Prague, Czech Republic, 4-8 July 2005 (accepted).
2. **Sirong Chen**, Longkin Wong, and Dagan Feng, "A New Automatic Detection Approach for Hepatocellular Carcinoma Using ^{11}C-Acetate Positron Emission Tomography", *Proceedings of IEEE International Conference on Image Processing*, Vol. 1**:** pp1065-1068, Barcelona, Spain, 14-17 Sep. 2003.

Submitted to Journal for Review

1. **Sirong Chen** and Dagan Feng, "Use of Modeling the Dual Hepatic Blood Supply for Liver Studies with Dynamic ^{11}C-Acetate PET", submitted to *IEEE Transactions on Nuclear Science*, (08/05).
2. **Sirong Chen** and Dagan Feng, "Novel Parameter Estimation Methods for ^{11}C-Acetate Dual-Input Liver Model with Dynamic PET", 2nd revision resubmitted to *IEEE Transactions on Biomedical Engineering*, (07/05).
3. **Sirong Chen**, Chilai Ho, and Dagan Feng, "Functional Imaging Techniques for the Evaluation of Hepatocellular Carcinoma Using Dynamic ^{11}C-Acetate PET Imaging", submitted to *Current Medical Imaging Reviews* (07/05).
4. Hon-Chit Choi, **Sirong Chen**, Dagan Feng, and Koon-Poog Wong, "Fast Parametric Imaging Algorithm for Dual-Input Biomedical System Parameter Estimation", submitted to *Computer Methods and Programs in Biomedicine*, (in revision).

Acknowledgements

I would like to express my most sincere thanks and gratitude to my supervisor, Prof. David Dagan Feng, for his excellent guidance and generous support throughout my PhD study. I would also like to thank Dr. Garrett Chilai Ho, director of the Department of Nuclear Medicine & Positron Emission Tomography of Hong Kong Sanatorium & Hospital, for providing clinical application advice and valuable clinical data; and to thank his colleagues, not only for their kindly assistance and support, but also for the constructive advice and fruitful discussion. I am also very grateful to my co-supervisor, Dr. Zheru Chi for his helpful advice and encouragement during my PhD study. My PhD study would have never been completed without their supervision. It is a rare privilege and a great honor for me to work with them. Both their professional advice and plentiful experience help me to further improve myself.

I also acknowledge my friends and colleagues for their advice, suggestion, support and friendship, in particular, Dr. Koon-Poon Wong, Dr. Weidong, Cai, Dr. Linfeng Wen, Mr. Hon-Chit Choi and Mr. Longkin Wong. I benefited greatly from the detailed discussion with them. In addition, I wish to thank the staffs of the Center for Multimedia Signal Processing and General Office in the Department of Electronic and Information Engineering for their support. Thanks also go to the School of Information Technologies, the University of Sydney, for

providing excellent resources and facilities during the period I worked as a Visiting Scholar.

Last but not least, I would like to take this opportunity to especially thank my parents. Without their continuing support and encouragement, this study would never have been possible.

Sirong Chen

July, 2005

Hong Kong

Statements of Originality

The following contributions reported in this thesis are claimed to be original.

1. A new compartment model consisting of three compartments four parameters with dual-input function was proposed to describe the kinetic characteristics of ^{11}C-acetate in hepatocellular carcinoma (HCC) and non-tumor liver tissue. Clinical dynamic PET images of ^{11}C-acetate in liver were used to test the models. The forward clearance rate $K = K_1 * k_3/(k_2+k_3)$ was estimated and defined as a new physiological parameter called the *local hepatic metabolic rate-constant of acetate* (*LHMRAct*) to different HCC from the non-tumor liver tissue. Preliminary results demonstrate that the *LHMRAct* of HCC is significantly higher than that of the non-tumor liver tissue. The model parameters could provide quantitative evidence and understanding on the kinetic basis of ^{11}C-acetate for its potential role in the imaging of HCC using PET.

2. A new model structure with an extra parameter included in the model dual-input function to account for the relative PV/HA contribution to the liver blood flow was presented. This new model structure and modeling technique can further improve the accuracy of quantitative analysis, provide a better understanding of the blood supply mechanism in liver and useful diagnostic information for detection of HCC, particularly in

situations when confounding hyperaemic variables such as dysplastic and regenerative nodules coexist in the setting of severe cirrhosis.

3. A dual-input-generalized linear least squares (D-I-GLLS) algorithm was proposed to identify the parameters of ^{11}C-acetate model with dual hepatic blood supply system. The quantitative analysis results suggest that the proposed technique could provide comparable reliability of the parameter estimation with NLS fitting and accurately identify the parameter in the dual-input function of ^{11}C-acetate liver model. This method may be potentially applicable to other dual-input biomedical system parameter estimation as well.

4. Two novel parameter estimation techniques: graphed NLS (GNLS) and graphed dual-input generalized linear least squares (GDGLLS) algorithms were presented for ^{11}C-acetate dual-input liver model. Clinical and simulated data were utilized to test the proposed algorithms by a systematic statistical analysis. In comparison to the NLS fitting procedure, these two novel methods achieve better estimation reliability and are computationally efficient, which provides better and practical ways for the clinical parameter estimation, and they are extremely powerful for the estimation of the two potential HCC indicators: *LHMRAct* and a_v in the noisy clinical environment.

5. To noninvasively and efficiently access the portal venous blood flow, we investigated the effectiveness of modeling the dual hepatic blood supply

with dynamic ^{11}C-acetate PET. Clinical data fitting results reveal that the proposed double modeling technique could successfully account for the hepatic dual-input. Therefore, the tedious or even impractical task of measuring the PV curve could be avoided. In addition, this new model structure is very valuable for providing the functional parametric images to evaluate HCC in a much early stage.

6. Two segmentation approaches based on cluster analysis were adopted to segment the dynamic ^{11}C-acetate PET liver images to avoid manual placement of ROIs for ^{11}C-acetate PET quantitative analysis.

Table of Contents

List of Tables

List of Figures

Chapter 1 Introduction

1.1 Introduction

The last two decades have witnessed extraordinary innovation in medical imaging and its clinical significance in diagnosis and treatment of diseases is overwhelming. The medical imaging is often thought of visualization of anatomic structures and to evaluate malignant tumors it mostly emphasizes the relationship of structural changes in the body, as exemplified by detection of “masses” [1]. Indeed, x-ray computed tomography (CT) and magnetic resonance imaging (MRI) yield exquisitely detailed images of such changes which generally occur at the advanced stages of malignant tumors [2]. Up to the present day, the diagnosis and treatment of cancer have been primarily surgical. When a mass of an enlarged lymph node is detected somewhere in the body, immediate surgical attempts are made to remove it or to obtain a histological diagnosis by biopsy. Now things are changing, as we become increasingly able to characterize lesions by their molecular characteristics known as functional information by the use of medical imaging procedures as nuclear medicine.

We were taught that functional impairment precedes structural changes in all forms of human diseases and earlier detection and aggressive surgical treatment of a cancer would consistently lead to a better outcome for the patient. Nuclear medicine contributes significantly to the initial diagnosis of disease, assessment of response to therapy, and exploration of the natural history of disease, and is beginning to have an expanded role in therapy [3]. An area of the field of nuclear medicine with many applications and great potential is especially positron emission tomography (PET). The progression from the first experimental animal studies of ^{14}C-labeled deoxyglucose used to measure functional brain activity by means of postmortem autoradiography in the early 1970s to the application of *^{18}F-fluorodeoxyglucose* (FDG) PET on a routine clinical basis has been exhilarating for many diseases and physiologic evaluation, PET has shown itself to be superior to other imaging techniques [3]. Functional PET imaging with its unique capability of extracting quantitative physiological information from complex dynamic processes has opened a new window for scientific and biomedical research. It is well known that of all the existing imaging modalities, PET is the best instrumentation for absolute quantification of the functional/molecular status of the pathological and physiological systems of the human body. Based on this principle, PET has been documented by a significant amount of data in the literature for its ability to establish the diagnosis at a much earlier stage. Today, characterization of molecular processes in cancerous lesions by PET can additionally help to determine whether therapy should be aggressive or “watch and wait”. Furthermore, once active treatment is decided, PET imaging is increasingly used to determine the extent of the disease for treatment planning,

and when treatment has been undertaken, PET is used to monitor treatment effect and then to follow the patient, to look for signs of recurrence.

Over the past 20 years, PET has matured into a powerful tool to quantitatively study regional metabolism, blood flow *etc.* of brain, heart and some other organs. However, studies of liver metabolism have been limited, in spite of the key role of the liver in the regulation of the metabolism and the unique possibility of studying metabolism *in vivo* by positron-labeled substrates [4]. Hepatocellular carcinoma is the predominant type of primary liver cancer and the most common malignancy worldwide in males. It is especially prevalent in parts of Asia and Africa. In Hong Kong, HCC is the second most common cancer in men and the sixth in women. It constitutes 9.5% of all new cancer cases and 12.5% of all cancer deaths per year. The definitive diagnosis of hepatoma is by histopathology. However, biopsy is often considered invasive and not a recommended procedure in patients with advanced liver disease and coagulopathy. Therefore, noninvasive alternatives to needle biopsy are required. The conventional methods for investigation of hepatoma include diagnostic imaging procedures using ultrasonography (USG), CT and MRI, evaluating the structural changes in the body. In situations when the background hepatic parenchyma has severe cirrhosis, often intermixing with a variable degree of regenerative and dysplastic nodules, the diagnosis of HCC by these structural imaging modalities will be greatly limited.

HCC is curable by surgery or liver transplantation only if the tumor is small, but tumor recurrence and /or metastasis are the major problems. Surgery or liver

transplantation may not be possible in all cases, usually if the tumor is very large or has spread beyond the liver. For large tumors or cancer that has spread beyond the liver, all the currently adopted treatment options are not curative. Most cases of HCC are discovered late and less than 10% are cured with surgical resection. Therefore, curative treatment of this aggressive tumor may be only at potentially early stages.

The use of PET for the studying of liver diseases remains on cancer detection. It is well known that FDG is the most popular tracer for the measurement of malignancies due to the fact that cancer cells have a generally increased uptake of glucose. Therefore, most clinical PET scanning is performed with FDG as the radiotracer. However, 40-50% of HCC do not show increased FDG uptake. Therefore, innovative design of the tracer is desired for the evaluation of HCC. ^{11}C-labeled acetate traces the tricarboxylic acid cycle and has been shown to be closely correlated to oxidative metabolism and, thus, to be a marker of myocardial oxygen consumption [5]. Increasing number of clinical studies are performed with ^{11}C tracers in oncology. The study by Ho *et al.* [6], [7] using a dual-isotope PET protocol: FDG and ^{11}C-acetate, has suggested that the evaluation of HCC could be greatly aided by the introduction of ^{11}C-acetate. Dynamic data would potentially resolve the time-related characteristics of the tumor status from other nontumorous processes, which are “lumped” together during static imaging. Therefore, quantitative studies would become crucial for accurately applying functional imaging techniques for establishing diagnosis of HCC. A suitable compartment model for describing the tracer kinetics and understanding the tracer biochemical mechanism in liver and HCC is the premise

for this research. Computer-aided kinetic modeling can hopefully resolve the model-related functional parameters, which would provide a better understanding on and correlation with the variable histopathology of this devastating tumor. Intelligent approaches of model-based quantitative image analysis for computerized diagnosis would in addition improve the sensitivity and specificity of the radiological PET images.

In the following sections of this chapter, the general overview of PET, the principles of tracer kinetic modeling in PET and the parameter estimation techniques would be briefly described, followed by the introduction of the work which is to be presented in the subsequent chapters of this thesis.

1.2 Principles of Positron Emission Tomography Imaging

This section is designed to give the reader a general understanding of PET. PET is a noninvasive medical imaging technology that can generate high-resolution images of human and animal physiologic functions. Figure 1-1 is a photograph of ECAT EXAT clinical PET scanner. PET is used for a variety of clinical applications in oncology, neurology, and cardiology, but the principal clinical application of PET is in oncology [3] since many oncologic questions have been addressed and most elegantly answered by employing PET. Figure 1-2 displays a whole-body FDG image acquired on the GE Advance clinical PET

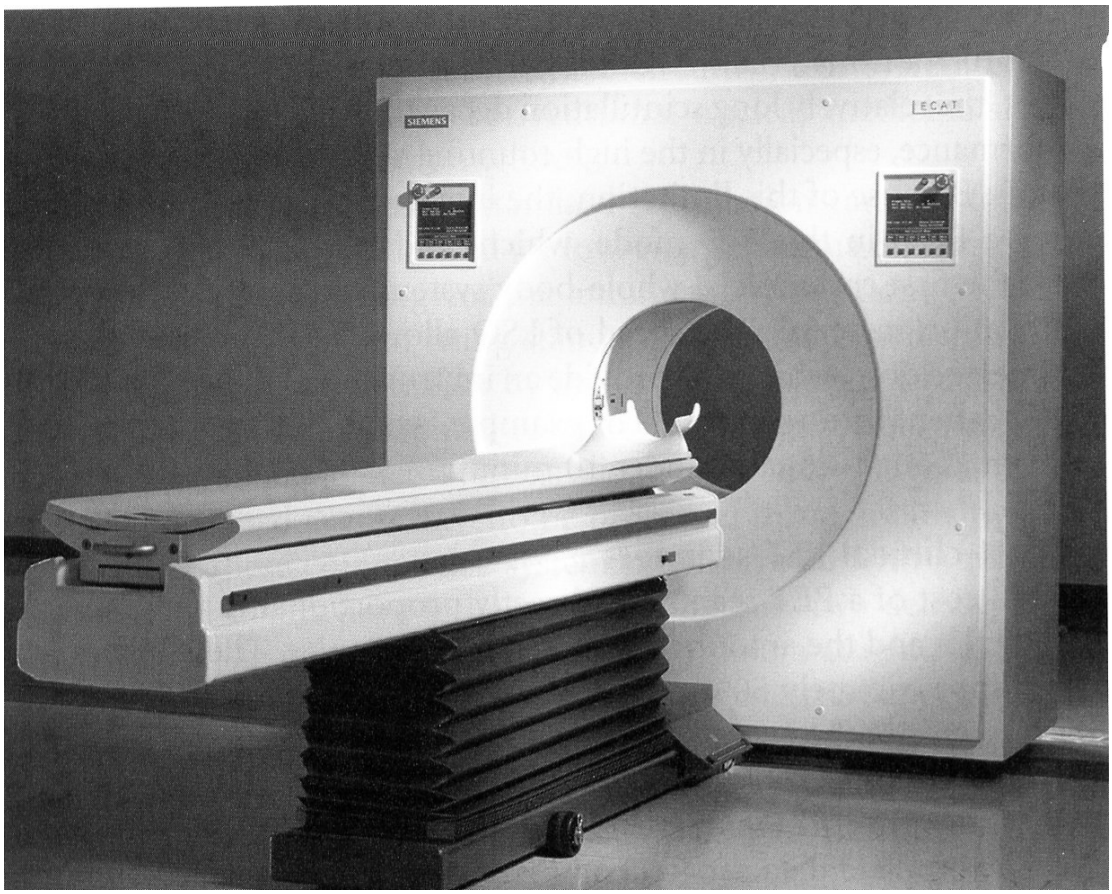

Figure 1-1: Photograph of ECAT EXACT clinical PET scanner (Courtesy of CTI Inc., Knoxville, TN.).

scanner. PET is a technique for measuring the concentrations of positron-emitting radioisotopes within the object by the use of external measurements of the radiation from these isotopes [8]. A PET study begins with the injection of inhalation of a positron-emitting radionuclide (tracer). The scan is begun to measure the distribution of tracers after a decay ranging from seconds to minutes to allow for transport to and uptake by the organ of interest. Positron-emitting radionuclides are used for imaging because of their unique tomographic capability and the availability of a group of metabolically important

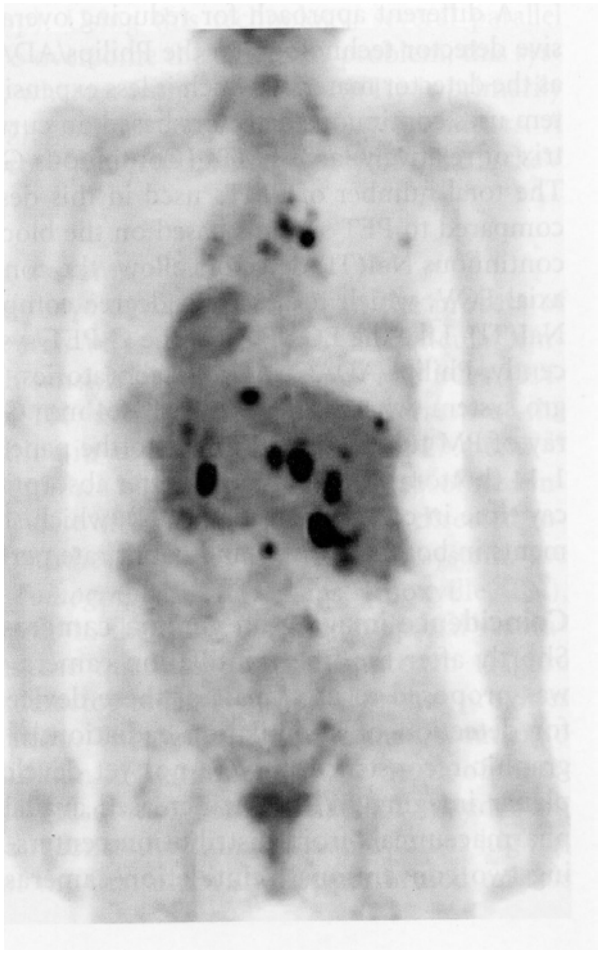

Figure 1-2: Whole-body FDG image acquired on the GE Advance clinical PET scanner (Courtesy of GE Medical Systems, Waukesha, WI.).

radionuclides [3]. The unique tomographic capability lies in the simultaneous emission of two back-to-back, 511-KeV gamma rays from a positron-labeled molecule and the tracer uptakes could be accurately quantified with its attenuation-correction. A PET scanner consists of a set of detectors that surround the object to be imaged and are designed to convert these high energy photons into an electrical signal that can be fed to subsequent electronics [9]. The signals are corrected for a number of factors and then reconstructed into a tomographic imaging using mathematical algorithms [9]. The medical importance of PET derives from the availability of many useful isotopes (^{11}C, ^{13}N, ^{15}O, ^{18}F), which

are essential elements of all living organisms and their physiological processes. Hence, tissue-specific and chemistry-specific tracers can be synthesized and injected into humans/animals to study the physiological functions of normal or pathological tissues *in vivo*. By taking a time sequence of images, the tissue concentration of the radiolabeled molecules as a function of time is measured, and with proper tracer kinetic modeling, the distribution of these positron-labeled compounds, as depicted by the tomographic images, may be converted into images of functional parameters such as metabolic rates, blood perfusion rates, and receptor densities [1].

1.2.1 Basic Physics of PET

The nucleus of an atom consists of two types of nucleons: protons and neutrons. If a nucleus has either an excess number of protons or neutrons, it is unstable and prone to radioactive decay, leading to a change in the number of protons or neutrons in the nucleus and a more stable configuration [9]. One common method by which nuclei with an excess of protons may decay is through *positron emission*. Radionuclides that decay predominantly by positron emission are preferred for PET imaging. When the radio-isotope decays, it emits a positron, which travels a short distance before annihilating with an electron, producing two high-energy (511 KeV) photons (gamma rays) propagating in nearly opposite directions, which was shown schematically in Figure 1-3. The movement of information from one place to another by means of electromagnetic radiation in the form of photons forms the basis of PET imaging. If two photons are detected within a short (about 10ns) timing window (the *coincidence timing window*), an

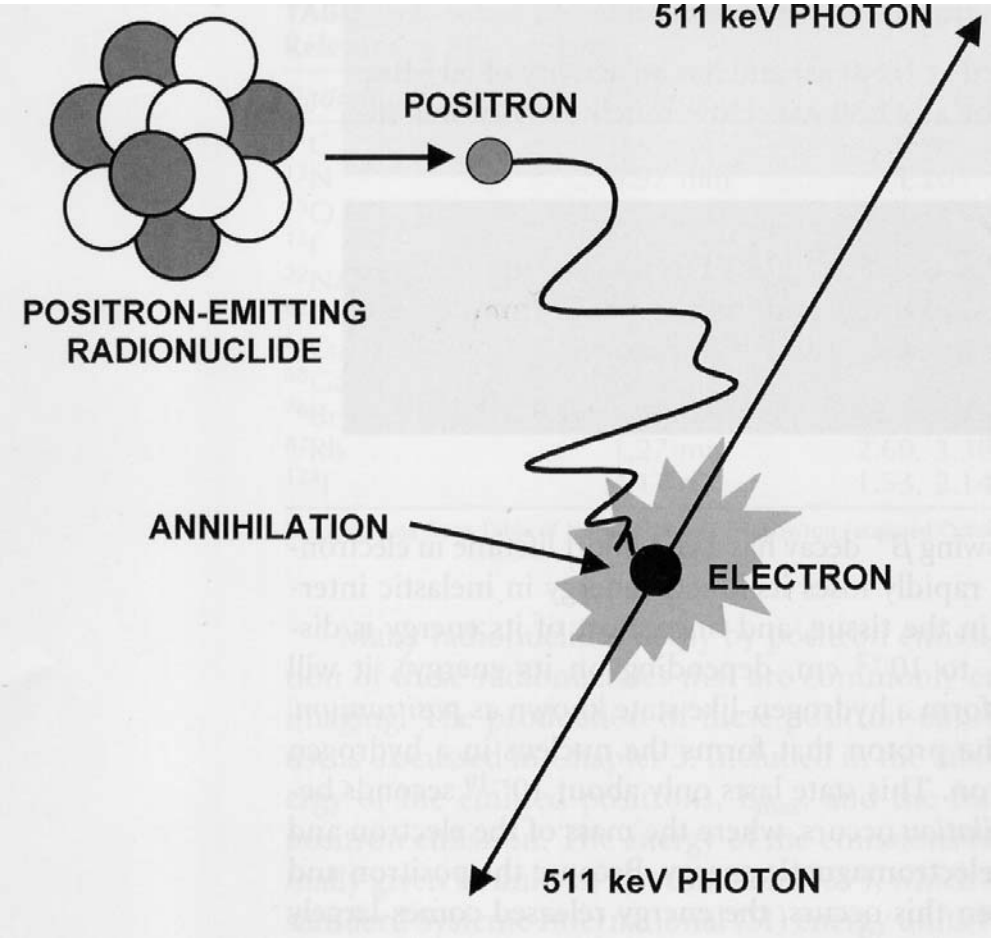

Figure 1-3: The process of positron emission and subsequent positron-electron annihilation results in two 511 KeV annihilation photons emitted 180° apart. The site of annihilation is usually very close to the point of positron emission.

event (called a *true coincidence* if neither photon is *scattered*) is recorded alone the line connecting the two detectors (sometimes referred to as a line of response (LOR)) [2].

A PET scanner is designed to detect and localize the simultaneous back-to-back annihilation photons that are emitted following decay of a radionuclide (Figure 1-4) [9]. With the detection of gamma-ray pairs by detectors outside the human body, tomographic images of the distribution of positron-labeled

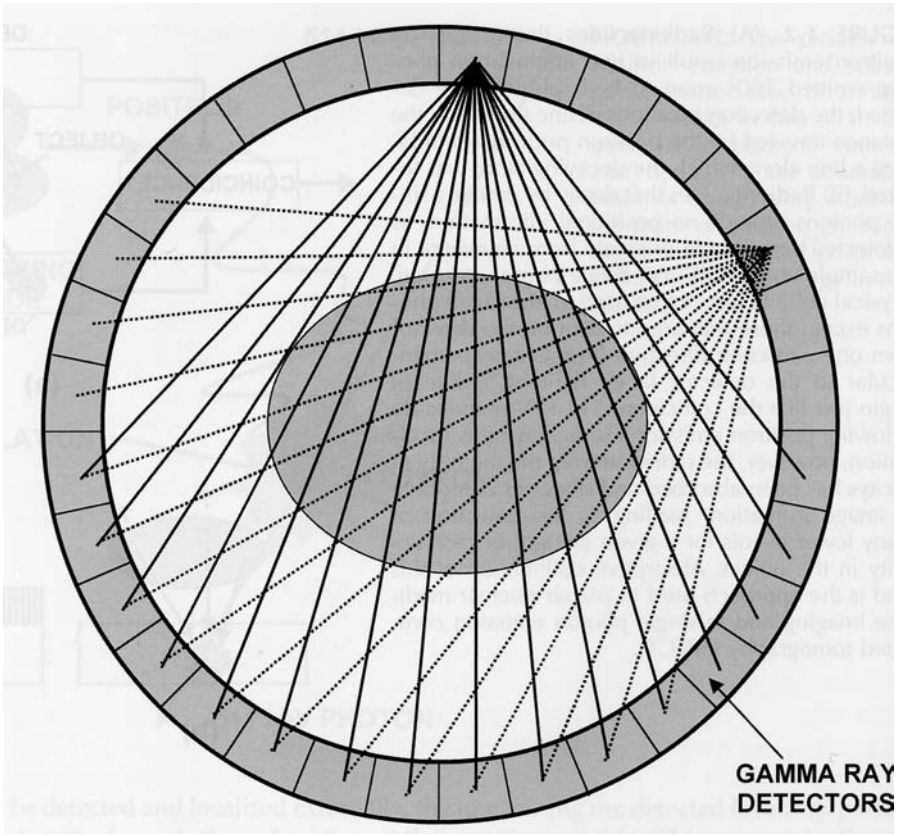

Figure 1-4: Schematic drawing of a PET scanner consisting of a ring of high-energy photon (gamma-ray) detectors. The detectors are designed to record as many of the annihilation photons as possible and to locate the line along which the decay occurred by determining the two interaction vertices. Typically, 10^6 to 10^9 events are needed in a PET scan to reconstruct a statistically meaningful image of the distribution of radioactivity in the body.

compounds can be generated by summing many *true coincidences* to approximate line integrals through the radioisotope distribution. For two-dimensional (2D) imaging, these line integrals form a discrete approximation of the *Radon transform* of a cross-section of the object presented as a gray scale image with the detected count intensity of each pixel [8], which is the theory basis for *image reconstruction*. Figure 1-5 depicts the basic physics of PET.

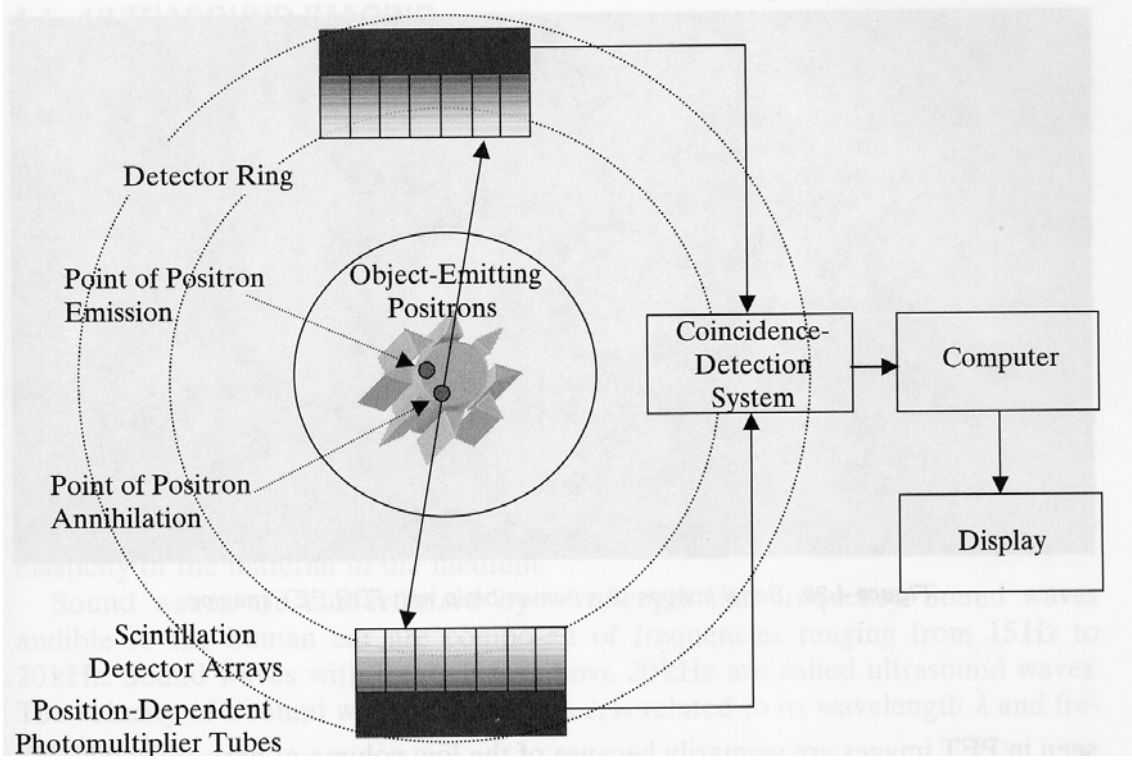

Figure 1-5: Diagram of the basic physics of PET.

1.2.2 Measurement of Radioisotope Concentrations

As aforementioned, the end result of PET acquisition and image reconstruction is an image representing the count density of each pixel. One of the advantages of PET over some other imaging modalities is that it can accurately determine the activity concentration of the radiotracer [9]. To do this, it is necessary to calibrate the efficiency of the system since a PET system will detect only a fraction of the emitted radiation. The usual method of calibration requires the measurement of a source of positron emitter by the PET system, usually as a uniform solution of activity in a cylindrical container much larger in

all dimensions than the spatial resolution of the tomograph. This is followed by the measurement of the amount of activity in an aliquot of the solution with a calibrated radiation detector, such as a well counter. This type of calibration will give the efficiency of the response of the system in terms of activity per unit volume or concentration. Thus, every picture element in the PET image can be scaled by this calibration factor to equal to the activity at that location in the subject and the activity in an organ can be determined by summing over an appropriate *region of interest* (ROI) in the image itself. If they are suitably calibrated, PET images yield quantitative estimates of the concentration of the radiopharmaceutical at specific locations within the body.

1.2.3 Limitations of PET

The major limitations of PET are 1) the cost of providing PET imaging, 2) the technical and logistic complexities, all resulting in a limited availability of PET facilities [5]. Ideally, the value in each pixel of a PET image is equal to the concentration of positron emitter at that point in the subject's body. In practice, as in all measurements, there are sources of error in the technique, and an understanding of these sources of error is required for the proper interpretation of results of PET measurements.

1.3 Principles of Tracer Kinetic Modeling in PET

As stated above, of all the existing imaging modalities, PET is the best instrumentation for absolute quantification of the functional/molecular status of the pathological and physiological systems by using tracer kinetic modeling techniques. If a dynamic sequence of images has been acquired, the kinetics of the radiopharmaceutical can be modeled as a linear dynamic system with the arterial concentration of radioisotope in the blood as the input and the PET measurement as the output. The state variables are the concentrations in different *compartments* of the tissue. The exchange rates between the compartments are parameters of the models. Acquiring a series of images sequentially after injection yields a time-course of the sum of the quantity of tracer in each compartment, *i.e.*, of the output of the model, which can be used to estimate the model's parameters. These parameters can then be used to calculate physiological parameters of interest, such as blood flow, glucose metabolism, receptor binding characteristics, *etc*. thus, PET can be used for precise quantitative measurements of specific physiological quantities [2].

1.3.1 Tracer Kinetic Techniques

Tracer kinetic techniques have its roots in pharmacokinetics, and are generally used in physiology and biochemistry as well to trace dynamic processes, such as blood flow, substrate transport, and biochemical reactions [8]. In tracer kinetic techniques, an appropriate tracer is required to follow the

dynamic process of interest. Usually, a tracer must either be structurally related to the natural substance involved in the dynamic process or have similar transport properties. Furthermore, the tracer must be measurable and distinguishable from the natural substance that it intends to trace. The tracer introduced is assumed to be in a trace amount, so that the process being measured is not perturbed by the introduction of the tracer. The dynamic process being evaluated with a tracer kinetic technique is usually assumed to be in a steady stage. It has been demonstrated that the diagnostic modeled parametric images can be far superior to simple static maps of tracer uptake. In the context of clinical applications, the generation of parametric images should be emphasized over ROI-based modeling. To interpret the data, tracer kinetic models are developed for each radiopharmaceutical to convert the radioactivity images into measurements of physiologically relevant variables such as blood flow, metabolism, and receptor number *etc.*. The time-activity function can be substituted with any tracer kinetic model that is linear in the unknown parameters.

For tracer kinetics, there exist various kinds of mathematical models of different mathematical characteristics --- deterministic versus stochastic, distributed versus nondistributed, compartmental [10] versus noncompartmental [11], and linear versus nonlinear [8]. For most PET analysis, linear compartmental models are most preferred, because of their attractive mathematical properties to provide adequate parameter estimates.

1.3.2 Compartment Model

The basis of a compartment in a system is one of lumping material with similar characteristics into discrete collections that are homogeneous and behave identically [12]. Compartment models attempt to describe the kinetics of an underlying process through the use of interconnected pools of a tracer in a particular form or space [9], [12]. The interconnections represent a flux of material, which physiologically, represent transport or a chemical transformation, or both. Linear interconnections are often constant values which can vary from tissue region to region but are not dependent on tracer mass or time. Although most physiological and biomedical processes are nonlinear, as far as tracers are concerned they often behave linearly (or approximately linearly) with regards to transport or chemical reactions due to the fact that the mass of tracer is typically much less than its natural counterpart [13]. The fundamental property that governs a complete tracer kinetic model is mass balance, which means that the rate of change of mass for a given compartment must equal the net mass coming in per unit time into a pool minus the net mass leaving per unit time. The related mathematical equations describing the compartment models are often referred to as *state equations*. The most general two-pool model structure was shown in Figure 1-6. This model has 6 nonnegative parameters: k_{21}, k_{12}, k_{01}, k_{02}, V_1, V_2; a maximum of two independent input variables $u_1(t)$ and $u_2(t)$; and a maximum of two possible independent measurement (output) variables $y_1(t)$ and $y_2(t)$ in pools 1 and 2, denoted by broken lines. The k's are (fractional) rate constants, with dimensions of time^{-1}; the V's are volumes; the u's are mass flux rates (mass/time); and the y's may be concentrations (mass/vol) or amounts (mass/vol).

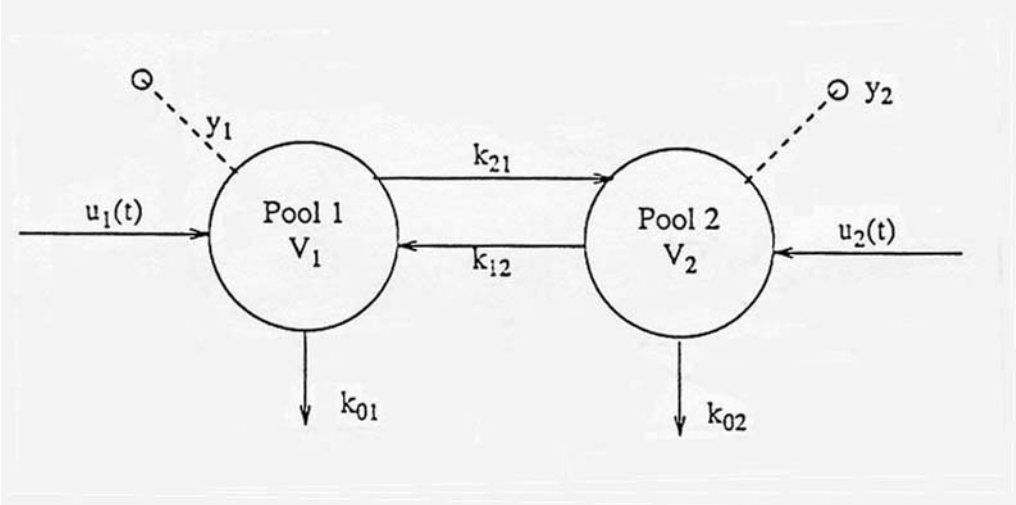

Figure 1-6: The most general two-pool model structure.

The two major factors that determine the tracer kinetics in tissue are the input function and the model configuration. In general, tracer kinetic models cannot be developed from tracer kinetic measurements alone. A *priori* knowledge must be utilized to determine the model structure. Kinetic measurements then can evaluate the validation of the model structure. When an accurate compartment model has been validated, accurate estimates of the biochemical and/or physiological parameters can be provided.

1.3.3 Measurement of the Input Function

As stated above, tracer kinetic modeling with PET requires measurements of the time-activity curves (TACs) in both blood and tissue to estimate the parameters. The blood TAC is usually referred as the model input function. The

usual method of obtaining the input function is to catheterize an artery of the subject and to take a series of blood samples following the injection of the positron emitter. The blood samples must be obtained with a frequency and over a length of time adequate to define the level of activity and shape of the input function. The frequency of sampling depends on the rate of injection and the rate of clearance of the activity from the blood. The length of time of sampling depends on the kinetics of the process being measured. The requirements of the sampling must be determined on an individual basis for each procedure.

The cannulation procedure is in general very invasive and time-consuming. Two methods have been developed to avoid arterial puncture in the measurement of the input function. The first takes advantage of the fact that, when the temperature of the hand is raised, there is dilation of the blood vessels and the blood in the surface veins is effectively arterialized [14]. This produces a very high blood flow in the hand without an increase in metabolic function, and the extraction of substrate in the hand is typically small. This method will probably be valid in those cases in which the rate of injection and rate of change of activity in the blood are relatively slow and the normal temperature extraction of the tracer into the tissue of the hand is relatively low. The second method uses the PET system to measure the amount of activity in the left ventricle, aorta, or other large artery as a function of time [15]-[19]. These image-based approaches have the advantages of being noninvasive but always require that the system be capable of accumulating images rapidly enough to satisfy the temporal sampling requirements of the particular input function.

1.3.4 Model Validation

Validation of a model is an important step before using it to extract information from the measured data. Kinetic validation aims to determine if the model prediction of TACs is consistent with the observed data. If the difference between the predication and the observation are randomly distributed about zero, which would indicate that the model is a good representation of the data. Large standard errors of the parameter estimates usually imply that the model has too many parameter unless the data are extremely noisy [9]. Regardless of the exact methods used to perform model validation, it is never the case that a model is proven to be true by the validation process. The validation process simply helps support to use the model to estimate the process.

1.4 Parameter Estimation in PET

To perform quantitative study and generate the physiological parametric image, parameter estimation is required. The goal of parameter estimation is to mathematically extract useful “information” from measured data. In PET, parameter estimation techniques are employed both in the validation of new tracer kinetic model and in its subsequent application to patient protocols. The most robust method for the estimation of model parameters is weighted nonlinear regression [20]. Weighted nonlinear regression is an iterative process in which starting estimates of all parameters along with equations that govern a particular

model are used to generate a refined estimate of the parameter. This approach is repeated until some criteria are met for achieving convergence [9]. Typically, we aim to minimize the square of the difference between the observation and model prediction for all observations referred to as the weighted residual sum of squares (WRSS). For analyzing the estimation results, some common procedures, including the tests for significance of parameter estimates, model differentiation and validation and goodness of fit, *etc.*, could be adopted. Image-wide parameter estimation for parametric imaging has stimulated the exploration of many fast algorithms due to the time-complexity of the nonlinear regression and its difficulty in convergence when the data are very noisy.

Tracer kinetic modeling and parametric quantification techniques for FDG, the most clinically useful cancer imaging tracer today, have been studies extensively with different degrees of refinement, simplification, and compromise between practicality and accuracy [2]. Figure 1-7 gives an example of key requirements and processes in generating brain parametric or quantitative functional images using PET and glucose tracer FDG.

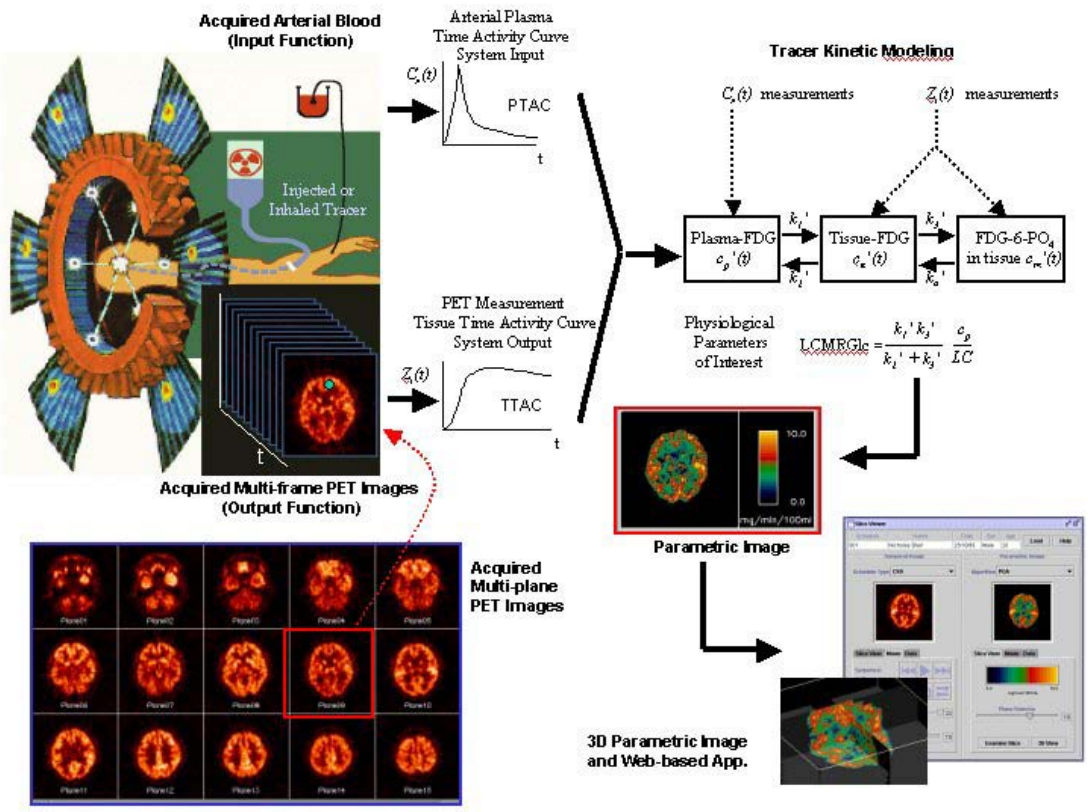

Figure 1-7: Main requirements for quantitative physiological parameter estimation. The activity of the radiotracer is measured quantitatively over time along with the activity in plasma, after the introduction of FDG. The physiological parameters of interest are estimated by applying a mathematical model (compartment model) to the data.

1.5 Organization of the Thesis

This thesis will be organized into eight chapters. Chapter 1 presents the general background of the application of PET in oncology, the clinical difficulty in detecting HCC in a much early stage, the principles of PET imaging, tracer kinetic modeling techniques, and the parameter estimation techniques used for in *vivo* measurement of physiological parameters.

Chapter 2 conducts quantitative dynamic modeling to evaluate the kinetic characteristics of ^{11}C-acetate in HCC and non-tumor liver tissue. The model parameters could provide quantitative evidence and understanding on the kinetic basis of ^{11}C-acetate for its potential role in the imaging of HCC using PET. A three-compartment model consisting of four parameters with fixed weight dual-input function is proposed and compared with that of five parameters. Clinical dynamic datasets extracted from six patients are used to test the presented model candidates. Estimation of the adequacy of these models is based on Akaike Information Criteria (AIC) and Schwarz Criteria (SC) by statistical study. The forward clearance $K=K_1*k_3/(k_2+k_3)$ is estimated and defined as a new parameter called the *local hepatic metabolic rate-constant of acetate* (*LHMRAct*) to find whether it could be used to differentiate HCC from the surrounding liver tissue.

Chapter 3 quantifies the individual contribution ratio of the hepatic artery (HA)/portal vein (PV) to the dual hepatic blood supply in different ROIs to further improve the accuracy of quantitative analysis since in real pathology, both tumor and non-tumor liver tissue can be heterogeneous in the distribution and proportion of the two blood supplies. A new model structure is presented by including an extra parameter a_v in the model input function to describe the contribution of PV to the liver. The new model structure is also intended to find more diagnostic information for the early detection of hepatic metastases.

Chapter 4 develops a novel fast algorithm: dual-input-generalized linear least squares (D-I-GLLS) to identify the ^{11}C-acetate dual-input model parameters including the parameter in the dual-input function. Although a variety of fast

parametric imaging techniques have been developed, most of them focus on single input systems, which do not provide optimal solution for dual-input biomedical system parameter estimation, which is the case of liver metabolism.

Chapter 5 presents two novel statistically reliable and computationally efficient parameter estimation techniques: graphed NLS (GNLS) and graphed dual-input generalized linear least squares (GDGLLS) algorithms for ^{11}C-acetate dual-input liver model. The computational time-complexity of NLS method is high and some estimates are not quite reliable or even fail to convergence, which limits its application in clinical environment and is not practical for the generation of parametric images. In addition, liver system modeling with dual-input function is very different from the widespread single-input biomedical system modeling. Therefore, most of the currently developed estimation techniques are not applicable for the liver ^{11}C-acetate-PET images.

Chapter 6 investigates the effectiveness of modeling the dual hepatic blood supply with dynamic ^{11}C-acetate PET to noninvasively and efficiently access the portal venous blood flow. Measurement of the PV curve is a tedious or even impractical task, therefore, the new model structure will be very valuable for providing the functional parametric images to evaluate HCC in a much early stage.

Chapter 7 applies the cluster analysis to segment the dynamic ^{11}C-acetate PET images in liver automatically. Manual placement of ROIs is subject to operator's skill and time-consuming. Furthermore, the small size of some ROIs

makes the task even more difficult. Two approaches based on cluster analysis will be adopted to segment the dynamic images.

Chapter 8 concludes the work described in this thesis. A brief discussion of future work that relates to the present work will also be provided.

Chapter 2 Tracer Kinetic Modeling of ^{11}C-Acetate Applied in the Liver with Positron Emission Tomography

2.1 Introduction

The hallmark of positron emission tomography (PET) is its ability to quantify *in vivo* the physiological and biochemical processes in humans using intravascularly injected PET tracers. Kinetic modeling using ^{18}F-fluorodeoxyglucose (FDG) is well established for measurements of many physiological parameters, but little attention has been given to the quantitative evaluation of liver metabolism, in spite of its central role as the “power house” of the human body. The use of PET for the studying of liver disease has been mostly in the detection of liver tumors [4]. Hepatocellular carcinoma (HCC) is the most common malignancy worldwide in men. Its occurrence is much higher in the Asian and African locality due to the prevalence of hepatitis B and C, in addition to other associated factors including cirrhosis and mycotoxins. Chronic infection with the hepatitis B virus and hepatitis C virus also increases the risk of developing HCC. It is one of the top three causes of cancer death in many Asian localities including China, Taiwan, Singapore and Japan. The disease is also believed to be in an upward trend in America due to the increasing frequency of

hepatitis C viral infection [21] and it is also a common cause of cancer deaths among Asian immigrants. Since the majority of patients present with advanced-stage malignancy are common associated with chronic liver disease and underlying cirrhosis, treatment options remain limited [7]. Poor hepatic functional reserve due to underlying cirrhosis is the major factor which limits extended surgical resection in many cases [22]. In these circumstances, less than 10% could be cured with surgical resection. Overall 5-year survival rate is less than 5% [23], [24]. Therefore, early and accurate diagnosis of HCC will increase the chance of cure and survival in these patients, lower the rate of recurrence and, hopefully, may prolong survival.

The rate of glucose metabolism (glycolysis) is increased in many forms of malignant tumors. It is directly correlated with tumor proliferation. The investigation of tumor kinetics by FDG-PET imaging has recently suggested that HCC has a non-zero dephosphorylation kinetic constant k_4 [25]. A non-zero k_4 is due to the presence of the enzyme glucose-6-phosphatase in HCC, the abundance of which leads to leakage of the trapped FDG metabolite back to the circulation. This may account for one of the reasons that 40-50% of HCC are not FDG-avid. This is regarded as the Achilles' heel of FDG-PET in the evaluation of liver tumors and is clearly not acceptable in countries where this tumor is one of the top three causes of cancer deaths.

Recently we have investigated the usefulness of ^{11}C-acetate in imaging HCC and other liver masses. Preliminary research findings have suggested that this agent might have a great potential role as a complementary tracer to and perhaps

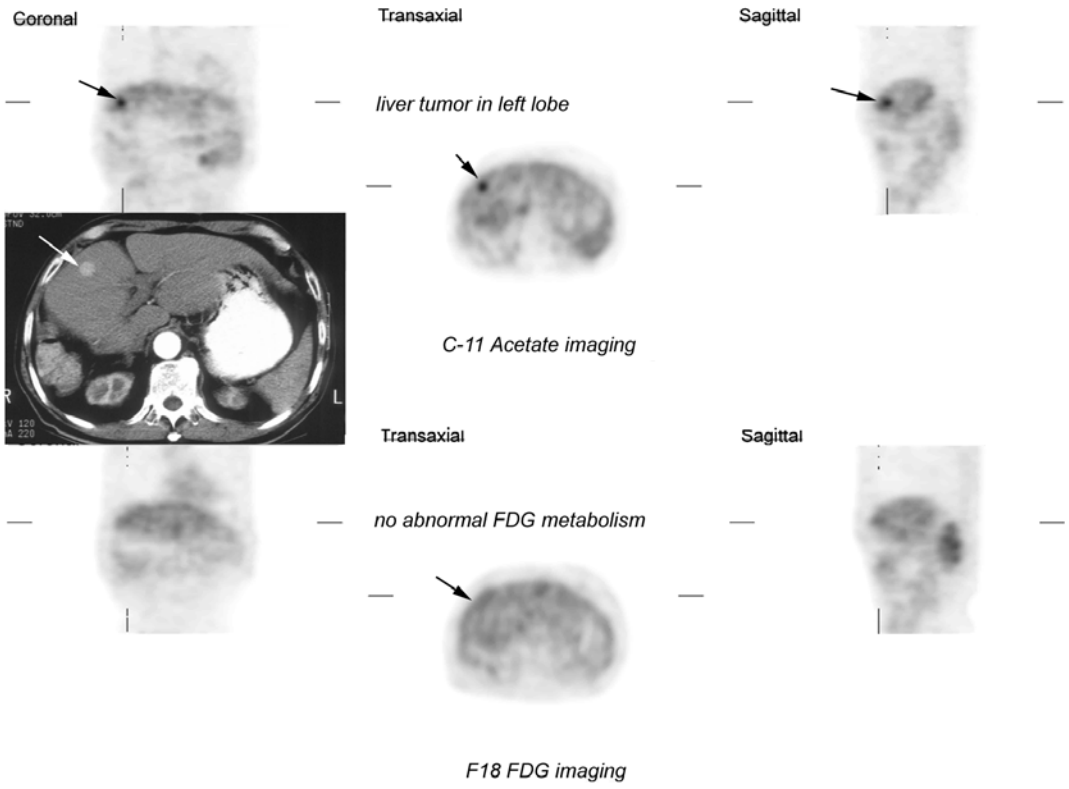

Figure 2- 1: CT demonstrates a hypervascular lesion in the L lobe of liver (status post R lobectomy for HCC); FDG imaging shows no abnormal FDG uptake; ^{11}C-acetate imaging shows increased metabolism.

a better tracer than FDG [6] [7]. Figure 2-1 demonstrates a case of recurrent HCC in the left lobe of liver after right lobectomy. CT shows hypervascularity within the tumor. FDG-PET imaging shows no abnormal FDG uptake by the tumor, whereas ^{11}C-acetate PET imaging shows increased metabolism.

^{11}C-acetate has been extensively validated as a PET tracer for the noninvasive assessment of regional myocardial oxygen consumption and myocardial blood flow [26]-[36]. It is also a useful tracer for urologic tumors

[37]. However, little data exist in the literature regarding the investigation of ^{11}C-acetate on HCC before Ho *et al.* [6]. The exact metabolic pathway of ^{11}C-acetate within tumors such as HCC is not well understood, although participation through acetyl-CoA in Beta oxidation for free fatty acid synthesis is thought to be the preferred biochemical method of incorporation. Application of kinetic modeling techniques may in addition provide improved understanding of these complex biokinetic processes [38]. In this chapter, a three-compartment four-parameter (4-P) kinetic model with dual inputs for evaluation of ^{11}C-acetate metabolism in liver was proposed. Comparison of this 4-P model and a three-compartment five-parameter (5-P) model with dual inputs was conducted. A new physiological parameter called the "*local hepatic metabolic rate-constant of acetate* (*LHMRAct*)" was introduced to characterize the regional consumption of acetate by both tumor and non-tumor tissue of the liver.

2.2 Methods

2.2.1 PET Scanning

An ECAT-EXACT 47 PET scanner (CTI/Siemens, Inc., TN, USA) was used for transaxial (septa-extended) dynamic image acquisition. Full sets of dynamic data in one single position, covering the liver dome and apical half of the left ventricle to the inferior part of liver, were obtained for 10 min immediately following bolus IV injection of ^{11}C-acetate. Sampling acquisition sequence was as follows: 4 sec frames x 10, 10 sec frames x 8, 30 sec frames x 2; 60 sec frames

x 3 and 120 sec frames x 2, a total of 25 frames. Standard static PET imaging covering the entire liver was also performed from 10-20 minutes. Then FDG was injected and FDG-PET imaging was performed 1 hour later (allowing more than 4 half-life decay for ^{11}C-acetate).

2.2.2 Human Studies

Six patients, all are hepatitis B carriers, including two with HCC, were recruited into the study. Ten regions of dynamic datasets, two from HCC regions, were extracted.

2.2.3 Blood Time-Activity Dual-Input Functions

The tracer time-activity curve (TAC) in blood (BTAC) $c_b(t)$ was used as the input function in the kinetic model. BTAC is usually represented by a sequence of arterial or arterialized blood samples. However, blood sampling is in general very invasive and requires extra personnel and processing time. Several noninvasive techniques have been proposed by some researchers. One was proposed to extract the input function together with the physiological parameters from the dynamic images [39], [40]. Chen *et al.* [41] had reported using TAC obtained from the region of interest (ROI) drawn on the target organ during dynamic PET imaging as an input function. The utilization of image-derived input function has been more commonly used in quantitative PET studies of the heart [42]. The reliability of using BTAC obtained directly by drawing a ROI

over the left ventricle (LV) or the left arterial region were investigated in [43]. Double modeling approach for dynamic cardiac studies with PET to estimate physiological parameter was also proposed [44].

The liver has a dual source of blood supply, receiving oxygenated blood from the common left and right hepatic arteries (HAs) and nutrient-rich blood via the portal vein (PV) [45]. Therefore, the use of arterial input may, however, introduce systematic errors in the estimated kinetic parameters because of the ignorance of the hepatic dual blood supply from the HA and the PV to the liver [4]. It is highly invasive and virtually impossible in clinical settings to count the radioactivity of the portal venous blood by direct catheterization and sampling. For the modeling method, the existence of dual blood supply in the liver would necessitate twice the number of parameters required for full characterization. For preliminary investigation, this method of modeling appears impractical. Therefore image-derived BTAC appears to be the only option at the moment.

In this work, the BTAC was obtained directly from PET images measurements. To reduce the scattering effect of radioactivity from the adjacent tissue, the contribution from the HA was approximated by evaluating the TAC of the abdominal aorta adjacent to the liver instead of the LV. The contribution from the PV was evaluated by direct activity-time measurement. The tracer arriving at the PV is delayed and dispersed when compared with that of the HA, making its activity similar to that of the tracer in the non-tumor liver tissue. Therefore, it is difficult to differentiate the PV from the surrounding hepatic parenchyma. However, its location may still be identified by its invariable

anatomical position being posterior to the pancreatic head that shows the most intense physiological uptake of ^{11}C-acetate, or by direct reference to the CT images. The radioactivity spillover from the surrounding tissue to the PV is significant, especially at the later part of the study when the tracer concentration in tissue is much higher than that in the PV. Munk, *et al*. [4] suggested that the difference between the two blood TACs was most pronounced around the peak and immediately after the bolus injection. After some time they are virtually identical. Therefore, the last five measurements of the TACs of the PV from PET images were replaced by the HA data in this study. To strike a reasonable statistical balance without compromising physiological requirement, in this chapter, the BTAC was measured empirically by using fixed weights from these two blood supply inputs, *viz*. 20% contribution from HA and 80% from PV according to their approximate percentage perfusion to the non-tumor liver tissue. Thus the dual-input function was calculated according to

$$c_b(t) = c_a(t) \times 20\% + c_v(t) \times 80\% \quad (1)$$

where $c_a(t)$ is the tracer concentration in the HA and $c_v(t)$ is the tracer concentration in the PV. However, the majority of the blood supply to the tumor is from the HA rather than the PV, accordingly, the weights of tumor used was 80% or 60% contribution from HA. The weight determination for different ROIs would be further studied in Chapter 3. Figure 2-2 shows an example of typical blood TACs from the HA, the PV and the weighted dual-input function for the non-tumor liver tissue.

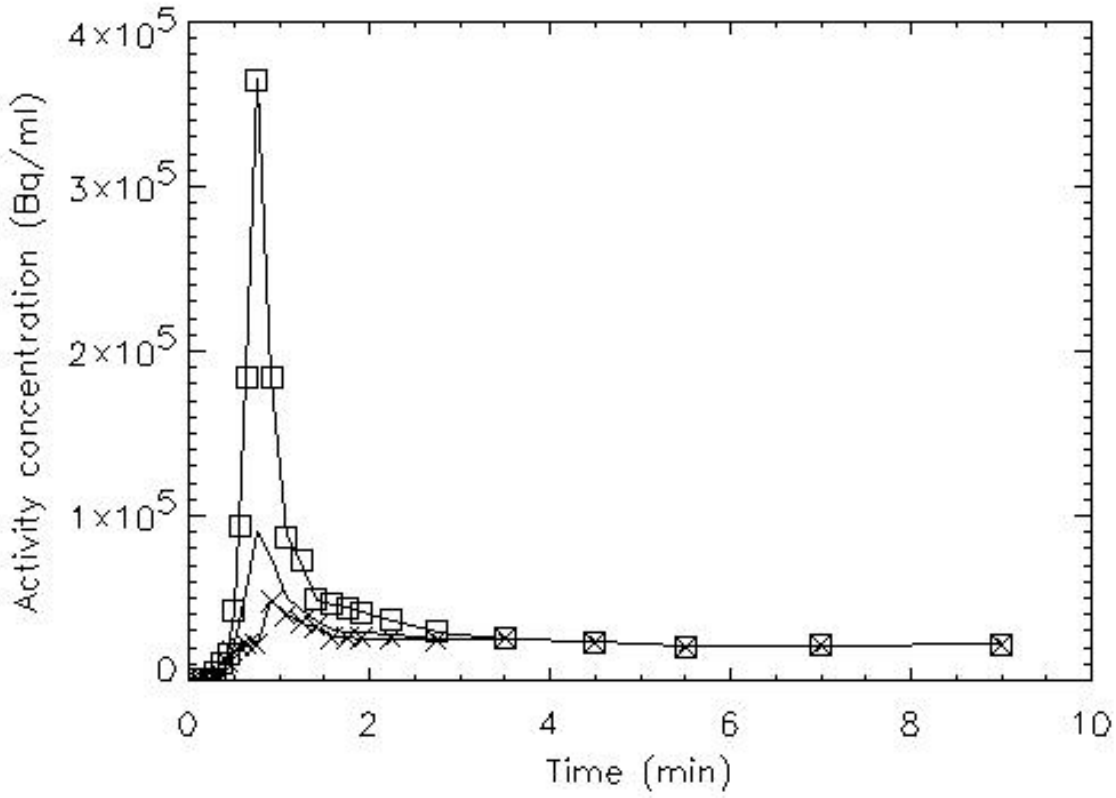

Figure 2- 2: Typical TACs of the HA, PV and weighted dual-input function of the non-tumor tissue. Solid line stands for the weighted dual-input, solid line marked by "□" is for the HA and "×" for the PV. The greatest activity difference among these 3 curves is during the initial radionuclide angiographic phase.

In this preliminary study, the metabolites of ^{11}C-acetate in blood were not taken into consideration in order not to complicate the issue of defining the suitable model. Also no correction was made for the noise scatters of the inputs.

2.2.4 Liver Kinetic Model for ^{11}C-Acetate

It is not just a clinical observation that HCC may display variable tumor kinetics. Early research on rat hepatomas had suggested that the patterns of

glycolytic enzymes might reflect hepatoma cell growth, function, and graded dedifferentiation [46]. Preliminary study shows that in some cases, FDG and ^{11}C-acetate are taken up by different parts of the tumor, suggesting that mixed pathology with dual tracer kinetics could exist within these tumors. Past researches on PET tracer kinetic modeling have been reported [47]-[49], but there is no data on kinetic modeling of ^{11}C-acetate PET images in liver. Acetate is enzymatically converted into acetyl-CoA in the liver [50], and then enters the Kreb's Cycle. In the liver, the role of Kreb's Cycle is more complex than in heart muscles [50]. Although the exact biochemical mechanism of ^{11}C-acetate accumulation within HCC is not completely defined, there is evidence that acetate is channeled to acetyl-CoA for fatty acid (lipid) synthesis in tumor cells, instead of being metabolized to CO_2 through the Kreb's cycle [51]. It is therefore reasonable to assume that only one compartment is needed for all of the metabolites in the liver/tumor tissue. A three-compartment model, as shown in Figure 2-3, was proposed in this study. The left compartment of this model represents the intravascular ^{11}C-acetate concentration. The center compartment represents the intracellular ^{11}C-acetate concentration. The right compartment represents the intracellular products/metabolites converted from ^{11}C-acetate (acetyl-CoA, and metabolites of fatty acid synthesis). K_1 represents the first order rate constant for the transport of ^{11}C-acetate from blood to tissue, k_2 for reverse transport of ^{11}C-acetate from tissue to blood, k_3 for conversion of ^{11}C-acetate to its products/metabolites, and k_4 for back conversion from the products/metabolites to ^{11}C-acetate. It should be noted that although the real biological system is complex, this compartmental approach, nonetheless, represents a rather reasonable estimation for global physiological function [38].

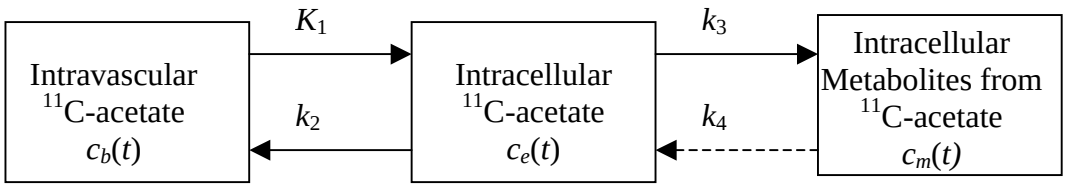

Figure 2- 3: Three-compartment liver kinetic model for ^{11}C-acetate.

Since the number of compartments of this proposed ^{11}C-acetate liver model is the same as that of the FDG model originally proposed by Sokoloff *et al*. [47] and further extended by Huang *et al*. [49] and Phelps *et al*. [48], the differential equations to the ^{11}C-acetate liver model share the same form as the FDG model

$$\frac{d}{dt}c_e(t) = K_1 c_b(t) - (k_2 + k_3)c_e(t) + k_4 c_m(t) \tag{2}$$

$$\frac{d}{dt}c_m(t) = k_3 c_e(t) - k_4 c_m(t) \tag{3}$$

$$c_i(t) = c_e(t) + c_m(t) \tag{4}$$

where $c_b(t)$ is the ^{11}C-acetate concentration in the whole blood calculated by equation (1), $c_e(t)$ is the free ^{11}C-acetate concentration in intracellular space, $c_m(t)$ is the intracellular products/metabolites concentration, $c_i(t)$ is the sum of $c_e(t)$ and $c_m(t)$. The solution of $c_i(t)$ in terms of macroparameters is

$$c_i(t) = (B_1 e^{-L_1 t} + B_2 e^{-L_2 t}) \otimes c_b(t) \tag{5}$$

where

$$B_1 = \frac{K_1}{\alpha_2 - \alpha_1}(k_3 + k_4 - \alpha_1), \qquad L_1 = \alpha_1$$

$$B_2 = \frac{K_1}{\alpha_2 - \alpha_1}(\alpha_2 - k_3 - k_4), \qquad L_2 = \alpha_2$$

$$\alpha_{1,2} = \frac{k_2 + k_3 + k_4 \mp \sqrt{(k_2 + k_3 + k_4)^2 - 4k_2k_4}}{2}.$$

B_1, B_2, L_1, L_2 are the macroparameters in the model and $\otimes$ denotes the operation of temporal convolution. If k_4 approaches zero, for simplicity, letting k_4 be zero, thus the macroparameters of the model were given by

$$B_1 = \frac{K_1 k_3}{k_2 + k_3}, \qquad L_1 = 0 \tag{6}$$

$$B_2 = \frac{K_1 k_2}{k_2 + k_3}, \qquad L_2 = k_2 + k_3.$$

The total activity of tracer in tissue includes both the activity of hepatic parenchyma and the activity within vascular/sinus space of liver tissue. As the blood volume in the liver is fairly large, a hepatic blood volume (*HBV*) term was included in our proposed ^{11}C-acetate model to account for this effect. The observed total tissue activity $c_T(t)$, is

$$c_T(t) = c_i(t) + HBV \times c_b(t). \tag{7}$$

With the measurements of both BTAC $c_b(t)$ and TTAC $c_T(t)$, the parameters of the 4-P (without k_4) and 5-P (with k_4) models were estimated by the weighted non-linear least square (NLS) method.

2.2.5 Statistical Study

The weighted NLS algorithm was used to numerically evaluate all the individual parameters. Statistical analysis, such as standard deviation (*SD*),

coefficient of variation (*CV*) *etc.*, was performed. The *CV* of a parameter estimate was calculated from

$$CV_P = \frac{SD_P}{P} \times 100\% \tag{8}$$

where P is the parameter estimate and SD_P is the standard deviation of P. Model parameters were estimated by minimizing the weighted residual sum of squares (*WRSS*) [4]. In this chapter, the weights used were proportional to the frame duration divided by the concentration value of that time point. The three-compartment 4-P and 5-P models were used to fit the clinical data. The best model fitted to the data is not necessarily the model producing the smallest *WRSS*, because adding more parameters generally decreases the *WRSS* [4]. The Akaike Information Criteria (AIC) [52] and Schwarz Criteria (SC) [53] were used to test which one is better. The AIC and the SC were given by (We assume that the data variances are known up to a constant)

$$AIC = N \ln(WRSS) + 2N_P \tag{9}$$

$$SC = N \ln(WRSS) + N_P \ln N \tag{10}$$

where N_P is the number of parameters in the model, and N is the number of data points. The best model by the AIC or SC is the one that minimizes the AIC or SC respectively. The AIC or SC provides a balance between data fitting precision in the first term and minimum dimensionality in the second [52], [53].

2.2.6 Model Estimation of the *LHMRAct*

The newly proposed physiological parameter *LHMRAct* was calculated using the following formula

$$LHMRAct = \frac{K_1 k_3}{k_2 + k_3} \tag{11}$$

where K_1 to k_3 can be derived from the results of NLS fitting. When k_4 is assumed to be zero, Patlak analysis [54] can also be applied to this study. The ratio of $c_T(t)$ and $c_b(t)$ can be calculated by

$$\frac{c_T(t)}{c_b(t)} = \frac{K}{c_b(t)} \int_0^t c_b(\tau) d\tau + \frac{K_1 k_2}{(k_2 + k_3)^2} + HBV \tag{12}$$

where

$$K = \frac{K_1 k_3}{k_2 + k_3}.$$

The data points within the period 3 min to 10 min were chosen to estimate the *LHMRAct* using Patlak method. The fitting results were compared with those obtained from the NLS methods by correlation analysis.

2.3 Results and Conclusion

Both the weighted NLS algorithm and the linear Patlak analysis were used for parameter estimation. The ^{11}C-acetate clinical data from ten ROIs were analyzed to test the 4-P and 5-P models and several statistical criteria were used to validate their adequacy. Results were given as the estimated value ± *SD*. The parameter estimates by the weighted NLS algorithm for the 4-P and 5-P models were summarized in Tables 2-1 and 2-2. As seen in Tables 2-1 and 2-2, the estimated values of the same parameter for the two models are approximated to each other, but the *CVs* of the estimated parameters for the 4-P model are far smaller than those for the 5-P model. For the 5-P model, the *CVs* of the estimated

Table 2- 1: Estimation results of the three-compartment 4-P ^{11}C-acetate liver model with dual-input function.

Datasets number	Estimated Parameters				Criteria	
	K_1 (ml/min/ml)	k_2 (min^{-1})	k_3 (min^{-1})	*HBV*	AIC	SC
1	0.652±0.048	0.312±0.059	0.085±0.030	0.038±0.020	181.1	185.9
2	0.731±0.064	0.284±0.065	0.064±0.035	0.047±0.027	197.4	202.3
3	0.759±0.033	0.290±0.031	0.051±0.016	0.036±0.015	164.0	168.9
4	0.456±0.019	0.237±0.029	0.075±0.020	0.383±0.012	144.2	149.1
5	0.461±0.034	0.245±0.052	0.072±0.035	0.367±0.023	173.6	178.5
6	0.709±0.068	0.509±0.090	0.170±0.023	0.362±0.030	165.2	170.0
7*	1.251±0.068	0.364±0.046	0.113±0.019	0.125±0.028	189.1	194.0
8	0.996±0.055	0.254±0.038	0.042±0.024	0.140±0.028	176.5	181.4
9	0.704±0.073	0.344±0.087	0.102±0.039	0.030±0.029	178.4	183.3
10*	0.806±0.071	0.280±0.124	0.472±0.132	0.100±0.022	168.5	173.3

* Regions 7 and 10 represent HCC. The input functions of regions 7 and 10 are 80% and 60% contribution from HA respectively.

Table 2- 2: Estimation results of the three-compartment 5-P ^{11}C-acetate liver model with dual-input function

Datasets number	Estimated Parameters					Criteria	
	K_1 (ml/min/ml)	k_2 (min^{-1})	k_3 (min^{-1})	k_4 (min^{-1})	*HBV*	AIC	SC
1	0.660±0.063	0.327±0.122	0.101±0.184	0.015±0.285	0.037±0.023	184.0	190.1
2	0.747±0.460	0.314±0.182	0.090±0.290	0.019±0.245	0.045±0.031	200.3	206.4
3	0.780±0.199	0.321±0.045	0.078±0.125	0.046±0.265	0.029±0.018	165.7	171.8
4	0.455±0.094	0.238±0.137	0.085±0.102	0.039±0.237	0.383±0.016	146.7	152.8
5	0.463±0.361	0.254±0.250	0.084±0.035	0.023±0.252	0.365±0.029	176.0	182.1
6	0.722±0.093	0.540±0.280	0.196±0.038	0.025±0.069	0.359±0.035	166.0	172.1
7*	1.262±0.246	0.378±0.219	0.130±0.024	0.024±0.103	0.120±0.031	190.6	196.7
8	1.015±1.223	0.257±0.156	0.042±0.088	0.018±0.342	0.130±0.031	178.2	184.3
9	0.743±0.356	0.372±0.212	0.109±.0.276	0.028±0.399	0.021±0.035	178.8	184.9
10*	0.804±1.142	0.283±0.557	0.498±0.209	0.010±0.018	0.096±0.023	170.0	176.1

* Regions 7 and 10 represent HCC. The input functions of regions 7 and 10 are 80% and 60% contribution from HA respectively.

K_1 range from 9.5% to 77.8% except regions 8 and 10, where *CVs* of K_1 are 121% and 142% respectively. The *CVs* of the estimated k_2 range from 13.9% to 98.5% except region 10 (where *CV* of k_2 = 197%). Only four *CVs* of the estimated k_3 among the ten sets of data are less than 100% and the *CVs* of the estimated k_4 are far from acceptable. The *CVs* of the estimated *HBV* are generally

acceptable except region 9. Since the estimated k_4 values for the 5-P model are very small and are less reliable for interpretation, it is reasonable to assume k_4 to be zero during the first 10 min dynamic scan. For the 4-P model, the maximum *CV* of the estimated K_1 is 10.4% (for region 9). The *CVs* of the estimated k_2 range from 10.7% to 25.2% except region 10 (where *CV* of k_2 = 44.2%). The *CV*s of the estimated k_3 range from 13.5% to 56.8%. All of the *CVs* of the estimated *HBV* are smaller than those of the 5-P model. Since the vascularity of cirrhotic liver is heterogeneous, the estimated *HBV* values exhibit moderate variability. As indicated by Tables 2-1 and 2-2, the parameter estimates of the 4-P model are significantly reliable than those of the 5-P model.

The model fitted curves according to the 4-P and 5-P models chosen from the ten clinical datasets were shown in Figure 2-4. Although among the ten datasets six *WRSS* values of the 5-P model are slightly smaller than those of the 4-P model, the *CVs*, AICs and SCs of the 4-P model are all generally less than those of the 5-P model, suggesting that the 4-P model is the better model to characterize the kinetics of ^{11}C-acetate in the liver. Moreover, the fitting results of the 4-P model are less affected by the initial values whereas those of 5-P model are greatly affected. From compartment analysis using the NLS algorithm for the 4-P model, the following physiological parameters were obtained: for the eight non-tumor liver tissue ROIs, the estimated K_1 is 0.684±0.173 ml/min/ml, k_2 is 0.309±0.088 /min and k_3 is 0.083±0.040 /min.

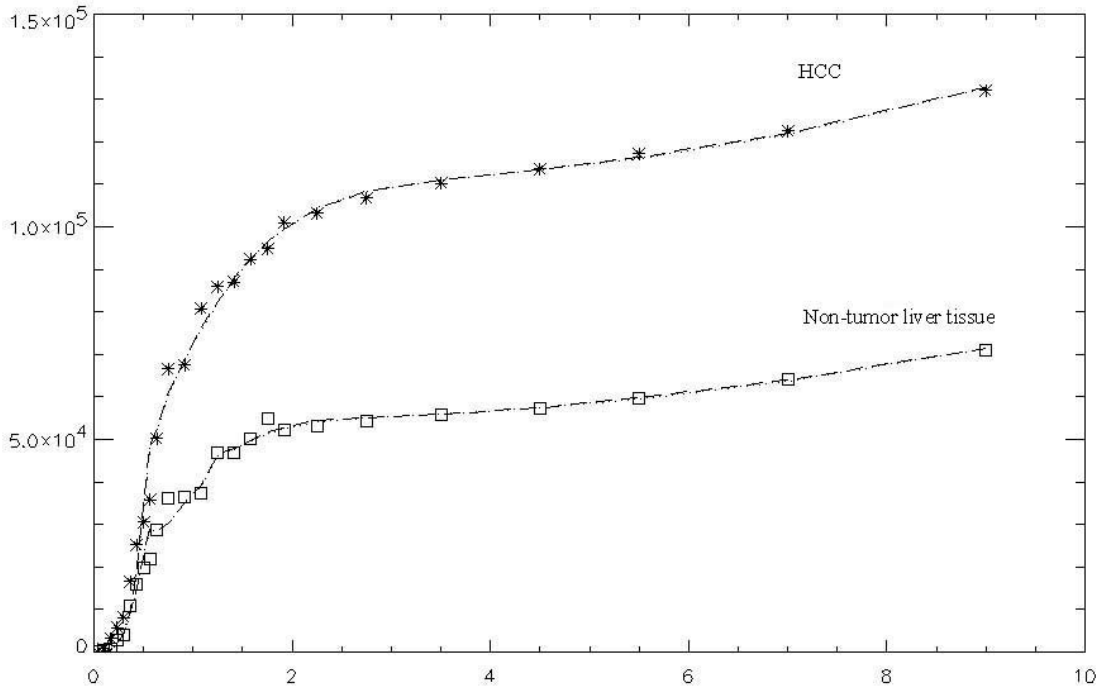

Figure 2- 4: Graph shows the generated TACs of the HCC ROI and the non-tumor liver tissue ROI with symbols * and □ respectively. While, dashed lines are the results of the fitted TACs using the 5-P model; dotted lines are the results of the fitted TACs using the 4-P model.

Table 2-3 provides the results of the estimated *LHMRAct* by the NLS and linear Patlak methods. The correlation coefficients between the results of Patlak method and those of the 4-P and 5-P models using the NLS method are 97.67% and 97.70% respectively. For the eight non-tumor liver regions, the estimated *LHMRAct* values for the 4-P and 5-P models by NLS method are 0.1351±0.0256 ml/min/ml and 0.1515±0.0255 ml/min/ml respectively, and the estimate by Patlak method is 0.1612±0.0200 ml/min/ml. As revealed in Table 2-3, the *LHMRAct* values of the non-FDG-avid type of HCC (regions 7 and 10) are significantly higher than those of the non-tumor liver parenchyma ($p<0.05$), which shows statistically significant difference of this functional parameter of

Table 2- 3: Estimation results of the *LHMRAct* for the 4-P and 5-P models with fixed weight dual-input function using the NLS and Patlak methods.

Datasets number	Estimated *LHMRAct* (K_1*k_3/(k_2+k_3))		
	NLS method for 5-P model	NLS method for 4-P model	Patlak method
1	0.1559	0.1398	0.1642
2	0.1663	0.1345	0.1826
3	0.1518	0.1130	0.1548
4	0.1201	0.1095	0.1562
5	0.1155	0.1046	0.1495
6	0.1921	0.1775	0.1664
7*	0.3227	0.2969	0.2694
8	0.1420	0.1405	0.1259
9	0.1683	0.1609	0.1903
10*	0.5126	0.5057	0.4945

* Regions 7 and 10 represent HCC. The input functions of regions 7 and 10 are 80% and 60% contribution from HA respectively.

^{11}C-acetate in this tumor. Therefore, parametric imaging with ^{11}C-acetate metabolism measured quantitatively (*LHMRAct*) may add supportive evidence of the usefulness of this tracer to HCC detection.

In summary, this three-compartment four-parameter model with dual-input function has been found suitable in mapping the kinetic characters of ^{11}C-acetate in a 10 min dynamic PET imaging of the liver. The model has provided a better understanding of the complexity and biochemistry of the behavior of this tracer in HCC and non-tumor liver tissue. A 10 min dynamic acquisition of ^{11}C-acetate PET imaging may provide enough valuable quantitative data. The parameter *LHMRAct* could be considered as potential indicator of metabolism (other than SUV) for evaluating HCC. ^{11}C-acetate is not just a complementary tracer to FDG, in fact a better tracer than FDG for detection of HCC.

Chapter 3 Noninvasive Quantification of the Differential Portal and Arterial Contribution to the Liver Blood Supply from PET Measurements Using the ^{11}C-Acetate Kinetic Model

3.1 Introduction

As stated in Chapter 2, hepatocellular carcinoma (HCC) is the most frequent malignant tumor of the liver. Patients with HCC are often unaware of its presence until the tumor has reached an advanced stage [22] and less than 10% are cured with surgical resection. Therefore, it is important to detect HCC at its early stage for curative treatment. Positron emission tomography (PET) enables extracting quantitative physiological information *in vivo* from complex dynamic processes by using the tracer kinetic modeling techniques, which makes it useful for early detection of malignant tumors. Our recent research has demonstrated that ^{11}C-acetate could be a complementary tracer to FDG in PET imaging of HCC [6], [55]. To get a better understanding of the characteristics of ^{11}C-acetate in the imaging of HCC in liver, quantitative dynamic modeling has been conducted in Chapter 2.

In Chapter 2, a three-compartment four-parameter (4-P) model was presented and a new physiological parameter called the "*local hepatic metabolic rate-constant of acetate* (*LHMRAct*)" (the forward clearance *K*) was introduced to characterize the regional consumption of acetate by HCC and non-tumor liver tissue. The tracer time-activity curve in blood (BTAC) was used as the model input function. To account for the liver's dual source of blood supply from the hepatic artery (HA) and portal vein (PV), we initially assumed a fixed contribution ratio of HA and PV in formulating the input function, *viz.* 20% contribution from HA and 80% from PV according to their approximate percentage perfusion to the non-tumor liver tissue, 60% or 80% contribution from HA for HCC due to the generally accepted fact that the majority of the blood supply to established liver metastases is derived from the HA [22], [56], [57]. However, early stage metastases may not be easily differentiated on dynamic PET images, therefore, it may be difficult to choose the fixed weight for quantitative study. Furthermore, in real pathology, both the tumor and non-tumor liver tissue can be heterogeneous in the distribution and proportion of the two blood supplies. Small liver tumors (<5mm) are mainly fed by PV; while for larger tumors, these lesions receive up to 95% of their blood supply from HA [58]. For non-tumor liver tissue, the two blood supplies may also vary within the liver and among individual patients due to many factors. Various liver diseases alter hepatic arterial circulation [59]. HCC is associated with liver cirrhosis in 80% of cases [56], it is stated that normal liver parenchyma obtains about 75% of its blood supply from the PVs and 25% from the HAs whereas in cirrhotic livers the blood supply is obtained from the arteries in a proportion up to 75% [57]. The presence of regenerating and dysplastic nodules will also change the liver blood

supply. Therefore, the fixed weighted dual-input function would increase the statistical uncertainties and reduce the accuracy in the estimated model parameters. The individual proportion of the two blood supplies in different regions of interest (ROIs) is needed to achieve more accurate quantitative analysis. In addition, measurement of the relative PV or HA contribution to liver blood flow might provide an alternative method for the detection of liver tumors [57].

Various kinds of methods have been used to distinguish PV and HA's distribution. Direct measurements usually involve cannulation procedures, which are very invasive and always performed on anaesthetized animals [60]. Breedis and Young [61] injected dyes and plastic into the blood vessels for postmortem studies. And later Lin *et al*. [62] used colored silicone rubber injected into the PV and HA to determine the different distribution. All these techniques are too invasive to perform on humans. Alternative noninvasive techniques are therefore of great interest.

Sarper *et al*. [63] presented a noninvasive indirect measurement by using dynamic scintigraphy: measuring the first pass of an intravenous bolus injection of a radioactive colloid through the liver and kidney to obtain the hepatic perfusion index (HPI) from the time-activity curve (TAC) of the liver [57], [64]. Technetium-99m is often used to conduct the scintigraphy [65], [66]. However, this technique is well-recognized to be susceptible to numerous errors in the derivation of the index, such as the overlap of the hepatic arterial and portal venous phases, the presence of intrahepatic portosystemic shunting *etc*. [57].

Chen *et al.* [67] reported non-invasive quantification of hepatic arterial blood flow with Nitrogen-13-Ammonia and dynamic PET. All these techniques require extra examination and processing time, and would cause more discomforts to the patients. Additionally, it is impossible to get the real-time PV and HA's distribution during the PET scan.

In this work, we study the feasibility of including an extra parameter in the vascular input function of ^{11}C-acetate liver model to obtain the differential portal and arterial contribution to the liver blood supply and evaluate the performance of this new modeling technique.

3.2 Methods

3.2.1 Data Acquisition

The study population comprised six subjects, all were hepatitis B carriers, including two with HCC. The transaxial (septa extended) dynamic PET images were obtained on an ECAT-EXACT 47 PET scanner (CTI/Siemens, Inc., TN, USA), which simultaneously recorded 47 contiguous planes. Each patient was positioned to allow image acquisition of the liver dome and apical half of the left ventricle to the inferior part of liver. A Hanning filter was used for image reconstruction, resulting in an in-plane spatial resolution of 4.119 mm. The axial resolution was 3.375 mm.

Serial images were obtained immediately following bolus IV injection of ^{11}C-acetate. The dynamic sequence consisted of ten frames of 4 s, eight frames of 10 s, two frames of 30 s, three frames of 60 s and two frames of 120 s, totaling 25 frames for a total scan time of 10 min.

3.2.2 Image Analysis

ROIs were defined using single transverse slice of the full sets of dynamic ^{11}C-acetate images. Ten regions of dynamic datasets, two from HCC regions, others from non-tumor liver regions, were extracted. In general, tracer kinetic modeling with PET requires the measurements of both BTAC and tracer time-activity curve in tissue (TTAC) to quantitatively estimate the model parameters, using BTAC and TTAC as the input and output functions in the kinetic model. Although the arterial blood measurements are considered the most accurate representation of the BTAC and arterialized venous samples have been validated as a replacement of arterial samples [48], it is generally accepted that the insertion of arterial lines and the subsequent collection and processing of arterial blood are not compatible with the practice of clinical PET [68]. Moreover, it is highly invasive and virtually impossible in clinical settings to count the radioactivity of the portal venous blood by direct catheterization and sampling [55]. Therefore, in this work, the TACs of both HA and PV were evaluated using the image-derived method described in Chapter 2. The PVs are small in size and not very distinguishable from the surrounding tissue, the two-step segmentation method based on cluster analysis proposed in Chapter 7 was also used to facilitate the extraction of the PV region [69].

3.2.3 ^{11}C-Acetate Liver Model with a Non-Fixed Weighted Dual-Input Function

The ^{11}C-acetate liver model was shown in Figure 3-1. The differential equations for the model are

$$\frac{d}{dt}c_e(t) = K_1 c_b(t) - (k_2 + k_3)c_e(t) \quad (1)$$

$$\frac{d}{dt}c_m(t) = k_3 c_e(t) \quad (2)$$

$$c_i(t) = c_e(t) + c_m(t) \quad (3)$$

where K_1-k_3 are the rate constants, $c_b(t)$ is the ^{11}C-acetate concentration in the whole blood, $c_e(t)$ is the free ^{11}C-acetate concentration in intracellular space, $c_m(t)$ is the intracellular products/metabolites concentration, and $c_i(t)$ is the sum of $c_e(t)$ and $c_m(t)$. As seen in Figure 3-1, another parameter "hepatic blood volume (*HBV*)" was included in the model to account for the contribution of the tracer within vascular/sinus space of liver tissue to the observed total tissue activity, then the observed total tissue activity $c_T(t)$, was given by

$$c_T(t) = c_i(t) + HBV \times c_b(t) \quad (4)$$

The solution of $c_T(t)$ in terms of macroparameters is

$$c_T(t) = (B_1 + B_2 e^{-L_1 t}) \otimes c_b(t) + HBV \times c_b(t) \quad (5)$$

where

$$B_1 = \frac{K_1 k_3}{k_2 + k_3},$$

$$B_2 = \frac{K_1 k_2}{k_2 + k_3}, \qquad L_1 = k_2 + k_3$$

are the macroparameters in the ^{11}C-acetate liver model and $\otimes$ denotes the operation of temporal convolution.

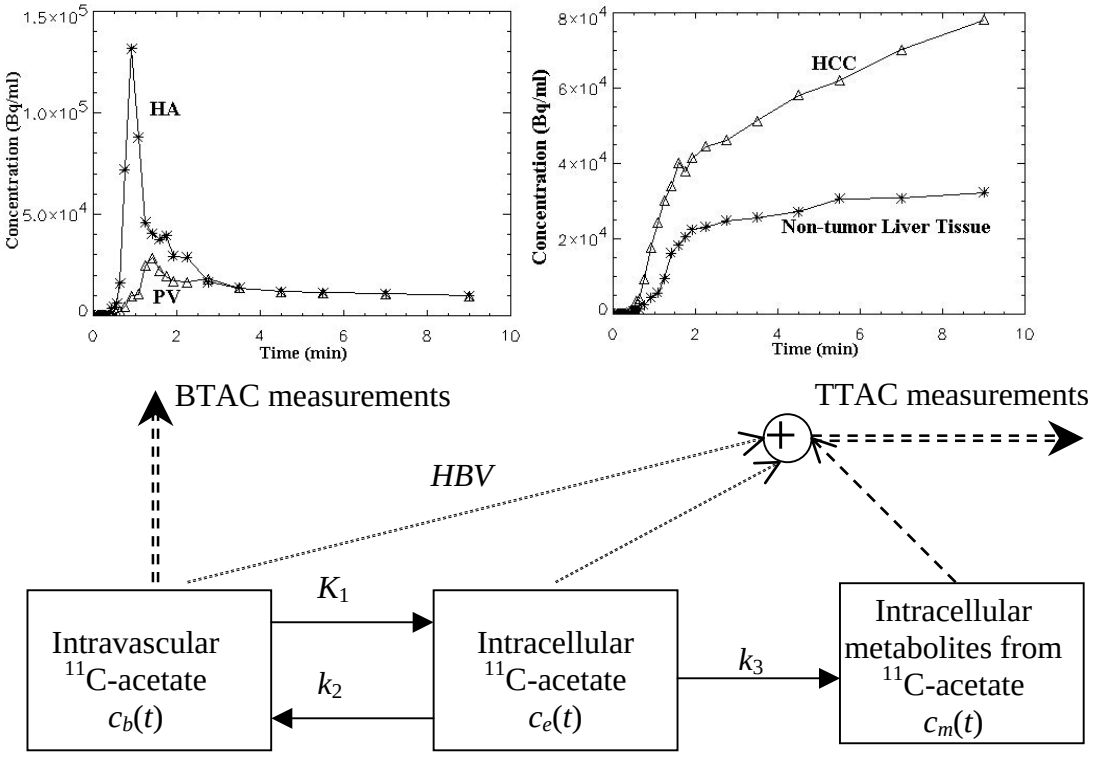

Figure 3- 1: Three-compartment liver kinetic model for ^{11}C-acetate with an extra parameter in the dual-input function. Typical TACs of HA and PV were illustrated in the BATC measurements. The last five points of PV measurements were replaced by the corresponding HA data. Solid line marked by asterisk stands for the HA, triangle for the PV. The greatest activity difference between these two curves is during the early radionuclide angiographic phase. Typical TACs of non-tumor liver tissue and HCC were illustrated in the TTAC measurements. Solid line marked by asterisk stands for the non-tumor liver tissue, triangle for the HCC.

In this study, to obtain the proportion of the portal or arterial contribution to the liver blood supply and provide more accurate physiological parameter estimates, a new parameter called the "relative portal venous contribution to the hepatic blood flow (a_v)" was included in the model input function to describe the contribution of PV to the total hepatic blood supply. Therefore, the contribution

of HA would be (1 - a_v). Thus the dual-input function was calculated according to

$$c_b(t) = (1 - a_v) \times c_a(t) + a_v \times c_v(t) \quad (6)$$

where $c_a(t)$ is the tracer concentration in the HA and $c_v(t)$ is the tracer concentration in the PV. Substituting $c_b(t)$ in equation (5) by equation (6), the equation

$$c_T(t) = (B_1 + B_2 e^{-L_1 t}) \otimes ((1 - a_v)c_a(t) + a_v c_v(t)) + HBV \times ((1 - a_v)c_a(t) + a_v c_v(t)) \quad (7)$$

could be obtained.

3.2.4 Parameter Estimation and Statistical Analysis

Three-compartment 4-P model with an extra parameter a_v in the dual-input function was used to fit the clinical data and compared with the fitting results of the 4-P model using fixed weighted dual-input function. With the measurements of $c_a(t)$, $c_v(t)$ and $c_T(t)$ from dynamic PET images, the weighted non-linear least squares (NLS) algorithm was used to numerically evaluate all the individual parameters. Model parameters were estimated by minimizing the weighted residual sum of squares (WRSS), which is a direct measurement of the fitting quality. WRSS is given by

$$WRSS(p) = \sum_{k=1}^{25} w_k \left[c_T(t_k, p) - z(t_k)\right]^2 \quad (8)$$

where p is the vector of parameters to be estimated, w_k is the weight adopted, which is proportional to the length of the scanning interval and inversely proportional to the radioactivity concentration, c_T is the model output, which is a

function of *p*, and *z* is the PET measurement. The superscript 25 is the total data points to be fitted in this study. *LHMRAct* could be calculated by

$$LHMRAct = \frac{K_1 k_3}{k_2 + k_3} \tag{9}$$

from NLS fitting results.

Patlak analysis [54] was also provided to estimate *LHMRAct* for the two models (with/without a_v) to fit the data between 3 - 10 min. Since Patlak method could not estimate parameter a_v, for the non-fixed weighted dual-input model, the input function was calculated according to the estimated value of a_v by using NLS method. The estimated *LHMRAct* of both models were compared with those obtained from NLS method respectively by correlation analysis.

Apart from *WRSS*, parameter standard deviation (*SD*) and coefficient of variation (*CV*), which are the computed measurements of variability of parameter estimation, were utilized as the statistical criteria. Besides, Akaike Information Criteria (AIC) [52] and Schwarz Criteria (SC) [53] were used to test which model is better. It was assumed that the data variances were known up to a proportionality constant, therefore the AIC and the SC are given by

$$AIC = N \ln(WRSS) + 2N_P \tag{10}$$

$$SC = N \ln(WRSS) + N_P \ln N \tag{11}$$

where N_P is the number of parameters in the model, and N is the number of data points, and *WRSS* is the weighted residual sum of squares.

3.2.5 Simulation Study

Computer simulation was also conducted to test the accuracy and reliability of the estimated parameters of the non-fixed weighted dual-input model. The TACs of both PV and HA were extracted from one clinical dataset. The TTAC was calculated according to (4) by using $K_1 = 0.47$, $k_2 = 0.26$, $k_3 = 0.09$, $HBV = 0.33$, $a_v = 0.72$. The scanning intervals were the same as those in clinical data acquisition. A pseudorandom number generator was used to generate the Gaussian noise added to the calculated TTAC and the noise level was set to 0.1, 0.5 and 1.0 respectively. The mean value of the estimated parameters was calculated from 100 simulation runs, and the bias was calculated by

$$Bias = \left| \frac{P^{true} - \bar{P}}{P^{true}} \right| \tag{12}$$

where P^{true} is the true value of the parameter, and $\bar{P}$ is the mean value from the NLS fitting results of the computer simulation.

3.3 Results and Discussion

The ^{11}C-acetate clinical data of ten ROIs extracted from six patients were analyzed to test the models with fixed/non-fixed weighted dual-input function. The estimated results of the models with 70%, 80% and 85% contribution from PV were summarized in Tables 3-1, 3-2 and 3-3 respectively. In Table 3-2, 80% and 60% contribution from HA for regions 7 and 10 respectively were used;

Table 3- 1: Estimated parameters of the three-compartment 4-P ^{11}C-acetate liver model with 70% contribution from PV using NLS method.

Datasets number	Rate constants			
	K_1 (ml/min/ml)	k_2 (min^{-1})	k_3 (min^{-1})	*HBV* (ml/ml)
1	0.531 ± 0.035	0.232 ± 0.052	0.079 ± 0.040	0.026 ± 0.016
2	0.645 ± 0.046	0.232 ± 0.053	0.058 ± 0.038	0.044 ± 0.022
3	0.696 ± 0.031	0.252 ± 0.031	0.044 ± 0.018	0.015 ± 0.013
4	0.479 ± 0.013	0.262 ± 0.020	0.088 ± 0.013	0.316 ± 0.009
5	0.472 ± 0.029	0.255 ± 0.043	0.077 ± 0.027	0.307 ± 0.018
6	0.791 ± 0.072	0.584 ± 0.092	0.175 ± 0.020	0.262 ± 0.029
7*	1.458 ± 0.129	0.454 ± 0.075	0.115 ± 0.021	0.426 ± 0.059
8	0.920 ± 0.050	0.221 ± 0.037	0.035 ± 0.027	0.074 ± 0.018
9	0.615 ± 0.056	0.283 ± 0.072	0.091 ± 0.042	0.007 ± 0.022
10*	1.185 ± 0.110	0.420 ± 0.117	0.350 ± 0.060	0.234 ± 0.037

* Regions 7 and 10 represent HCC.

Table 3- 2: Estimated parameters of the three-compartment 4-P ^{11}C-acetate liver model with 80% contribution from PV using NLS method.

Datasets number	Rate constants			
	K_1 (ml/min/ml)	k_2 (min^{-1})	k_3 (min^{-1})	*HBV* (ml/ml)
1	0.652 ± 0.048	0.312 ± 0.059	0.085 ± 0.030	0.038 ± 0.020
2	0.731 ± 0.064	0.284 ± 0.065	0.064 ± 0.035	0.047 ± 0.027
3	0.759 ± 0.033	0.290 ± 0.031	0.051 ± 0.016	0.036 ± 0.015
4	0.456 ± 0.019	0.237 ± 0.029	0.075 ± 0.020	0.383 ± 0.012
5	0.461 ± 0.034	0.245 ± 0.052	0.072 ± 0.035	0.367 ± 0.023
6	0.709 ± 0.068	0.509 ± 0.090	0.170 ± 0.023	0.362 ± 0.030
7*	1.251 ± 0.068	0.364 ± 0.046	0.113 ± 0.019	0.125 ± 0.028
8	0.996 ± 0.055	0.254 ± 0.038	0.042 ± 0.024	0.140 ± 0.028
9	0.704 ± 0.073	0.344 ± 0.087	0.102 ± 0.039	0.030 ± 0.029
10*	0.806 ± 0.071	0.280 ± 0.124	0.472 ± 0.132	0.100 ± 0.022

* Regions 7 and 10 represent HCC. The input functions of regions 7 and 10 are 80% and 60% contribution from HA respectively.

Table 3- 3: Estimated parameters of the three-compartment 4-P ^{11}C-acetate liver model with 85% contribution from PV using NLS method.

Datasets number	Rate constants			
	K_1 (ml/min/ml)	k_2 (min^{-1})	k_3 (min^{-1})	*HBV* (ml/ml)
1	0.723 ± 0.061	0.379 ± 0.072	0.104 ± 0.028	0.059 ± 0.024
2	0.740 ± 0.061	0.280 ± 0.063	0.057 ± 0.036	0.063 ± 0.030
3	0.795 ± 0.034	0.316 ± 0.033	0.057 ± 0.016	0.050 ± 0.017
4	0.449 ± 0.028	0.231 ± 0.043	0.072 ± 0.031	0.415 ± 0.018
5	0.462 ± 0.048	0.253 ± 0.070	0.078 ± 0.042	0.394 ± 0.029
6	0.649 ± 0.064	0.448 ± 0.087	0.163 ± 0.025	0.426 ± 0.030
7*	1.396 ± 0.089	0.426 ± 0.056	0.119 ± 0.018	0.185 ± 0.037
8	0.975 ± 0.038	0.224 ± 0.032	0.017 ± 0.028	0.207 ± 0.028
9	0.762 ± 0.080	0.358 ± 0.084	0.083 ± 0.034	0.052 ± 0.033
10*	0.920 ± 0.080	0.334 ± 0.119	0.433 ± 0.097	0.123 ± 0.025

* Regions 7 and 10 represent HCC. The input functions of regions 7 and 10 are 60% and 50% contribution from HA respectively.

60% and 50% contribution from HA was adopted for regions 7 and 10 respectively in Table 3-3. Comparison of the three groups of estimation results according to their *CV* and *WRSS* was conducted. It could be found that generally if the datasets achieving best fitting are from Table 3-1, they always show the worst fitting quality in Table 3-3. On the contrary, if the datasets of best quality are from Table 3-3, they always demonstrate the worst fitting results in Table 3-1. The estimated parameters in Table 3-2 exhibit moderate fitting quality.

The parameter estimates for the model with non-fixed weighted dual-input function were summarized in Table 3-4. It was demonstrated that the estimated a_v value showed moderate variability among different ROIs from non-tumor liver tissue and significant difference between HCC and non-tumor regions ($p < 0.05$). Therefore, non-fixed weighted dual-input function has significant importance to

Table 3- 4: Estimated parameters of the three-compartment ^{11}C-acetate liver model with an extra parameter a_v in the dual-input function using NLS method.

Datasets number	Rate constants				
	K_1 (ml/min/ml)	k_2 (min^{-1})	k_3 (min^{-1})	*HBV* (ml/ml)	a_v
1	0.761 ± 0.140	0.362 ± 0.110	0.071 ± 0.025	0.088 ± 0.046	0.900 ± 0.069
2	0.659 ± 0.102	0.242 ± 0.083	0.059 ± 0.042	0.042 ± 0.028	0.705 ± 0.136
3	0.804 ± 0.064	0.322 ± 0.050	0.058 ± 0.017	0.055 ± 0.030	0.863 ± 0.073
4	0.474 ± 0.016	0.256 ± 0.024	0.085 ± 0.014	0.328 ± 0.018	0.717 ± 0.024
5	0.530 ± 0.052	0.369 ± 0.079	0.142 ± 0.032	0.291 ± 0.054	0.697 ± 0.073
6	0.664 ± 0.105	0.505 ± 0.131	0.187 ± 0.027	0.468 ± 0.078	0.899 ± 0.048
7*	1.360 ± 0.214	0.411 ± 0.101	0.118 ± 0.020	0.157 ± 0.082	0.333 ± 0.247
8	0.979 ± 0.096	0.244 ± 0.046	0.037 ± 0.027	0.136 ± 0.082	0.790 ± 0.106
9	0.827 ± 0.186	0.419 ± 0.151	0.099 ± 0.033	0.048 ± 0.083	0.866 ± 0.110
10*	1.005 ± 0.441	0.366 ± 0.234	0.405 ± 0.118	0.147 ± 0.114	0.568 ± 0.291

* Regions 7 and 10 represent HCC.

the parameter estimation. The mean value of the estimated a_v for non-tumor regions is 0.805, which is comparable with our previous hypothesis in Chapter 2 for the fixed weight 4-P and 5-P models, and the SD is 0.088. The estimated a_v values of the two HCC ROIs are much less than those of the non-tumor liver tissue, indicating that the measurement of a_v might be an alternative noninvasive method to detect HCC. As aforementioned, in cirrhotic livers the blood supply could be obtained from the arteries in a proportion up to 75%, therefore, the measurement of a_v may also provide an indirect way of reflecting cirrhosis using PET (which is normally evaluated by CT). Regarding the comparison stated in the above paragraph, for every dataset, the most accurate estimation among the three fixed-weight fittings is always with the assumed weight that is closest to the estimated a_v value in Table 3-4. For example, the estimated a_v value of region 4 is 0.717 (shown in Table 3-4), the model with 70% contribution from

PV could achieve best fitting quality in terms of *WRSS* and *CV* compared to the other two weight assumptions for region 4; the estimated a_v value of region 9 is 0.866 (shown in Table 3-4), for region 9, the model with 85% contribution from PV could achieve most accurate estimation, which may indicate that the estimated a_v value could be accurate.

The fitting results using the fixed weights in Table 3-2 were focused to be compared with those using non-fixed weighted input model. Compared with the results in Table 3-2, the estimated value of K_1, k_2, k_3 of non-tumor regions in Table 3-4 shows no significant difference respectively, which may due to the fact that the estimated a_v value demonstrates relatively less variance from 80%. For non-tumor liver tissue, the estimated K_1 expressed as mean ± *SD* is 0.684 ± 0.173 ml/min/ml in Table 3-2 and 0.712 ± 0.165 ml/min/ml in Table 3-4; k_2 is 0.309±0.088 /min in Table 3-2 and 0.340 ± 0.094 /min in Table 3-4; k_3 is 0.083 ± 0.040 /min in Table 3-2 and 0.092 ± 0.050 /min in Table 3-4. However, the fitting results of the two HCC regions exhibit relatively great difference especially for region 10, which may due to the significant difference between the estimated a_v value and the fixed weight assumed. It could be found that the two sets of estimated *HBV* value in Tables 3-2 and 3-4 differ greatly because *HBV* is the hepatic blood volume term which is directly affected by the contribution of the hepatic dual inputs. Since the vascularity of cirrhotic liver is heterogeneous, the estimated *HBV* value also exhibits moderate variability [55].

Table 3- 5: Comparison of the *WRSS*, AIC and SC of the models using fixed/non-fixed weighted dual-input function.

Datasets number	*WRSS_change* (%)			AIC**		SC**	
	Table 3-1	Table 3-2	Table3-3	F***	NF***	F	NF
1	51.0	29.9	25.4	181.1	176.5	185.9	182.6
2	-0.8	14.1	22.3	197.4	196.1	202.3	202.2
3	6.0	0.3	-0.2	164.0	166.0	168.9	172.1
4	4.1	84.8	269.0	144.2	130.9	149.1	137.0
5	-39.5	-15.5	21.7	173.6	179.8	178.5	185.9
6	30.5	15.2	2.3	165.2	163.6	170.0	169.7
7*	19.9	-5.5	3.5	189.1	192.5	194.0	198.6
8	-13.4	3.7	-6.0	176.5	177.6	181.4	183.7
9	25.8	17.8	8.0	178.4	176.3	183.3	182.4
10*	-6.2	4.2	2.1	168.5	169.4	173.3	175.5

* Regions 7 and 10 represent HCC.
**Comparison of AIC and SC was between the results with the weights in Table 3-2 and those with the non-fixed weight in Table 3-4.
*** “F” stands for the fixed weight and “NF” stands for the non-fixed weight.

Comparison of the *WRSS*, AIC and SC of the fixed (weights in Table 3-2)/non-fixed weighted models was conducted, the results were summarized in Table 3-5. The “*WRSS_change*” term in Table 3-5 was calculated by

$$WRSS\_change = \frac{WRSS_F - WRSS_N}{WRSS_N} \times 100\% \quad (13)$$

where $WRSS_N$ is the *WRSS* using the non-fixed input model and $WRSS_F$ is the *WRSS* using the fixed input model. As shown in Table 3-5, when parameter a_v was used, *WRSS* (refer to the second column of *WRSS_change*) for all regions except regions 5 and 7 is reduced. Compared to the AIC and SC of the fixed-weight model, half of them in Table 3-4 are smaller. Table 3-6 summarizes the comparison of the *CV* of the estimated parameters in Tables 3-2 and 3-4. Although there is one more parameter in the non-fixed weighted input model, the

Table 3- 6: Comparison of the *CV* of the estimated parameters in Tables 3-2 and 3-4.

Datasets number	K_1 (%)		k_2 (%)		k_3 (%)		*HBV* (%)		a_v (%)
	F**	NF**	F	NF	F	NF	F	NF	NF
1	7.38	18.40	19.02	30.45	34.97	35.64	53.25	52.80	7.70
2	8.73	15.42	23.04	34.36	54.82	70.92	57.73	66.07	19.31
3	4.30	8.01	10.75	15.65	31.75	29.84	42.40	53.97	8.46
4	4.19	3.47	12.11	9.20	26.28	16.56	3.26	5.51	3.30
5	7.38	9.74	21.04	21.46	48.03	22.40	6.19	18.45	10.45
6	9.61	15.87	17.61	25.88	13.46	14.66	8.34	16.65	5.31
7*	5.43	15.71	12.67	24.53	16.79	17.08	22.60	52.18	74.25
8	5.48	9.80	15.17	18.86	56.79	71.47	20.25	60.41	13.39
9	10.37	22.44	25.18	36.03	38.01	33.22	96.86	172.6	12.74
10*	8.82	43.88	44.23	63.92	27.91	29.20	21.60	77.70	51.17

* Regions 7 and 10 represent HCC.
** “F” stands for the fixed weight and “NF” stands for the non-fixed weight.

CV value is still acceptable and additionally about one fourth *CVs* of the estimated parameters (excluding a_v) even decrease. The fitting result of a_v is very reliable since a majority of *CVs* are less than 20%. The model fitted curves according to the fix/non-fixed weighted input models for two datasets: one from HCC, another from non-tumor region, were drawn in Figure 3-2. The 4-P model plus a weight parameter in the required model input function is the better model to characterize the kinetics of ^{11}C-acetate in the liver. The fitting result of the non-fixed weighted model is satisfactory and parameter a_v could be identified by using the tracer kinetic modeling techniques.

The NLS fitting results of the computer simulation using the non-fixed weighted dual-input model were presented in Table 3-7. Parameter estimates

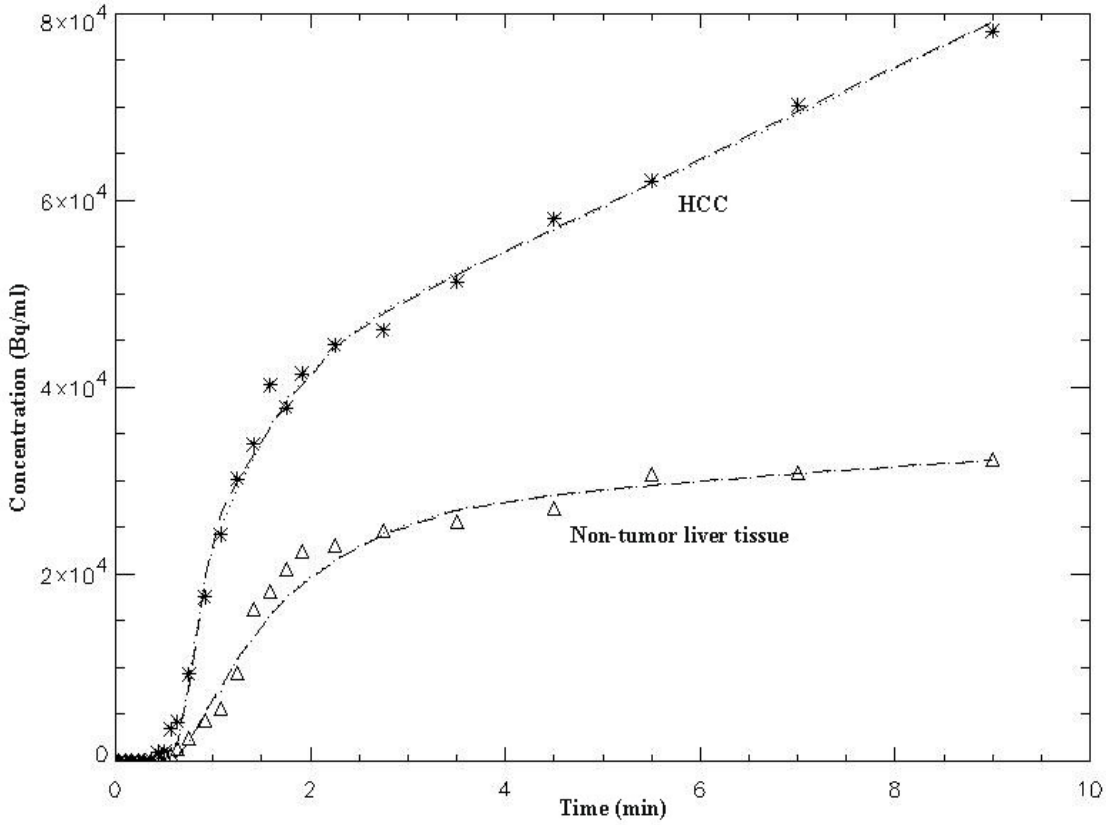

Figure 3- 2: Graph shows the generated TACs of the HCC ROI with symbol "*" and the non-tumor liver tissue ROI with symbol "Δ". While, dashed lines demonstrate the fitting results using the fixed weights in the dual-input function; dotted lines stand for the fitting results using an extra parameter in the input function of the ^{11}C-acetate liver model.

Table 3- 7: NLS fitting results of the computer simulation using non-fixed weighted dual-input model. The mean value, *SD* and *Bias* of K_1-k_3, *HBV*, a_v, *K* were calculated from 100 simulation runs.

Noise level	Rate constants											
	K_1	*Bias*	k_2	*Bias*	k_3	*Bias*	*HBV*	*Bias*	a_v	*Bias*	*K*	*Bias*
0.1	0.4699±0.0034	0.0002	0.2600±0.0045	0.0000	0.0901±0.0023	0.0007	0.3305±0.0050	0.0016	0.7205±0.0067	0.0007	0.1209±0.0016	0.0002
0.5	0.4693±0.0173	0.0015	0.2597±0.0226	0.0011	0.0897±0.0118	0.0028	0.3323±0.0251	0.0071	0.7210±0.0343	0.0014	0.1202±0.0085	0.0054
1	0.4692±0.0352	0.0016	0.2606±0.0454	0.0023	0.0890±0.0231	0.0115	0.3336±0.0500	0.0110	0.7180±0.0703	0.0028	0.1181±0.0176	0.0228

were expressed as mean ± *SD*. As seen in Table 3-7, both the *CV* and *bias* of all the estimated parameters from 100 simulation runs are very small, therefore reliable and accurate parameter estimation of the non-fixed weighted dual-input model could be achieved by using NLS method.

The ten clinical datasets were also fitted with the Patlak method using the fixed (weights in Table 3-2)/non-fixed weighted dual-input function. Due to the nature of Patlak method, the data of the early phase (< 3 min) were not included in the analysis. The results of the estimated *LHMRAct* (the forward clearance *K*) for the two models using the NLS and Patlak methods were presented in Table 3-8. Since the TACs of the HA and PV are similar after the dynamic phase [4], the estimated *K* using the Patlak method is affected less by the duall-input function, the non-fixed input model shows less difference with the fixed input model. For the eight ROIs from the non-tumor liver tissue, the estimated *K* value expressed as mean ± *SD* with/without a_v is 0.1611±0189 and 0.1612±0.0200 ml/min/ml respectively. For the two ROIs of HCC, the estimated forward clearance *K* by the Patlak method with/without weight parameter is 0.2728 and 0.2694 ml/min/ml (region 7), 0.5066 and 0.4945 ml/min/ml (region 10). For NLS analysis, the results do show a little difference between the two models. For the eight ROIs from the non-tumor liver tissue, the estimated *K* value expressed as mean ± *SD* with/without a_v is 0.1388±0.0212 and 0.1351±0.0256 ml/min/ml respectively. For the two ROIs of HCC, the estimated *K* value with/without weight parameter is 0.3025 and 0.2969 ml/min/ml (region 7), 0.5278 and 0.5057 ml/min/ml (region 10). The correlation coefficients between the estimated *K* value of Patlak and NLS methods for the fixed and non-fixed input models is 97.67% and 98.21%

Table 3- 8: Estimated *K* value for the models with fixed (weights in Table 3-2) /non-fixed weighted dual-input function using the NLS and Patlak methods respectively.

Datasets number	Estimated K $(K_1k_3/(k_2+k_3))$			
	NLS method using fixed weighted inputs	Patlak method using fixed weighted inputs	NLS method using non-fixed weighted inputs	Patlak method using non-fixed weighted inputs
1	0.1398	0.1642	0.1250	0.1642
2	0.1345	0.1826	0.1300	0.1773
3	0.1130	0.1548	0.1228	0.1587
4	0.1095	0.1562	0.1182	0.1552
5	0.1046	0.1495	0.1472	0.1483
6	0.1775	0.1664	0.1797	0.1679
7*	0.2969	0.2694	0.3025	0.2728
8	0.1405	0.1259	0.1296	0.1270
9	0.1609	0.1903	0.1580	0.1898
10*	0.5057	0.4945	0.5278	0.5066

* Regions 7 and 10 represent HCC.

respectively. Same as in Chapter 2, the *K* value of the non-FDG-avid type of HCC (regions 7 and 10) is significantly higher than those of the non-tumor liver parenchyma ($p < 0.05$). Therefore, quantitative parametric imaging of *LHMRAct* could be a potential functional imaging technique to detect HCC.

3.4 Conclusion

This study suggests that the differential portal and arterial contribution to the liver blood supply could be extracted from the dynamic PET measurements noninvasively using tracer kinetic modeling techniques. The estimated a_v value is reasonable and concordant with the clinical, radiological and pathological

conditions. It adds supportive evidence to the observation that liver metastases derive a much greater proportion of their blood supply from the hepatic arterial flow when neovascularization is a common cancer growth characteristic, with a smaller proportion from the portal venous flow. Whether the estimated a_v value might have an alternative role as a vascular indicator that can reflect subtle neovascularization in early HCC tumor growth requires more research. In the presence of pathological changes of cirrhosis, the background liver parenchyma shows heterogeneous vascular changes such as significant arterioportal and portovenous systemic shunting. All these confounding factors will add to the complexity of background noise, making it difficult to evaluate for small and well- differentiated HCC lesions. This is the same reason for a low detection accuracy even by the most advanced triple-phase CT technology when severe hepatic cirrhosis is encountered. The measurement of a_v, however, may directly provide a measure of the "vascular deviation" status from the normal liver vasculature, and, therefore, may provide an indirect way of reflecting cirrhosis using PET (which is normally evaluated by CT). The presented results show that all the required parameters can be quantified simultaneously and the parameter estimates are reliable and accurate. The three-compartment four-parameter model plus an extra weight parameter in the dual-input function is a more appropriate representation of the physiological system by describing the kinetic characters of ^{11}C-acetate in a 10-minute dynamic PET imaging of the liver, including a more consistent estimation of *LHMRAct*. In summary, the above findings and proposal may provide a better understanding of the perfusion and metabolic function of normal liver and liver cancer.

Chapter 4 Fast Parametric Imaging Algorithm for Dual-Input Biomedical System Parameter Estimation

4.1 Introduction

Quantitative functional imaging with dynamic positron emission tomography (PET) has been playing an important role in modern biomedical research and has revolutionized clinical diagnosis [70]. Dynamic PET imaging provides the ability to construct functional images of various kinds of physiological and biochemical parameters [71], [72]. One of the key issues in functional imaging is to estimate parameters at the pixel-by-pixel level from certain processes described by dynamic continuous-time models for certain biosystems, which is widely acknowledged as biomedical system identification [73]-[75]. In biosystem identification, the task is to develop a valid mathematical model, usually represented by a set of differential equations, capable of describing the essential properties of the system with sufficient accuracy and in useful form [76] and estimate the parameters within the dynamic models [77].

The present algorithms to construct parametric images with nonuniformly sampled PET data are based on the kinetic analysis of changes in the tracer

concentration in regional tissue [78]. The classic nonlinear least squares regression (NLS) algorithm is widely adopted and can provide optimum estimation quality [79]. Nevertheless, when the number of parameters to be estimated is relatively large, “good” initial guess is required and the computational burden is considerable, which limits its application in clinical environments for image-wide parameter estimation. For the generation of parametric images, computationally efficient and statistically reliable algorithms have been developed. The well-known Patlak graphical approach [54] assumes that the dynamic process is linear when a unidirectional transfer process is dominant during the scanning period and could estimate the combination of the rate constants. However, this simplification may cause underestimation when the reverse transfer process could not be ignored and this method could not provide estimates for individual kinetic parameters. The linear least squares (LLS) method is potential to be optimal when the measurement noise is low [80], which may not be true in the clinical PET studies, and the estimation is biased due to the colored noise. The integrated projection [81] and weighted integration methods (WIM) [82] could provide the parameter estimates efficiently. However, the estimation results are biased and it is infeasible to predetermine the optimal weighting functions in WIM fitting procedure. Feng *et al.* [74] proposed an unbiased parametric imaging algorithm: generalized linear least squares (GLLS) for nonuniformly sampled biomedical system parameter estimation. However, when the clinical PET data is very noisy, parameter estimation may not converge to reasonable values. Later, a bound GLLS (B-GLLS) algorithm for parametric imaging was presented to guarantee the convergence [72]. All these computationally efficient techniques focus on single input systems and could not

provide optimal solution for dual-input biomedical systems, such as the metabolic system of the "power house" of the human body: liver.

The liver has a dual source of blood supply, receiving oxygenated blood from the common left and right hepatic arteries (HAs) and nutrient-rich blood via the portal vein (PV) [45]. Therefore, the use of arterial input may, however, introduce systematic errors in the estimated kinetic parameters because of the ignorance of the hepatic dual blood supply from the HA and PV to the liver [4]. To achieve more accurate quantitative analysis, in Chapter 3, the actual proportion of portal/arterial contribution to the liver dual blood supply was investigated and a parameter denoted as the *relative portal venous contribution to the hepatic blood flow* (a_v) was introduced into the dual-input function. Previous modeling studies in Chapters 2 and 3 have suggested that the "*local hepatic metabolic rate-constant of acetate* (*LHMRAct*)" (the forward clearance *K*) and a_v could be the potential indicators to detect hepatocellular carcinoma (HCC). Therefore, it is of great interest to develop fast parametric imaging algorithms for the dual-input biomedical system identification.

In this chapter, a rapid estimation algorithm of dual-input-GLLS (D-I-GLLS) for dual-input liver system was proposed. ^{11}C-acetate kinetic model in liver with Parameter a_v in the dual-input function presented in Chapter 3 was utilized to test the algorithm. Its performance was evaluated by comparison with the fitting quality of NLS method.

4.2 Methods

4.2.1 Dual-Input Generalized Linear Least Squares Algorithm

The tracer kinetic model that describes the behavior of ^{11}C-acetate in liver has been presented in Chapter 3. The model consists of three compartments and five parameters including parameter a_v in the dual-input function. The differential equations for the continuous-time model could be referred to section 3.2.3 "^{11}C-Acetate Liver Model with a Non-fixed Weighted Dual-input Function".

The D-I-GLLS technique involves the D-I-LLS estimation and refining the linear estimation results. The dual-input-single-output (DISO) linear ^{11}C-acetate liver kinetic model can be described by the following second-order differential equation

$$c_T''(t) = HBV \times c_b''(t) + \left[K_1 + (k_2 + k_3)HBV\right] \times c_b'(t) + K_1 k_3 \times c_b(t) - (k_2 + k_3) c_T'(t) \quad (1)$$

Let

$$P_0 = HBV$$
$$P_1 = K_1 + (k_2 + k_3)HBV$$
$$P_2 = K_1 k_3$$
$$P_3 = k_2 + k_3$$

then

$$c_T''(t) = P_0 \times c_b''(t) + P_1 \times c_b'(t) + P_2 \times c_b(t) - P_3 \times c_T'(t) \quad (2)$$

Substitute $c_b(t)$ in equation (2) by the dual-input function in section 3.2.3, and assume zero initial condition which holds for most cases [74], we obtain

$$c_T(t) = P_0 \times c_a(t) + P_4(c_v(t) - c_a(t)) + P_1 \int_0^t (c_a(\tau) \times (1 - a_v) + c_v(\tau) \times a_v) d\tau + P_2 \int_0^t \int_0^t (c_a(\tau) \times (1 - a_v) + c_v(\tau) \times a_v) d\tau^2 - P_3 \int_0^t c_T(\tau) d\tau \quad (3)$$

where $P_4=HBV \times a_v$. To provide the LLS solution for the dual-input model, assume a_v= "initial guess" in the third and fourth terms of equation (3), digitalize equation (3) at the sampling time t_i (i=0, 1, 2, … , m), the linear equation in matrix form is

$$y = X\theta + \xi \quad (4)$$

where $\xi=[\xi_0, \xi_1, \ldots, \xi_m]^T$ are the equation errors, $y=[c_T(t_0), c_T(t_1), \ldots, c_T(t_m)]^T$ are the PET measurements at time t_0, t_1, … , and t_m, $\theta=[P_0, P_1, P_2, P_3, P_4]^T$ are the parameters to be estimated and X is the coefficient matrix

$$X = \begin{bmatrix} c_a(t_0) & \int_0^{t_0} \hat{c}_b(\tau) d\tau & \int_0^{t_0} \int_0^{\tau} \hat{c}_b(s) ds d\tau & -\int_0^{t_0} c_T(\tau) d\tau & (c_v(t_0) - c_a(t_0)) \\ c_a(t_1) & \int_0^{t_1} \hat{c}_b(\tau) d\tau & \int_0^{t_1} \int_0^{\tau} \hat{c}_b(s) ds d\tau & -\int_0^{t_1} c_T(\tau) d\tau & (c_v(t_1) - c_a(t_1)) \\ \vdots & & & & \\ c_a(t_m) & \int_0^{t_m} \hat{c}_b(\tau) d\tau & \int_0^{t_m} \int_0^{\tau} \hat{c}_b(s) ds d\tau & -\int_0^{t_m} c_T(\tau) d\tau & (c_v(t_m) - c_a(t_m)) \end{bmatrix} \quad (5)$$

The dual-input function in the second and third columns of X was calculated by the initial guess of a_v. The D-I-LLS solution for θ is

$$\hat{\theta}_{D-I-LLS} = \left(X^T X\right)^{-1} X^T y \quad (6)$$

where $\hat{\theta}_{D-I-LLS}$ denotes the estimated θ in the D-I-LLS sense.

To refine the D-I-LLS estimation results, the correlated equation noise should be whitened. The second-order differential equation of the DISO linear ^{11}C-acetate liver kinetic model is

$$c_T''(t) = P_0 \times c_a''(t) + P_0 a_v (c_v''(t) - c_a''(t)) + P_1 \times c_a'(t) + P_1 a_v (c_v'(t) - c_a'(t)) + P_2 \times c_a(t) + P_2 a_v (c_v(t) - c_a(t)) - P_3 \times c_T'(t) \quad (7)$$

Two terms are "redundant" since there are only five independent variables, whereas seven terms are included in the right hand side of the above equation. Those "redundant" terms can be eliminated by assuming $\hat{P}_0 \to P_0, \hat{P}_1 \to P_1, \hat{P}_2 \to P_2$ in the second, fourth and sixth terms of equation (7), where $\hat{P}_0$, $\hat{P}_1$ and $\hat{P}_2$ are the estimated parameters from the previous iteration, then we have

$$c_T''(t) = P_0 \times c_a''(t) + P_1 \times c_a'(t) + P_2 \times c_a(t) + a_v (\hat{P}_0 (c_v''(t) - c_a''(t)) + \hat{P}_1 (c_v'(t) - c_a'(t)) + \hat{P}_2 (c_v(t) - c_a(t))) - P_3 \times c_T'(t) \quad (8)$$

Take the Laplace transform of equation (8), whiten the correlated equation errors using Filter $s(s + \hat{P}_3)$ in s domain [74], and then take the inverse Laplace transform, the time domain input-output relationship could be given by

$$c_T(t) - \hat{P}_3 \psi_1 \otimes c_T(t) = P_0 \left(c_a(t) - \hat{P}_3 \psi_1 \otimes c_a(t)\right) + P_1 \psi_1 \otimes c_a(t) + P_2 \psi_2 \otimes c_a(t) - P_3 \psi_1 \otimes c_T(t) + a_v \left(\hat{P}_0 (c_v(t) - c_a(t)) + (\hat{P}_1 - \hat{P}_0 \hat{P}_3) \psi_1 \otimes (c_v(t) - c_a(t)) + \hat{P}_2 \psi_2 \otimes (c_v(t) - c_a(t))\right) \quad (9)$$

where

$$\psi_1 = e^{-\hat{P}_3 t}$$

$$\psi_2 = \frac{1}{\hat{P}_3}(1 - e^{-\hat{P}_3 t})$$

Digitalize equation (9) at the sampling time as in D-I-LLS fitting procedure, we have

$$r = Z\theta + \zeta \tag{10}$$

where θ=[P_0, P_1, P_2, P_3, a_v]^T are the parameters to be estimated, ζ is the filtered equation noise, r is filtered PET measurements

$$r = \begin{bmatrix} c_T(t_0) - \hat{P}_3\psi_1 \otimes c_T(t_0) \\ c_T(t_1) - \hat{P}_3\psi_1 \otimes c_T(t_1) \\ \vdots \\ c_T(t_m) - \hat{P}_3\psi_1 \otimes c_T(t_m) \end{bmatrix} \tag{11}$$

and Z is the coefficient matrix

$$Z = \begin{bmatrix} (c_a(t_0) - \hat{P}_3\psi_1 \otimes c_a(t_0)) & \psi_1 \otimes c_a(t_0) & \psi_2 \otimes c_a(t_0) & -\psi_1 \otimes c_T(t_0) & (\hat{P}_0 c_g(t_0) + (\hat{P}_1 - \hat{P}_0\hat{P}_3)\psi_1 \otimes c_g(t_0) + \hat{P}_2\psi_2 \otimes c_g(t_0)) \\ (c_a(t_1) - \hat{P}_3\psi_1 \otimes c_a(t_1)) & \psi_1 \otimes c_a(t_1) & \psi_2 \otimes c_a(t_1) & -\psi_1 \otimes c_T(t_1) & (\hat{P}_0 c_g(t_1) + (\hat{P}_1 - \hat{P}_0\hat{P}_3)\psi_1 \otimes c_g(t_1) + \hat{P}_2\psi_2 \otimes c_g(t_1)) \\ \vdots & & & & \\ (c_a(t_m) - \hat{P}_3\psi_1 \otimes c_a(t_m)) & \psi_1 \otimes c_a(t_m) & \psi_2 \otimes c_a(t_m) & -\psi_1 \otimes c_T(t_m) & (\hat{P}_0 c_g(t_m) + (\hat{P}_1 - \hat{P}_0\hat{P}_3)\psi_1 \otimes c_g(t_m) + \hat{P}_2\psi_2 \otimes c_g(t_m)) \end{bmatrix} \tag{12}$$

where

$$c_g(t) = c_v(t) - c_a(t)$$

The parameter estimates are

$$\hat{\theta}_{D-I-GLLS} = \left(Z^T Z\right)^{-1} Z^T r \tag{13}$$

where $\hat{\theta}_{D-I-GLLS}$ represents the estimated parameters in the D-I-GLLS sense. The estimation results of D-I-LLS would be used as the initial values for the first iteration of the above estimation procedures and the subsequent estimates are refined by the same procedure until the convergence criteria are satisfied. The flow chart of the proposed D-I-GLLS algorithm for dual-input continuous system parameter estimation was shown in Figure 4-1.

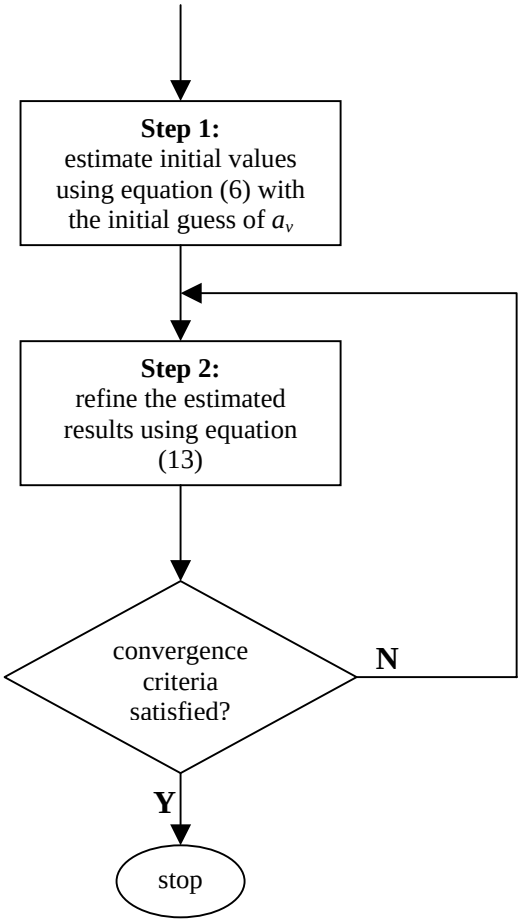

Figure 4- 1: The flow chart of the D-I-GLLS algorithm for the dual-input continuous system parameter estimation.

4.2.2 Simulation Study

Computer simulation was conducted to test the D-I-GLLS algorithm. Two computer simulated datasets representing HCC and non-tumor liver tissue with two image-derived dual-input functions obtained from clinical data, were recruited in this study. The simulation data were generated by the sampling

protocol which is the same as the image acquisition sequences in Chapter 2. A pseudorandom number generator was employed to generate the Gaussian noise added to the calculated tissue time-activity curves (TTACs) with the noise levels 0.1, 0.5 and 1.0. The noise level represents the proportional constant in the variance of the generated noise.

4.2.3 Statistical Criteria

The reliability and accuracy of the parameter estimates obtained by the proposed D-I-GLLS technique were evaluated by the coefficient of variation (*CV*) and *bias* calculated from 200 simulation runs for each noise level. The *CV* of a parameter estimate was defined as

$$CV_{\bar{P}} = \frac{SD_{\bar{P}}}{\bar{P}} \times 100\% \tag{14}$$

where $\bar{P}$ is the mean value of the parameter estimates over 200 runs and $SD_{\bar{P}}$ is the standard deviation of $\bar{P}$, and the *bias* is calculated by

$$Bias = \left| \frac{P^{true} - \bar{P}}{P^{true}} \right| \times 100\% \tag{15}$$

where P^{true} denotes the true value of *P*, and $\bar{P}$ is the mean value. The simulation runs were also conducted with NLS fitting for comparisons.

4.3 Results and Discussion

Estimation results of K_1-k_3, *HBV*, a_v and *LHMRAct* (the forward clearance *K*) by D-I-GLLS and NLS methods were summarized in Table 4-1. As seen in Table 4-1, the reliability of the estimated parameters by the two methods is generally comparable with each other; while the accuracy of the parameter estimates provided by the D-I-GLLS is generally slightly worse than that by NLS fitting procedure.

The accuracy of the estimated rate constant parameters K_1-k_3 by D-I-GLLS is satisfactory since the maximum *bias* of these estimated parameters is 5% when the noise level is 1 for the estimation of k_2 of the HCC data. The fitting quality in terms of *CV* and *bias* of these parameters estimated by the D-I-GLLS technique are satisfactory. The accuracy of the estimation of *HBV* is moderately worse than that provided by NLS method. As revealed by Table 4-1, although the *bias* of the estimated a_v is generally slightly more than that by NLS, the accuracy is still satisfactory since the maximum *bias* is 3.4%. Furthermore, Parameter a_v for the non-tumor liver tissue data could be more accurately estimated by D-I-GLLS algorithm when the noise level is 1. The reliability of the estimated a_v is satisfactory as well especially for the non-tumor liver tissue data. As indicated in Table 4-1, Parameter *LHMRAct* (the forward clearance *K*) could be estimated accurately and reliably and the estimation quality is comparable with the most optimum NLS estimation.

Table 4- 1: Estimation results of K_1-k_3, *HBV*, a_v and K from two sets of simulation. $P_{\text{t-true}}$ and $P_{\text{n-true}}$ represent the true values of the parameters for HCC and non-tumor liver tissue respectively. The estimated parameters in the table are their mean values. The values of *CV* and *bias* are the percentage values. The mean values, *biases* ($bias_1$, $bias_2$, $bias_3$, $bias_H$, $bias_a$, $bias_K$), and *CVs* (CV_1, CV_2, CV_3, CV_H, CV_a, CV_K) were calculated from 200 simulation runs. "D-G" is the abbreviation of "D-I-GLLS".

Method	K_1	$bias_1$	CV_1	k_2	$bias_2$	CV_2	k_3	$bias_3$	CV_3	*HBV*	$bias_H$	CV_H	a_v	$bias_a$	CV_a	K	$bias_K$	CV_K
$P_{\text{t-true}}$	1.35	---	---	0.40	---	---	0.11	---	---	0.20	---	---	0.40	---	---	0.2912	---	---
Noise level α=0.1																		
NLS	1.3499	0.0061	1.39	0.4000	0.0081	2.10	0.1100	0.0202	1.38	0.1997	0.1685	5.56	0.3993	0.1869	6.44	0.2912	0.0038	0.66
D-G	1.3378	0.9013	1.25	0.3966	0.8481	1.91	0.1099	0.1090	1.28	0.2187	9.3508	5.58	0.4070	1.7474	6.36	0.2902	0.3226	0.60
Noise level α=0.5																		
NLS	1.3457	0.3163	6.82	0.3991	0.2262	10.40	0.1097	0.2290	6.99	0.2031	1.5648	28.23	0.3920	2.0015	32.41	0.2903	0.3126	3.38
D-G	1.3262	1.7603	6.04	0.3917	2.0725	9.34	0.1088	1.1317	6.60	0.2288	14.413	27.82	0.4038	0.9539	32.39	0.2882	1.0202	3.12
Noise level α=1																		
NLS	1.3365	0.9988	11.70	0.3977	0.5660	18.16	0.1092	0.7488	14.13	0.2262	13.124	62.08	0.3920	2.0104	60.15	0.2875	1.2671	7.12
D-G	1.2980	3.8507	11.82	0.3800	4.9914	18.33	0.1058	3.7796	14.39	0.2498	24.898	55.78	0.3862	3.4444	69.20	0.2825	2.9679	7.06
$P_{\text{n-true}}$	0.50	---	---	0.30	---	---	0.10	---	---	0.30	---	---	0.70	---	---	0.1250	---	---
Noise level α=0.1																		
NLS	0.5000	0.0052	0.68	0.3001	0.0189	1.62	0.1000	0.0442	2.30	0.3000	0.0142	1.70	0.7000	0.0054	1.22	0.1250	0.0067	1.12
D-G	0.4954	0.9279	0.83	0.2962	1.2709	2.06	0.0991	0.9074	2.99	0.3046	1.5315	1.93	0.7023	0.3271	1.25	0.1242	0.6663	1.46
Noise level α=0.5																		
NLS	0.4994	0.1156	3.47	0.2999	0.0185	8.33	0.0997	0.2588	11.77	0.3001	0.0373	8.54	0.6979	0.2996	6.33	0.1244	0.4807	5.83
D-G	0.4968	0.6494	4.33	0.2975	0.8306	10.35	0.0986	1.3589	15.20	0.3062	2.0605	9.64	0.7040	0.5744	6.32	0.1233	1.3789	7.90
Noise level α=1																		
NLS	0.4976	0.4839	7.10	0.2991	0.3008	16.98	0.0984	1.5945	23.84	0.3004	0.1236	17.52	0.6902	1.4006	14.45	0.1222	2.2459	12.33
D-G	0.4934	1.3233	8.71	0.2945	1.8422	21.13	0.0950	4.9538	32.54	0.3073	2.4440	19.40	0.6986	0.2068	14.32	0.1180	5.5729	20.34

All the estimated parameters could be expressed analytically in terms of the PET measurements by the D-I-GLLS technique, therefore, the fitting procedure is significantly faster than NLS regression. The number of the iteration needed is generally less than 5, which would be very practical for image-wide parameter estimation in the clinical environments.

4.4 Conclusion

In this chapter, a fast parametric imaging algorithm of D-I-GLLS for dual-input biomedical system identification was proposed. It achieves a comparable estimation quality in terms of coefficient of variance with NLS method. The accuracy of most of the parameter estimates for ^{11}C-Acetate liver kinetic model is satisfactory. This computationally efficient algorithm could reliably identify all the parameters including the parameter in the dual-input function. Only one initial guess is required for the fitting procedure and the results are not sensitive to this initial guess. Therefore, this D-I-GLLS algorithm is potentially useful for the construction of parametric images from ^{11}C-acetate dynamic liver PET images and is generally applicable to other dual-input biomedical system parameter estimation.

Chapter 5 Novel Parameter Estimation Methods for ^{11}C-Acetate Dual-Input Liver Model with Dynamic PET

5.1 Introduction

The extraordinary innovation in modern molecular imaging techniques used to explore the inner world of cells, such as positron emission tomography (PET), makes them increasingly formidable in clinical settings. Due to its great potential for high quality imaging and its ability to extract *in vivo* the molecular and quantitative physiological information from complex dynamic processes in humans using various PET tracers, PET has been proven very promising for the early evaluation of the distribution of malignant tumors. The main focus of PET for the study of liver diseases remains on the detection of liver tumors [6], [25], [84], [85]. Recent clinical studies [6] revealed that the detection of hepatocellular carcinoma (HCC) could be greatly aided by the introduction of a dual-isotope PET protocol: ^{18}F-fluorodeoxyglucose (FDG) and ^{11}C-acetate. In the succedent ^{11}C-acetate liver modeling studies in Chapter 2, the "*local hepatic metabolic rate-constant of acetate* (*LHMRAct*)" was introduced and validated as the potential indicator for detecting HCC. Chapter 3 improved the parameter estimation accuracy and quantified the individual relative PV/HA contribution to

the total liver blood supply by involving a parameter called the "*relative portal venous contribution to the hepatic blood flow* (a_v)" in the model dual-input function. It was proved that the measurement of a_v using dynamic ^{11}C-acetate-PET images could provide an alternative method for the detection of HCC.

In the previous quantitative studies, all the individual parameters were estimated by the weighted nonlinear least squares (NLS) algorithm. However, five parameters need to be estimated simultaneously, which is a difficult task for the weighted NLS fitting procedure. The computational burden is considerable, the fitting results are sensitive to the initial guess, and some estimates are not quite reliable, which limits its application in the clinical environment and is not practical for generating the parametric images. Therefore, statistically reliable and computationally efficient estimation algorithms are much desired for the ^{11}C-acetate liver model with dual hepatic blood supply.

With the development of high spatial and temporal resolution PET, several alternative rapid parameter estimation schemes for the use of dynamic PET molecular images were proposed [54], [74], [80] - [82], [86] - [88]. As concluded in Chapter 2, the back conversion from the ^{11}C-acetate products/metabolites to the free ^{11}C-acetate in liver cells could be ignored, the well-known Patlak method [54] could be applied to estimate *LHMRAct*. However, the individual parameters are not obtainable, especially a_v which has superior diagnostic value for evaluating HCC. In addition, more accurate estimation of *LHMRAct* requires the individual a_v value rather than the predetermined fixed a_v value to calculate the dual-input function. The integrated projection [81] and the linear least squares

(LLS) methods could provide the parameter estimates efficiently, however, they are very biased when applied to the clinical PET images which are noisy and nonuniformly sampled. Although the weighted integration method (WIM) [82] is generally applicable in clinical settings, it is infeasible to predetermine the optimal weighting functions [74]. Feng *et al.* [74] proposed an unbiased fast parameter estimation algorithm: generalized linear least squares (GLLS) for nonuniformly sampled biomedical system, which is particularly useful in image-wide (pixel-by-pixel based) parameter estimation. Despite all the advances in computationally efficient techniques, they are limited in their clinical application to identify the conventional single-input systems, which are not applicable for the dual blood supply liver system, therefore, extra effort is needed to develop parameter estimation methods for the dual-input biomedical systems.

As revealed in Chapter 2, the model with no account for the back conversion from the ^{11}C-acetate products/metabolites to the free ^{11}C-acetate in liver cells could better describe the tracer molecular kinetics in liver, therefore, it may be very valuable to extract the information that could be provided by the linear graphical analysis and consider the result as a *prior*. In this chapter, two potential parameter estimation techniques: graphed nonlinear least squares (GNLS) and graphed dual-input generalized linear least squares (GDGLLS) were proposed. The performance of these two novel algorithms was tested by the clinical PET images and simulated data with comparison to the standard NLS method for the measurement of *LHMRAct*, a_v and all the other individual model parameters.

5.2 Methods

5.2.1 ^{11}C-Acetate Dual-Input Model in Liver

The tracer kinetic model describing distribution of labeled ^{11}C-acetate in liver was shown in Figure 5-1. $c_b(t)$ is the weighted ^{11}C-acetate concentration from the dual hepatic blood supply in intravascular space, $c_e(t)$ is the free ^{11}C-acetate concentration in intracellular space, $c_m(t)$ is the intracellular ^{11}C-acetate products/metabolites concentration, and $c_T(t)$ is the observed total tissue time activity. The first-order mathematical equations governing the model were described by section 3.2.3. In terms of macroparameters, the observed total tissue time activity $c_T(t)$ could be expressed as

$$c_T(t) = (B_1 + B_2 e^{-L_1 t}) \otimes c_b(t) + HBV \times c_b(t) \quad (1)$$

where

$$B_1 = \frac{K_1 k_3}{k_2 + k_3}$$
$$B_2 = \frac{K_1 k_2}{k_2 + k_3}, \qquad L_1 = k_2 + k_3$$

are the macroparameters of the model and $\otimes$ denotes the operation of temporal convolution. When K_1 - k_3 are estimated, the physiological parameter *LHMRAct* can be calculated by

$$LHMRAct = \frac{K_1 k_3}{k_2 + k_3} \quad (2)$$

which has the same form as the forward clearance *K*.

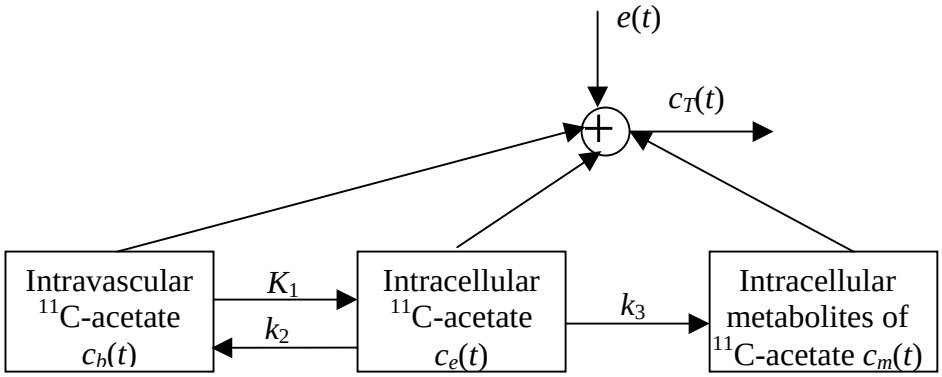

Figure 5- 1: The three-compartment ^{11}C-acetate liver kinetic model with parameter a_v in the dual-input function. *e(t)* denotes the PET measurement noise.

5.2.2 Graphed Nonlinear Least Squares Algorithm

As aforementioned, ^{11}C-acetate is metabolized irreversibly in liver cells with a rate constant of k_3 during the scanning period, therefore, beyond the dynamic phase of the dual-input, the ratio of $c_T(t)$ to $c_b(t)$ could be described by

$$\frac{c_T(t)}{c_b(t)} = \frac{K}{c_b(t)} \int_0^t c_b(\tau) d\tau + \frac{K_1 k_2}{(k_2 + k_3)^2} + HBV \qquad (3)$$

where

$$K = \frac{K_1 k_3}{k_2 + k_3}$$

which is denoted as *LHMRAct* as well. As shown in equation (3), it might be very useful to obtain the forward clearance K by a graph of the ratio of the total tracer concentration in tissue at the midtimes of sampling to the tracer concentration in blood at the respective times versus the ratio of the blood tracer

concentration time integral to the tracer multiple-time (midtimes of sampling) activity data in blood. As illustrated in equation (1), B_1 has the same form as the forward clearance K, therefore, B_1 may be estimated by this linear graphical analysis.

Our proposed GNLS approach applied to the dual-input ^{11}C-acetate liver model is a cascaded estimation algorithm, which has three steps, whose flow chart was shown in Figure 5-2. In the first step, linear graphical analysis is applied to estimate B_1 by equation (3). The ratio of $c_T(t)$ to $c_b(t)$ changes rapidly during the dynamic phase of the tracer activity in blood, therefore, the data to be fitted should belong to the input steady-state space. In this study, the fitting period was from 3 min to 10 min. To calculate the dual-input function in equation (3), a_v was empirically set to be 0.8 for the first iteration. During the graphical fitting period, the two blood time-activity curves (TACs) are almost virtually identical [4], therefore, the estimated B_1 is less affected by the actual PV contribution ratio (a_v), and furthermore, it is well accepted that the estimates by the linear graphical analysis are very robust [54]. Therefore, it is reasonable to consider the estimated B_1 by step 1 as a *prior* for the subsequent estimation schemes. In the second step, the weighted NLS algorithm is utilized to estimate *HBV*, a_v and the other two macroparameters: B_2 and L_1 with the known B_1, which aims to minimize the weighted residual sum of squares (WRSS). The weight used in this step was

$$w_i = \frac{\Delta t_i}{c_T(t_i)} \qquad i = 1,2,...,25 \qquad (4)$$

where $\Delta t_i = t'_i - t'_{i-1}$ is the scanning interval and $c_T(t_i)$ is the total tracer concentration in tissue at the midtimes of sampling time t'_i. As seen in Figure 5-2,

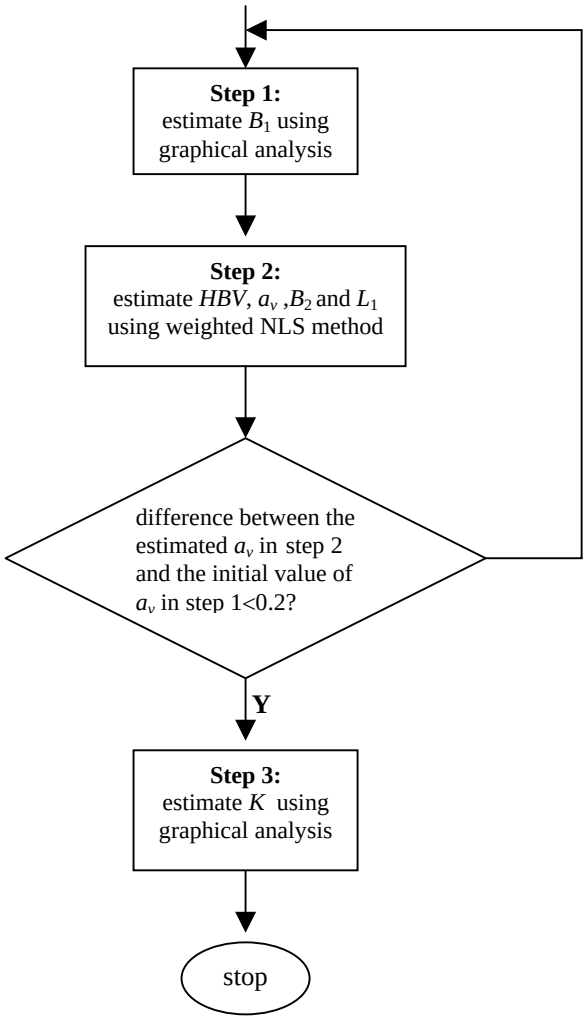

Figure 5- 2: The flow chart of the GNLS estimation procedure.

the first two steps would not cease until the difference between the estimated a_v in step 2 and the initial value of a_v utilized in step 1 is less than 0.2. In the successive first step estimation, the initial value of a_v would be set to the latest estimated a_v. For non-tumor cases, the iteration generally would not be repeated; for tumor cases, one more iteration is generally needed. In the third step, parameter K would be estimated by the graphical Gjedde-Patlak analysis with the

most updated a_v value to calculate the dual-input function. By using GNLS method, estimates of *HBV*, a_v and *K* (*LHMRAct*) could be obtained directly and the model rate constant parameters $K_1 - k_3$ could be calculated by

$$\begin{aligned} K_1 &= K + B_2 \\ k_2 &= \frac{B_2 L_1}{K + B_2} \\ k_3 &= \frac{K L_1}{K + B_2} \end{aligned} \tag{5}$$

5.2.3 Graphed Dual-Input Generalized Linear Least Squares Algorithm

The first step of our proposed GDGLLS algorithm applied to the dual-input ^{11}C-acetate liver cellular model is the same as the first step GNLS estimation. The model expressed by the second-order differential equation is

$$\frac{d^2 c_T(t)}{dt^2} = HBV \times \frac{d^2 c_b(t)}{dt^2} + \left[K_1 + (k_2 + k_3) HBV\right] \times \frac{dc_b(t)}{dt} + K_1 k_3 \times c_b(t) - (k_2 + k_3) \times \frac{dc_T(t)}{dt} \tag{6}$$

Substitute $c_b(t)$ in the first term of equation (6) with the dual-input function equation in section 3.2.3 and assume the initial conditions were all zeros, we obtain

$$c_T(t) = P_0 \times c_a(t) + P_3(c_v(t) - c_a(t)) + P_1 \int_0^t c_b(\tau) d\tau + KP_2 \int_0^t \int_0^t c_b(\tau) d\tau^2 - P_2 \int_0^t c_T(\tau) d\tau \tag{7}$$

where

$$P_0 = HBV$$
$$P_1 = K_1 + (k_2 + k_3)HBV$$
$$P_2 = k_2 + k_3$$
$$P_3 = HBV \times a_v$$
$$K = \frac{K_1 k_3}{k_2 + k_3}$$

Discretize equation (7) at the midtimes of sampling $t_i = (t'_i + t'_{i-1})/2$ (i = 1, 2, … , 25), the linear equation in matrix form is

$$y = X\theta + \xi \tag{8}$$

where $y = [c_T(t_1), c_T(t_2), \dots, c_T(t_{25})]^T$ are the total tracer concentration in tissue, $\theta = [P_0, P_1, P_2, P_3]^T$ are the parameters to be estimated, $\xi = [\xi_1, \xi_2, \dots, \xi_{25}]^T$ are the equation noise, and X is the coefficient matrix. Assume $\hat{K} \to K, \hat{a}_v \to a_v$, then

$$X = \begin{bmatrix} c_a(t_1) & \int_0^{t_1} \hat{c}_b(\tau)d\tau & (\hat{K}\int_0^{t_1}\int_0^{\tau} \hat{c}_b(s)dsd\tau - \int_0^{t_1} c_T(\tau)d\tau) & (c_v(t_1) - c_a(t_1)) \\ c_a(t_2) & \int_0^{t_2} \hat{c}_b(\tau)d\tau & (\hat{K}\int_0^{t_2}\int_0^{\tau} \hat{c}_b(s)dsd\tau - \int_0^{t_2} c_T(\tau)d\tau) & (c_v(t_2) - c_a(t_2)) \\ \vdots & & & \\ c_a(t_{25}) & \int_0^{t_{25}} \hat{c}_b(\tau)d\tau & (\hat{K}\int_0^{t_{25}}\int_0^{\tau} \hat{c}_b(s)dsd\tau - \int_0^{t_{25}} c_T(\tau)d\tau) & (c_v(t_{25}) - c_a(t_{25})) \end{bmatrix}$$

where $\hat{K}$ is the parameter estimate provided by step 1, $\hat{a}_v$ is the initial guess of a_v and $\hat{c}_b(\tau)$ is calculated by the dual-input function equation with the initial guess of a_v. In the second step of GDGLLS, the parameters are estimated by

$$\hat{\theta}_{GDLLS} = \left(X^T X\right)^{-1} X^T y \tag{9}$$

where $\hat{\theta}_{GDLLS}$ represents the estimated θ in this GDLLS sense. With the estimate of the forward clearance K by step 1 and the estimates of $P_0 - P_3$ by equation (9), all the individual parameters $K_1 - k_3$, HBV and a_v could be obtained.

The estimation results in step 2 would be used as the initial values of step 3 that aims to refine the fitting results of step 2. If all the dual-input function terms were substituted by the dual-input function equation, the dual-input ^{11}C-acetate model could be described

$$\frac{d^2c_T(t)}{dt^2} = P_0 \times \frac{d^2c_a(t)}{dt^2} + P_0 a_v(\frac{d^2c_v(t)}{dt^2} - \frac{d^2c_a(t)}{dt^2}) + P_1 \times \frac{dc_a(t)}{dt} + P_1 a_v(\frac{dc_v(t)}{dt} - \frac{dc_a(t)}{dt}) + KP_2 \times c_a(t) + KP_2 a_v(c_v(t) - c_a(t)) - P_2 \times \frac{dc_T(t)}{dt} \quad (10)$$

where

$$P_0 = HBV$$
$$P_1 = K_1 + (k_2 + k_3)HBV$$
$$P_2 = k_2 + k_3$$
$$K = \frac{K_1 k_3}{k_2 + k_3}$$

To obtain the GDGLLS solution, assume $\hat{K} \to K$ and $\hat{P}_0 \to P_0, \hat{P}_1 \to P_1, \hat{P}_2 \to P_2$ in the second, fourth and sixth terms of equation (10) respectively, we have,

$$\frac{d^2c_T(t)}{dt^2} = P_0 \times \frac{d^2c_a(t)}{dt^2} + P_1 \times \frac{dc_a(t)}{dt} + \hat{K}P_2 \times c_a(t) + a_v(\hat{P}_0(\frac{d^2c_v(t)}{dt^2} - \frac{d^2c_a(t)}{dt^2}) + \hat{P}_1(\frac{dc_v(t)}{dt} - \frac{dc_a(t)}{dt}) + \hat{K}\hat{P}_2(c_v(t) - c_a(t))) - P_2 \times \frac{dc_T(t)}{dt} \quad (11)$$

where $\hat{K}$ is the parameter estimate by step 1 and $\hat{P}_0, \hat{P}_1, \hat{P}_2$ represent the most updated estimates of P_0, P_1, P_2 respectively. Take the Laplace transform of the above equation with the assumption that the initial conditions were all zeros, whiten the correlated equation errors with an autoregressive filter $s(s + \hat{P}_2)$ [74], and then take the inverse Laplace transform, the time domain output function is

$$c_T(t) - \hat{P}_2\psi_1 \otimes c_T(t) = P_0\left(c_a(t) - \hat{P}_2\psi_1 \otimes c_a(t)\right) + P_1\psi_1 \otimes c_a(t) + P_2\left(\hat{K}\psi_2 \otimes c_a(t) - \psi_1 \otimes c_T(t)\right) + a_v\left(\hat{P}_0(c_v(t) - c_a(t)) + (\hat{P}_1 - \hat{P}_0\hat{P}_2)\psi_1 \otimes (c_v(t) - c_a(t)) + \hat{K}\hat{P}_2\psi_2 \otimes (c_v(t) - c_a(t))\right) \quad (12)$$

where

$$\psi_1 = e^{-\hat{P}_2 t}$$

$$\psi_2 = \frac{1}{\hat{P}_2}(1 - e^{-\hat{P}_2 t})$$

Discretize equation (12) at the midtimes of sampling $t_i = (t'_i + t'_{i-1})/2$ (i = 1, 2, … 25), the equation could be obtained as

$$r = Z\theta + \zeta \quad (13)$$

where r is the filtered output at the midtimes of sampling, θ=[P_0, P_1, P_2, a_v]^T are the parameters to be estimated, ζ=[ζ_1, ζ_2, … , ζ_{25}]^T are the filtered equation errors, and Z is the coefficient matrix. In the third step of GDGLLS, the parameters would be estimated by

$$\hat{\theta}_{GDGLLS} = \left(Z^T Z\right)^{-1} Z^T r \quad (14)$$

where $\hat{\theta}_{GDGLLS}$ represents the estimated θ in this GDGLLS sense. The weight used in equation (14) was calculated by equation (4) as well. Equation (14) would not cease until termination criteria are satisfied. In this study, the termination criterion was that either maximum iteration of 10 was reached or the Euclidean norm of difference of parameter estimates between two successive iterations was less than 0.0001. The flow chart of the GDGLLS algorithm was illustrated in Figure 5-3. All the individual parameters could be estimated by GDGLLS method in the first three steps. In the fourth step, parameter K would be estimated by the graphical Gjedde-Patlak analysis with the most updated a_v value to calculate the dual-input function.

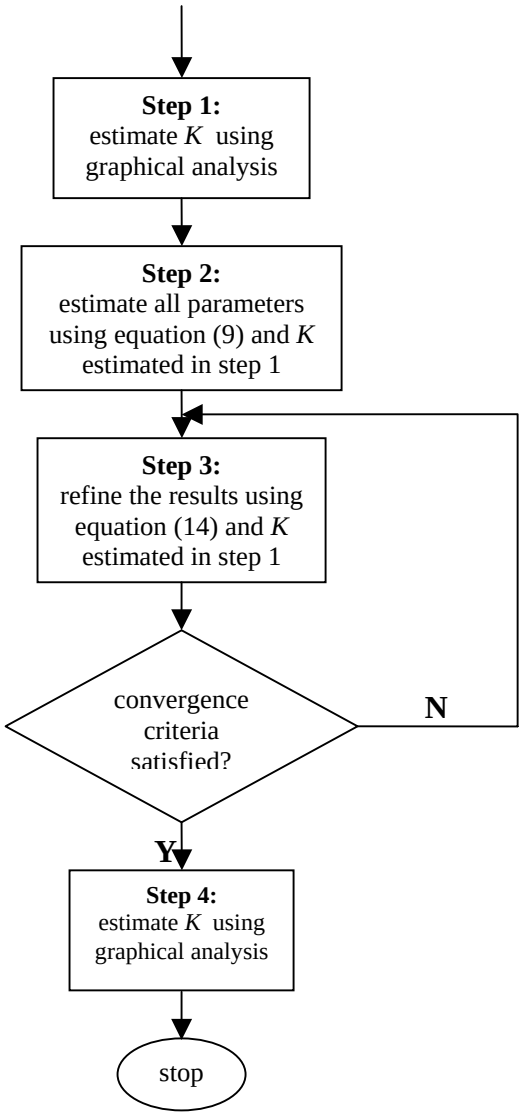

Figure 5- 3: The flow chart of the GDGLLS algorithm.

5.2.4 Clinical Study

The dynamic PET images were recorded with an ECAT EXACT 47 PET scanner (model 921; CTI/Siemens, Inc., Knoxville, TN), which simultaneously acquired 47 contiguous transverse slices (septa extended). Each patient was

positioned to allow image acquisition of the liver dome and apical half of the left ventricle to the inferior part of liver. Serial images were obtained immediately after the bolus IV injection of ^{11}C-acetate. The image acquisition sequences were as follows: ten frames of 4 sec each, eight frames of 10 sec each, two frames of 30 sec each, followed by three frames of 60 sec each and two frames of 120 sec each, a total of 25 frames for 10 min. Reconstruction and attenuation correction was performed with the standardized ordered-subsets expectation maximization technique. Reconstructed transaxial spatial resolution was about 4.4 mm.

Six patients with liver masses were studied, all were hepatitis B carriers, including two with HCC. Regions of interests (ROIs) were defined using single transverse slice of the full set of dynamic images. For each patient, one non-tumor liver tissue ROI was extracted. Two HCC regions were extracted from the two patients suffered from HCC. The TAC of PV was evaluated by direct activity-time measurement. To reduce the radioactivity spillover effect from the adjacent tissue, the TAC of HA was approximated by evaluating the TAC of the abdominal aorta adjacent to the liver [15] [16] and the last five measurements of the TAC of PV were replaced by the corresponding HA data as in Chapters 2 and 3.

5.2.5 Simulation Study

All the parameter estimation methods including NLS, GNLS and GDGLLS were tested by computer simulated data. Two simulated datasets with the same image-derived dual-input extracted from clinical data were generated in this

study, including one representing HCC. The scanning intervals were the same as those of clinical data acquisition. A pseudorandom number generator was used to generate the Gaussian noise added to the calculated TAC and the variance structure could be described as

$$\sigma^2(t_i) = \frac{\alpha \times c_T(t_i)}{\Delta t_i} \qquad i = 1,2,...,25 \tag{15}$$

where $c_T(t_i)$ is the calculated TAC, Δt_i is the scanning interval, $\sigma^2(t_i)$ is the variance of $c_T(t_i)$, and α is the proportional constant representing the noise level. In this study, the noise levels are set to 0.1, 0.5, 1 and 2.

5.2.6 Statistical Criteria

The correlation analysis was conducted for the estimated K_1 - k_3, a_v, *HBV* and *K* provided by NLS and GNLS methods for the clinical datasets. In addition, the Akaike Information Criteria (AIC) [52] and Schwarz Criteria (SC) [53] were utilized to test the "goodness of fit". It was assumed that the data variances were known up to a proportionality constant, therefore, the AIC and SC are given by

$$AIC = N \ln(WRSS) + 2N_P \tag{16}$$

$$SC = N \ln(WRSS) + N_P \ln N \tag{17}$$

where N_P is the number of parameters, and N is the number of data points, and *WRSS* is the weighted residual sum of squares. The reliability of parameter estimation was accessed by the coefficient of variation (*CV*), which is the computed measurements of the estimates' variability and formulated as

$$CV_P = \frac{SD_P}{P} \times 100\% \tag{18}$$

where P is the parameter estimate and SD_P is the standard deviation (*SD*) of P. In NLS and GNLS fitting procedure, *SDs* were estimated as the square roots of the diagonal elements of the covariance matrix and the covariance matrix was estimated based on sensitivity functions. For the simulation study, the accuracy of the estimated parameters was evaluated by *bias*, which is calculated by

$$Bias = \left| \frac{P^{true} - \bar{P}}{P^{true}} \right| \times 100\% \tag{19}$$

where P^{true} is the true value of the parameter, and $\bar{P}$ is the mean value calculated from 200 simulation runs.

5.3 Results and Discussion

Figure 5-4 shows one slice of dynamic ^{11}C-acetate-PET images of HCC. The HCC region demonstrates significantly increased ^{11}C-acetate uptake in the last several frames. The quantitative studies of this molecular imaging were performed by modeling the ^{11}C-acetate kinetics in liver cells and estimating the corresponding characteristic parameters.

To evaluate the performance of GNLS, comparison between the estimation by NLS and GNLS for clinical datasets was conducted. The parameter estimates of K_1 - k_3, *HBV*, a_v and K (*LHMRAct*) by these two methods were listed in Table 5-1. As seen in Table 5-1, the estimation results predicted by the two methods are comparable with each other. The correlation coefficients by the correlation

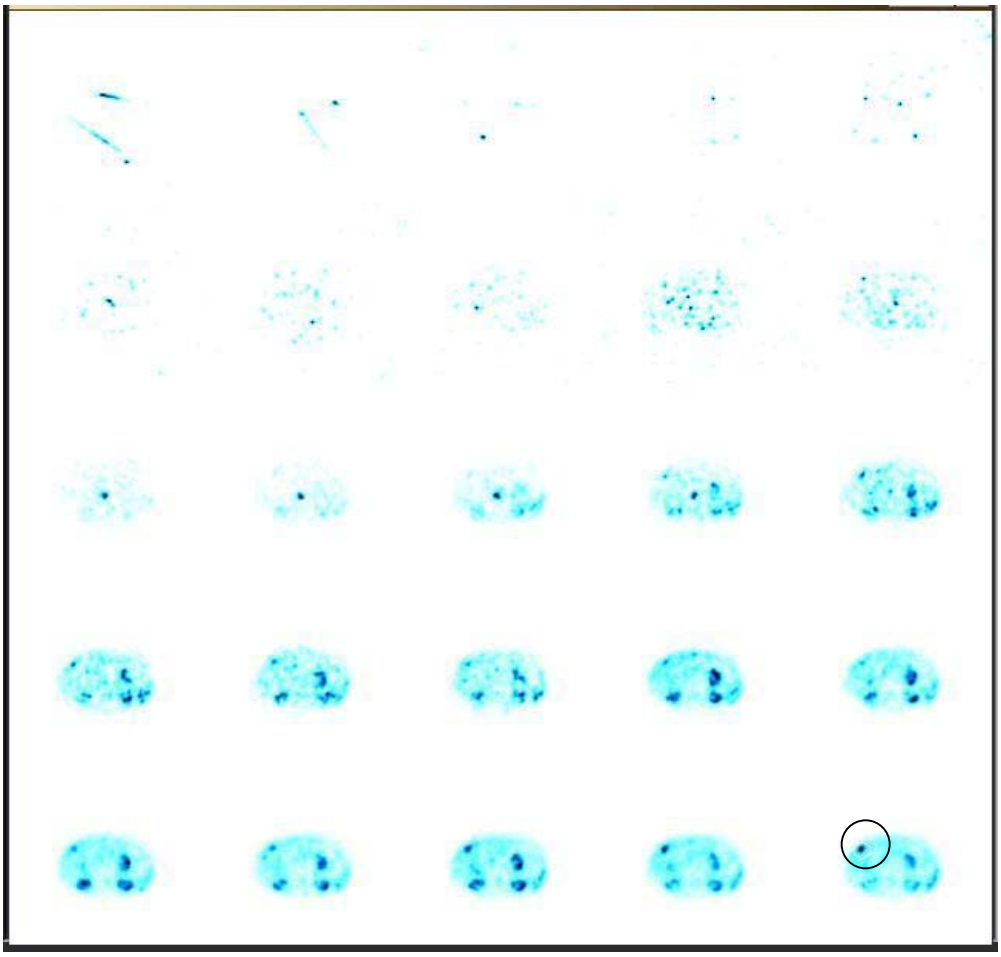

Figure 5- 4: One slice of dynamic ^{11}C-acetate-PET images of HCC. The images were displayed row by row, from left to right. The enclosed area indicates HCC.

analysis of the two sets of K_1, k_2, k_3, *HBV*, a_v and K (*LHMRAct*) for each defined ROI are 0.9872, 0.9563, 0.9868, 0.9920, 0.9987 and 0.9847 respectively. The two sets of estimated a_v in Table 5-1 were approximately the same. For the six non-tumor liver tissue regions, the estimated a_v expressed as mean value ± *SD* are 0.8495 ± 0.0752 and 0.8361 ± 0.0790 by GNLS and NLS methods respectively. The estimated K by GNLS and NLS methods are 0.1602 ± 0.0225 and 0.1437 ± 0.0224 respectively for datasets 1 to 6. The correlation of these estimated parameters by the two methods was plotted in Figure 5-5. As shown in

Table 5- 1: The parameter estimates of K_1, k_2, k_3, HBV, a_v and K by NLS and GNLS methods for the clinical datasets.

Datasets	NLS						GNLS					
Number	K_1	k_2	k_3	HBV	a_v	K	K_1	k_2	k_3	HBV	a_v	K
1	0.7815	0.3822	0.0728	0.0880	0.9004	0.1250	0.8307	0.4006	0.0987	0.0817	0.9085	0.1642
2	0.8073	0.3355	0.0602	0.0548	0.8634	0.1228	0.8790	0.3443	0.0768	0.0539	0.8899	0.1603
3	0.5300	0.3694	0.1421	0.2908	0.6972	0.1472	0.5156	0.3573	0.1446	0.3077	0.7192	0.1485
4	0.6687	0.4849	0.1782	0.4680	0.8994	0.1797	0.6749	0.4739	0.1569	0.4568	0.8978	0.1679
5	0.9794	0.2435	0.0371	0.1358	0.7903	0.1296	0.9896	0.2504	0.0366	0.1567	0.7980	0.1261
6	0.8269	0.4194	0.0990	0.0480	0.8657	0.1580	0.8660	0.4316	0.1249	0.0715	0.8837	0.1944
7	1.3601	0.4113	0.1176	0.1573	0.3330	0.3025	1.3055	0.3730	0.0987	0.2006	0.3433	0.2731
8	0.9935	0.3398	0.3852	0.1473	0.5684	0.5278	0.9635	0.3083	0.3547	0.1528	0.5661	0.5154

Note: Datasets 1 to 6 represent non-tumor liver tissue ROIs extracted from six patients' data. Datasets 7 and 8 represent HCC ROIs extracted from patients 4 and 6.

Figure 5-5, all the estimated parameters by the two approaches correlated closely with each other.

The *CVs* of the estimated K_1, k_2, k_3, HBV and a_v by NLS fitting and the estimated K, B_2, L_1, HBV and a_v by GNLS fitting for the clinical datasets were summarized in Table 5-2. As seen in Table 5-2, the results of GNLS have conclusively demonstrated that the estimation reliability of K, B_2, and L_1 is satisfactory since most *CVs* are less than 20%. The average *CVs* of K, B_2, and L_1 are much less than the mean *CVs* of K_1, k_2 and k_3 by NLS in Table 5-2. With the estimated K, B_2, and L_1 by GNLS, the model rate constant parameters K_1 - k_3 could be calculated by equation (5). Therefore, K_1, k_2 and k_3 could be much more reliably estimated by the proposed GNLS method. It is worth noting in Table 5-2 that the estimation of a_v by GNLS is very reliable since most *CVs* are less than 20% and half of them are less than 10%. Majority *CVs* of the estimated a_v by

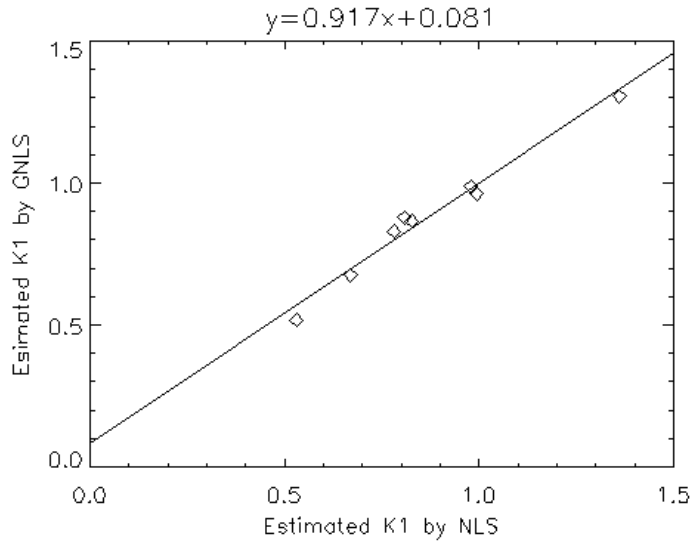
y=0.917x+0.081
Esimated K1 by GNLS
Estimated K1 by NLS
0.0
0.5
1.0
1.5

(a)

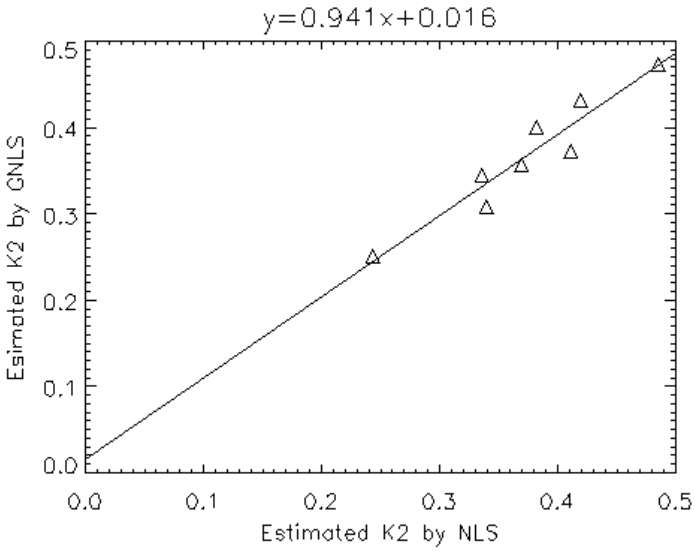
y=0.941x+0.016
Esimated K2 by GNLS
Estimated K2 by NLS
0.0
0.1
0.2
0.3
0.4
0.5

(b)

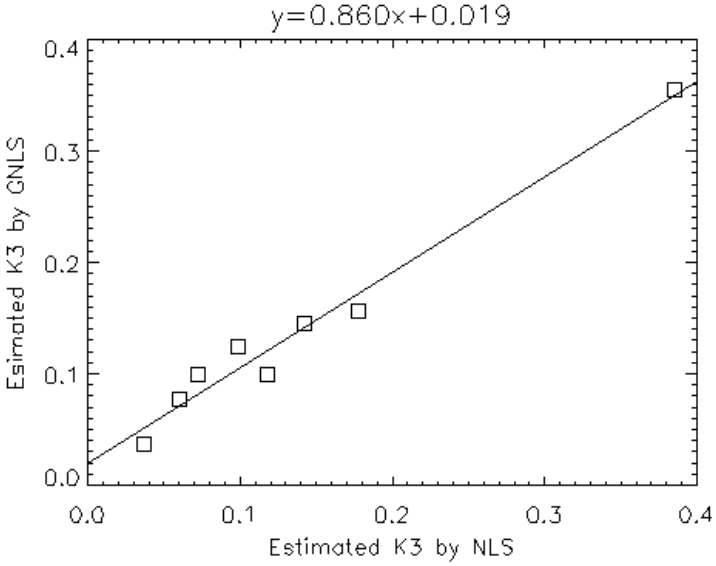
y=0.860x+0.019
Esimated K3 by GNLS
Estimated K3 by NLS
0.0
0.1
0.2
0.3
0.4

(c)

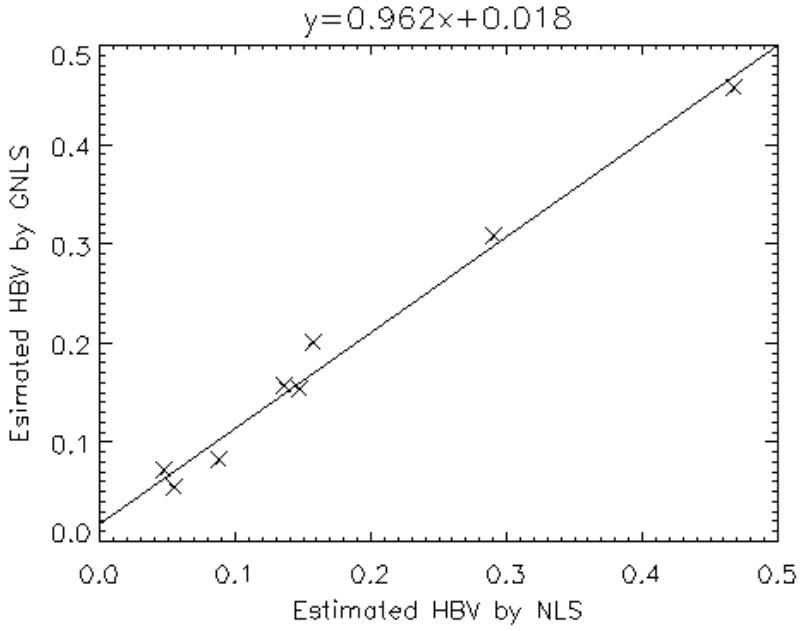
y=0.962x+0.018
Esimated HBV by GNLS
Estimated HBV by NLS
0.0
0.1
0.2
0.3
0.4
0.5

(d)

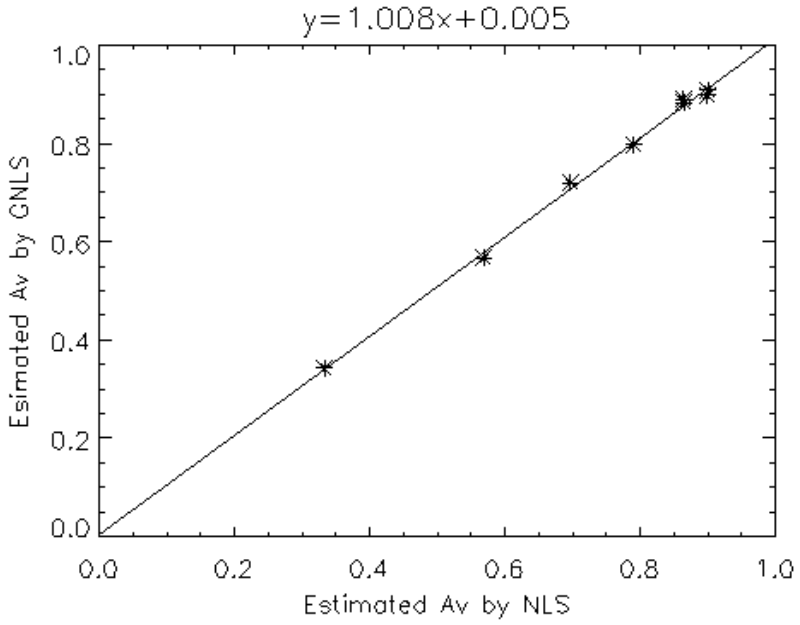
y=1.008x+0.005
Esimated Av by GNLS
Estimated Av by NLS
0.0
0.2
0.4
0.6
0.8
1.0

(e)

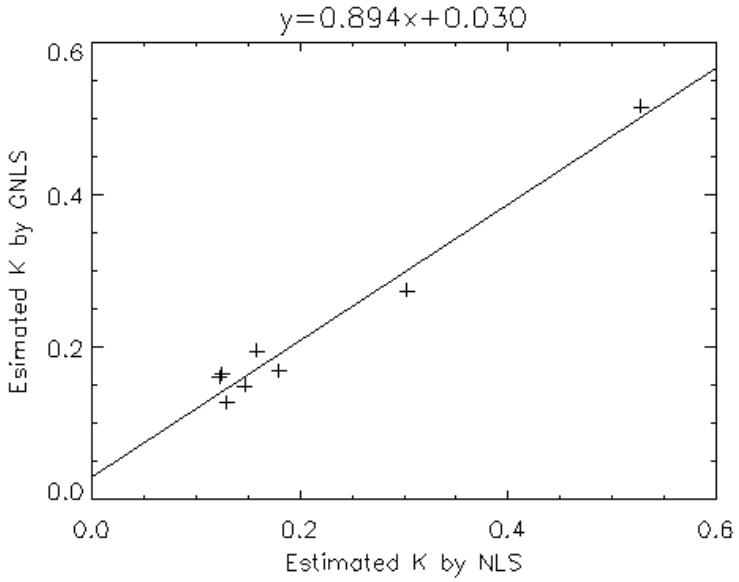

(f)

Figure 5- 5: Correlation of the estimated (a) K_1, (b) k_2, (c) k_3, (d) *HBV*, (e) a_v and (f) K for the eight clinical ROIs by using GNLS and NLS methods.

Table 5- 2: Comparison of the *CVs* of the estimated K_1, k_2, k_3, *HBV* and a_v by NLS and the estimated K, B_2, L_1, *HBV* and a_v by GNLS for the clinical datasets.

Datasets	NLS					GNLS				
Number	K_1	k_2	k_3	*HBV*	a_v	K	B_2	L_1	*HBV*	a_v
1	18.40	30.45	35.64	52.80	7.70	9.70	24.79	22.16	59.45	7.86
2	8.01	15.65	29.84	53.97	8.46	25.01	8.54	8.69	59.19	7.56
3	9.74	21.46	22.40	18.45	10.45	9.20	10.27	9.18	15.33	8.94
4	15.87	25.88	14.66	16.65	5.31	8.39	13.73	10.02	14.23	4.99
5	9.80	18.86	71.47	60.41	13.39	38.95	10.17	12.38	51.14	11.89
6	22.44	36.03	33.22	172.6	12.74	10.06	23.47	19.99	141.7	11.44
7	15.71	24.53	17.08	52.18	74.25	12.17	15.96	13.88	50.16	73.23
8	43.88	63.92	29.20	77.70	51.17	2.82	31.96	18.79	39.51	21.12
Average	17.98	29.60	31.69	63.10	22.93	14.54	17.36	14.39	53.84	18.38

GNLS are less than those by NLS, and the estimation of a_v of region 8 is considerably more reliable. As illustrated in Table 5-2, the estimation of *HBV* by GNLS is generally more reliable than that by NLS especially for region 8. All these findings suggest that GNLS method could provide more reliable parameter estimation for ^{11}C-acetate dual-input liver model.

As shown in Table 5-3, when compared with NLS method, all SCs of clinical datasets by GNLS except those of regions 1 and 7 are smaller, which may indicate that GNLS could provide better fit. The two sets of AICs are comparable with each other.

It is widely acknowledged that the initial guess and computational burden issues limit the application of NLS algorithm in the clinical environment, though its fitting results are generally considered as the gold standard. During the GNLS fitting procedure, owing to the reduced number of parameters to be estimated by the recursive NLS procedure, the computational burden is reduced. Since one of the model macroparameters B_1 are predetermined and considered as a *prior*, the fitting results of the second step NLS regression are less affected by the initial guess.

Computer simulation was utilized to examine both GNLS and GDGLLS methods as well. The estimation results of the mean values, *biases*, and *CVs* of K_1 - k_3, *HBV*, a_v and K (*LHMRAct*) calculated from 200 simulation runs by NLS, GNLS and GDGLLS were presented in Table 5-4. When compared with NLS method, the rate constant parameters K_1 - k_3 could be considerably more reliably

Table 5- 3: The AICs and SCs by NLS and GNLS algorithms for the clinical datasets.

Datasets Number	NLS		GNLS	
	AIC	SC	AIC	SC
1	176.51	182.61	178.74	183.61
2	165.97	172.07	166.68	171.56
3	179.84	185.94	178.58	183.45
4	163.61	169.71	163.82	168.70
5	177.61	183.71	177.12	182.00
6	176.32	182.41	176.46	181.34
7	192.54	198.63	194.04	198.92
8	169.44	175.54	167.60	172.47

estimated by both GNLS and GDGLLS especially when the noise level is high. Nevertheless, NLS could provide more accurate estimates of K_1 - k_3. As shown in Table 5-4, the estimation of a_v and *HBV* by the two proposed methods is moderately more reliable than that by NLS. The accuracy of the estimated a_v and *HBV* using the two presented approaches is in general comparable with that of NLS. The estimation of *K* in Table 5-4 by both GNLS and GDGLLS is much more reliable for all the cases when compared to the results of NLS, especially when the noise level is 2. The estimation accuracy of Parameter *K* is satisfactory since all *biases* are around 1% for dataset 1 and less than 1% for dataset 2. When the noise level is 2, both methods could achieve better fitting accuracy for this HCC indicator (Parameter *K*). It could be concluded from Table 5-4 that the estimation accuracy of all the parameters by the two presented techniques is generally not sensitive to the noise level: higher noise level would not definitely mean worse fitting results, which may be extremely useful in clinical settings whose noise level is generally high. Besides, by using GDGLLS algorithm all the individual model parameters could be expressed analytically in terms of the PET

Table 5- 4: Estimation results of K_1 - k_3, *HBV*, a_v and K from two sets of simulation, in which the second dataset represents HCC. The true value of the two datasets is K_1=0.65, k_2 =0.40, k_3=0.15, *HBV*=0.30, a_v=0.75 and K_1=1.35, k_2 =0.35, k_3=0.13, *HBV*=0.30, a_v=0.40 respectively. The estimated parameters in this table represent their mean values. The mean values, *biases* (percentage value), and *CVs* (percentage value) were calculated from 200 simulation runs.

Method	K_1	$bias_1$	CV_1	k_2	$bias_2$	CV_2	k_3	$bias_3$	CV_3	HBV	$bias_H$	CV_H	a_v	$bias_a$	CV_a	K	$bias_K$	CV_K
	Noise level α=0.1																	
NLS	0.6504	0.06	0.75	0.4007	0.17	1.45	0.1502	0.17	1.19	0.2998	0.07	1.77	0.7498	0.02	0.96	0.1774	0.06	0.48
GNLS	0.6587	1.34	0.45	0.4157	3.93	0.62	0.1559	3.94	0.72	0.2952	1.59	1.59	0.7472	0.37	0.94	0.1796	1.32	0.30
GDG	0.6505	0.07	0.57	0.4090	2.24	0.90	0.1568	4.55	0.72	0.3040	1.34	1.67	0.7508	0.11	1.04	0.1796	1.31	0.31
	Noise level α=0.5																	
NLS	0.6516	0.24	3.90	0.4030	0.75	7.51	0.1510	0.63	5.99	0.2992	0.28	8.93	0.7479	0.28	4.92	0.1776	0.16	2.39
GNLS	0.6577	1.19	2.32	0.4153	3.82	3.21	0.1562	4.14	3.58	0.2953	1.56	8.55	0.7453	0.62	4.30	0.1797	1.37	1.53
GDG	0.6504	0.05	2.98	0.4083	2.07	4.61	0.1562	4.16	3.59	0.3018	0.61	8.90	0.7441	0.79	4.58	0.1791	1.05	1.56
	Noise level α=1																	
NLS	0.6526	0.40	8.21	0.4054	1.36	15.80	0.1509	0.58	12.22	0.2973	0.89	18.14	0.7410	1.21	10.62	0.1771	0.13	4.97
GNLS	0.6543	0.66	5.02	0.4125	3.12	7.08	0.1566	4.39	7.26	0.2954	1.53	16.20	0.7386	1.52	10.08	0.1797	1.38	3.06
GDG	0.6448	0.80	6.11	0.4029	0.73	9.57	0.1557	3.82	7.19	0.2978	0.72	18.12	0.7268	3.09	12.00	0.1785	0.70	3.15
	Noise level α=2																	
NLS	0.6527	0.42	17.89	0.4100	2.50	33.56	0.1492	0.54	25.41	0.2932	2.27	36.45	0.7088	5.50	28.83	0.1740	1.87	11.31
GNLS	0.6421	1.22	10.25	0.3993	0.18	14.87	0.1562	4.14	14.99	0.2880	4.00	35.28	0.7003	6.63	26.12	0.1794	1.18	6.24
GDG	0.6185	4.85	13.01	0.3822	4.44	22.28	0.1585	5.69	16.34	0.2877	4.09	36.00	0.6826	8.98	30.26	0.1785	0.70	5.81
Method	K_1	$bias_1$	CV_1	k_2	$bias_2$	CV_2	k_3	$bias_3$	CV_3	HBV	$bias_H$	CV_H	a_v	$bias_a$	CV_a	K	$bias_K$	CV_K
	Noise level α=0.1																	
NLS	1.3504	0.03	0.89	0.3503	0.09	1.58	0.1301	0.10	1.29	0.3000	0.01	2.39	0.4000	0.00	3.56	0.3658	0.04	0.55
GNLS	1.3556	0.41	0.73	0.3544	1.25	1.01	0.1320	1.56	0.68	0.2997	0.11	2.04	0.4016	0.40	3.01	0.3680	0.64	0.32
GDG	1.3770	2.00	0.64	0.3733	6.65	0.85	0.1421	9.31	0.74	0.3111	3.71	2.01	0.4144	3.60	3.34	0.3684	0.77	0.32
	Noise level α=0.5																	
NLS	1.3507	0.05	4.54	0.3515	0.42	8.04	0.1305	0.39	6.49	0.3000	0.00	11.70	0.3960	1.01	18.39	0.3657	0.03	2.80
GNLS	1.3531	0.23	3.73	0.3538	1.08	5.14	0.1321	1.60	3.44	0.3000	0.01	10.46	0.3972	0.70	16.05	0.3677	0.57	1.63
GDG	1.3724	1.66	3.24	0.3720	6.29	4.29	0.1423	9.46	3.78	0.3102	3.39	10.61	0.4146	3.65	16.86	0.3681	0.68	1.61
	Noise level α=1																	
NLS	1.3501	0.01	9.31	0.3533	0.95	16.49	0.1308	0.58	13.19	0.3009	0.31	23.01	0.3842	3.96	39.52	0.3645	0.30	5.82
GNLS	1.3471	0.21	7.70	0.3531	0.88	10.82	0.1326	2.00	7.10	0.3011	0.39	20.60	0.3844	3.90	36.20	0.3673	0.46	3.28
GDG	1.3630	0.96	6.45	0.3695	5.57	8.56	0.1429	9.93	7.88	0.3125	4.17	21.51	0.4007	0.17	35.73	0.3674	0.50	3.22
	Noise level α=2																	
NLS	1.3509	0.07	17.82	0.3596	2.76	31.15	0.1313	0.98	26.34	0.3071	2.36	44.60	0.3475	13.12	91.11	0.3588	1.86	12.69
GNLS	1.3283	1.61	15.27	0.3502	0.06	21.41	0.1344	3.38	14.90	0.3087	2.91	40.53	0.3477	13.08	86.68	0.3658	0.05	6.65
GDG	1.3309	1.41	13.02	0.3619	3.39	17.30	0.1467	12.83	19.20	0.3203	6.76	40.63	0.3497	12.57	86.67	0.3658	0.06	6.46

Notes: “GDG” are the abbreviations of “GDGLLS”.

measurements. The average number of iterations needed for step 3 of GDGLLS in the simulation study is generally less than 4 (shown in Table 5-5), therefore, the fitting procedure is significantly faster than NLS method. As shown in Table

Table 5- 5: The average number of iterations needed by GDGLLS in simulation study.

Datasets Number	Noise level			
	0.1	0.5	1	2
1	2.99	2.77	3.23	4.12
2	3.98	3.58	3.48	3.91

5-5, when the noise level increases, the number of iterations needed would not increase which is very valuable for the generation of parametric images.

5.4 Conclusion

Two novel parameter estimation techniques for ^{11}C-acetate liver kinetic model with dual hepatic blood supply using dynamic PET images were presented in this chapter. When compared with NLS approach, more reliable parameter estimates and better fitting quality in terms of SC could be provided by GNLS method for clinical study. Due to the reduced number of parameters to be estimated by NLS regression, the computational burden of GNLS is reduced when compared with the standard NLS method and the fitting results are less affected by the initial guess because the predetermined B_1 is considered as a *prior*. GDGLLS algorithm could generally identify all the parameters more reliably including the parameter in the dual-input function and the fitting procedure is drastically faster than NLS method. Compared with NLS fitting, both presented algorithms could achieve a comparable estimation accuracy of the

two HCC indicators. When the noise level is high, both methods could even achieve better fitting accuracy of Parameter *K*. Due to the robustness and computational efficiency, the two presented algorithms might be promising for providing the functional physiological parametric images of the two HCC markers. Therefore, the two estimation algorithms could provide better ways in the noisy clinical environment for the early detection of HCC and are generally applicable for other dual-input biomedical systems.

Chapter 6 Use of Modeling the Dual Hepatic Blood Supply for Liver Studies with Dynamic ^{11}C-Acetate PET

6.1 Introduction

As pointed in Chapter 5, the use of positron emission tomography (PET) for the studying of liver disease has been mostly in the detection of liver tumors [6], [25], [84], [85], [89]. The investigation of tumor kinetics by ^{18}F-fluorodeoxyglucose (FDG) PET imaging has suggested that the detection of liver tumors, especially hepatocellular carcinoma (HCC), is hampered due to the abundance of the enzyme glucose-6-phosphatase in HCC leading to leakage of FDG metabolites back to the circulation [25], [90], [91]. The evaluation of HCC could be aided by dynamic FDG PET quantitative studies [25], [90]. Besides, recent introduction of ^{11}C-acetate in imaging HCC and other liver masses by Ho *et al.* [6], [7] and the successive quantification studies of dynamic ^{11}C-acetate PET images using tracer kinetic modeling techniques in Chapters 2 and 3 could significantly improve the *in vivo* assessment of HCC.

As aforementioned, for the quantification studies of dynamic ^{11}C-acetate/FDG PET using tracer kinetic modeling techniques, both measurements of tracer concentration in the hepatic artery (HA) and portal vein (PV), the dual hepatic blood supply, should be considered [4], [55], [83], [90]. Directly measuring them by the widely adopted blood sampling or cannulation procedure is invasive, as it is invasive to the subject and exposes personnel to the risks associated with the handling of patient blood and radiation dose [68]. In addition, measurement of blood flow in the human liver is difficult as gaining proper access to the organ is virtually impractical and it is highly invasive in clinical settings to measure the portal venous blood flow by direct catheterization and sampling.

Many efforts have been paid to reduce the invasiveness of the blood sampling procedure. PET-acquired input function has been validated by many researchers for various clinical quantitative studies [15], [16], [18], [19], [92]-[94], where manual placement of the location of blood vessels is always required. However, the tracer arriving at the PV is delayed and dispersed, and furthermore, the radioactivity spillover from the surrounding tissue to the PV is significant, making it difficult to differentiate the individual PV region from the liver tissue [55]. Besides, it is possible that the PV region is inaccessible on some PET scans. The requirement of user drawn region-of-interest (ROI) makes this image-derived method operator dependent and lack of reproducibility.

To avoid the spillover correction problem and improve the reliability and reproducibility, alternative methods of extracting the time-activity curves (TACs)

of blood vessels were developed. Factor analysis of dynamic structures (FADS) algorithm based on principal component analysis (PCA) with positivity constraints was found sufficient to extract the blood factor from the composite dynamic images without blood sampling or ROI drawing [95]. However, as aforementioned the TACs of PV and normal liver tissue show no much difference and the decomposed factors themselves may not represent the true physiological factors, which makes the portal venous blood factor is indiscernible. In addition, due to the small size of HA and PV, the accuracy of blood TAC extraction would be affected [96]. To improve the accuracy, a spatial independent component analysis (ICA) was proposed [96]. However, the spatial distribution of vessels is desired on PET images by using this method, which is impossible for PV as it is difficult to separate it from the surrounding tissue and it is even inaccessible on some PET scans. Another negative aspect of both FADS and spatial ICA is the computation burden, which is impractical in clinical settings.

Some researchers has proposed an eigenvector-based algorithm for the blind deconvolution of input signals [97], however, it is not applicable for the dual-input hepatic system since the input function is ROI or even pixel different [83].

Another type of solution to acquire the input function noninvasively is modeling approach [38], [39], [44]. Feng *et al.* proposed a blood TAC model to describe the tracer kinetics in blood vessels, however, it is not adaptable for the dual-input liver system, since the model could only estimate the TAC of HA. Little attention has been paid to modeling the tracer kinetics in the PV. The

portal venous input is generally predicted by convolution of the arterial input with a notional system function with five parameters [90], [98]. However, in addition to the five parameters of ^{11}C-acetate dual-input liver model as stated in Chapter 3, ten parameters need to be estimated simultaneously, which would be an extremely difficult task for convergence.

With regard to all the negative aspects of the aforementioned techniques when applied to the quantification of dynamic ^{11}C-acetate PET in liver, in this chapter we investigated whether the quantification could be accessed reliably and accurately by using a simple model accounting for the tracer kinetics in the PV. Therefore, the tedious or even unsolvable task of measuring the PV curve could be eliminated, which would be very meaningful for the clinical evaluation of HCC *in vivo*.

6.2 Materials and Methods

6.2.1 PET Examination

Dynamic ^{11}C-acetate PET studies were performed on five human subjects, including two with HCC, lying in the position that allows image acquisition of the liver dome and apical half of the left ventricle to the inferior part of liver. Before the emission scan, transmission scan was performed with a total of 10 min acquisition time. Immediately after the bolus IV injection of ^{11}C-acetate, dynamic PET images were recorded with an ECAT EXACT 47 PET scanner

(model 921; CTI/Siemens, Inc., Knoxville, TN), which simultaneously acquired 47 contiguous transverse slices (septa extended) over a period of 10 min by measuring ten 4 sec frames, eight 10 sec frames, two 30 sec frames, followed by three 60 sec frames and two 120 sec frames, a total of 25 frames. Reconstruction and attenuation correction was performed with the standardized ordered-subsets expectation maximization technique.

6.2.2 Analysis of ^{11}C-Acetate PET Images

For quantitative analysis, ROIs were defined on single transverse slice on a frame-by-frame basis. The TAC of each ROI was created by averaging the activity in each region. For each patient, two ROIs were defined, thus, a total of eight nontumor liver tissue ROIs and two HCC ROIs (from two HCC patients) were extracted from the five patients for this study. To be relatively free of the radioactivity spillover from the liver tissue, the TAC of HA was approximated by defining ROI over the abdominal aorta adjacent to the liver.

6.2.3 Modeling the Dual Hepatic Blood Supply

As aforementioned in contrast to other organs or tissues, which are supplied only by arterial blood, the liver has a dual source of blood supply: receiving oxygenated blood from the common left and right HAs and nutrient-rich blood from the gastrointestinal tract via the PV. When the tracer concentration of the

arterial blood entering the gastrointestinal tract was approximated to that of HA, according to Fick principle [99], we obtain

$$\frac{dQ_g(t)}{dt} = F(c_a(t) - c_v(t)) \tag{1}$$

where $Q_g(t)$ is the quantity of ^{11}C-acetate in gastrointestinal tract, $c_a(t)$ and $c_v(t)$ are the tracer concentration in HA and PV respectively, and it is assumed that the arterial flow is equal to venous flow, denoted by F (ml/min/ml). The assumption was also made that the blood in the gastrointestinal tissue forms only a small percentage of the total tissue volume. If W (g) denotes the weight of the tissue in gastrointestinal tract, the concentration of ^{11}C-acetate in the gastrointestinal tissue $c_g(t)$ could be given by the equation

$$\frac{dc_g(t)}{dt} = \frac{1}{W}\frac{dQ_g(t)}{dt} = \frac{F}{W}(c_a(t) - c_v(t)), \tag{2}$$

and we also assume

$$c_g(t) = \lambda c_v(t) \tag{3}$$

where λ is the partition coefficient describing ratio of the solubility of ^{11}C-acetate in gastrointestinal tissue and blood [99]. Substituting $c_g(t)$ is equation (2) with equation (3), we have

$$\frac{\lambda dc_v(t)}{dt} = \frac{F}{W}(c_a(t) - c_v(t)) \tag{4}$$

then, the differentiation of $c_v(t)$ (the tracer concentration in PV) could be expressed as

$$\frac{dc_v(t)}{dt} = \frac{F}{\lambda W}(c_a(t) - c_v(t)) \tag{5}$$

Take the Laplace transform of equation (5), and then take the inverse Laplace transform, the portal venous concentration of ^{11}C-acetate $c_v(t)$ could be predicted by

$$c_v(t) = pe^{-pt} \otimes c_a(t), \quad p = \frac{F}{\lambda W} \tag{6}$$

where $c_a(t)$ was measured by defining ROI over the abdominal aorta adjacent to the liver and $\otimes$ denotes the operation of temporal convolution.

In Chapter 3, the model dual-input function $c_b(t)$ was calculated by

$$c_b(t) = (1 - a_v) \times c_a(t) + a_v \times c_v(t) \tag{7}$$

where a_v is the "relative portal venous contribution to the hepatic blood flow", one of the HCC indicator. Substitute $c_v(t)$ in equation (7) with equation (6), the hepatic dual-input could be modeled by

$$c_b(t) = (1 - a_v) \times c_a(t) + a_v \times (pe^{-pt} \otimes c_a(t)) \tag{8}$$

where a_v and p are the parameters to be estimated.

6.2.4 Parameter Estimation for the Dual-Model of ^{11}C-Acetate

When the dual hepatic blood supply was accounted by the model expressed by equation (8) with image-derived TAC of HA, all the parameters of the ^{11}C-acetate liver model could be estimated by fitting the model output TACs. Figure 6-1 illustrates the skeleton of this double modeling approach named as the dual-model of ^{11}C-acetate for dynamic PET studies in liver. The portal venous concentration $c_v(t)$ was determined with ^{11}C-acetate using one-compartment model relating arterial input as demonstrated at the upper left of Figure 6-1. The

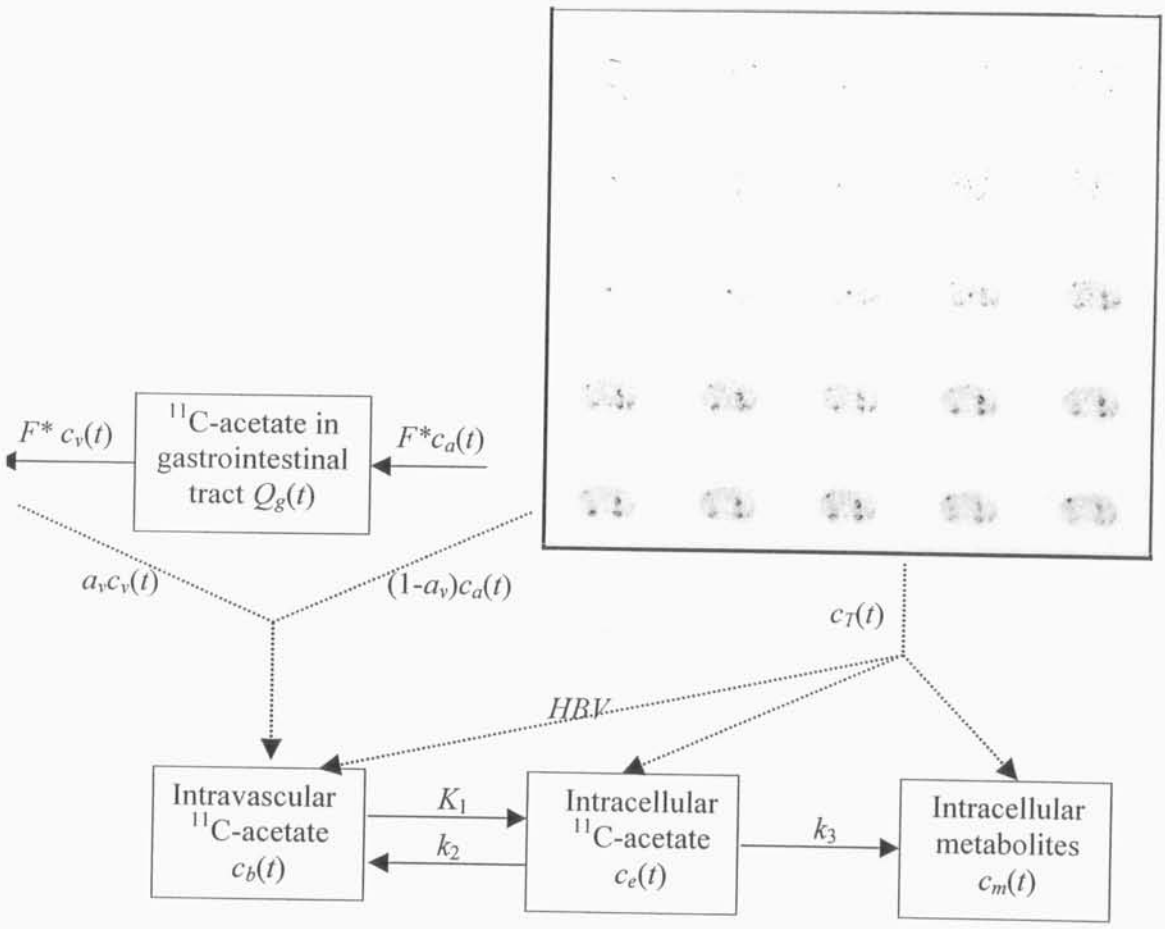

Figure 6- 1: The skeleton of the dual-model of ^{11}C-acetate for dynamic PET studies in liver. F denotes the arterial/portal venous blood flow. a_v accounts for the "relative portal venous contribution to the hepatic blood flow". *HBV* is the "hepatic blood volume" term. K_1 represents the first order rate constant for the transport of ^{11}C-acetate from blood to tissue, k_2 for reverse transport of ^{11}C-acetate from tissue to blood and k_3 for conversion of ^{11}C-acetate to its products/metabolites.

model describing the kinetics of ^{11}C-acetate in liver has two tissue compartments, which was shown at the bottom of Figure 6-1. As seen in Figure 6-1, the arterial input function $c_a(t)$ was used as the input of the dual-model and the observed total tissue time activity $c_T(t)$ was served as the dual-model output. Both $c_a(t)$ and $c_T(t)$ were acquired from the dynamic PET images displayed at the upper right of

Figure 6-1. As provided by Chapter 2, the mathematical equations for the ^{11}C-acetate model in liver could be given by

$$\frac{dc_e(t)}{dt} = K_1 c_b(t) - (k_2 + k_3) c_e(t) \tag{9}$$

$$\frac{dc_m(t)}{dt} = k_3 c_e(t) \tag{10}$$

$$c_T(t) = c_e(t) + c_m(t) + HBV \times c_b(t) \tag{11}$$

where $c_e(t)$ is the free ^{11}C-acetate concentration in intracellular space, $c_m(t)$ is the intracellular ^{11}C-acetate products/metabolites concentration, K_1 - k_3 are the rate constants, and *HBV* is to account for the contribution of ^{11}C-acetate within vascular/sinus space of liver tissue to the observed total tissue activity. In terms of macroparameters, $c_T(t)$ could be expressed as

$$c_T(t) = (B_1 + B_2 e^{-L_1 t}) \otimes c_b(t) + HBV \times c_b(t) \tag{12}$$

where

$$B_1 = \frac{K_1 k_3}{k_2 + k_3}$$

$$B_2 = \frac{K_1 k_2}{k_2 + k_3}, \qquad L_1 = k_2 + k_3$$

are the macroparameters. In addition to parameters a_v and p of the hepatic dual-input model, the dual-model of ^{11}C-acetate totally has six parameters to be estimated.

As seen in equation (12), B_1 has the same form as the forward clearance K and the "local hepatic metabolic rate-constant of acetate (*LHMRAct*)", another HCC marker. Due to the relatively large number of parameters to be estimated, instead of the nonlinear least squares (NLS) algorithm, graphed NLS (GNLS)

method [100] was applied for more reliable parameter estimation and to ensure the convergence. The flow chart of the estimation procedure for the 6-P dual model of ^{11}C-acetate using GNLS algorithm was shown in Figure 6-2.

6.2.5 Simulation Study

To test the effectiveness of the proposed 6-P dual-model of ^{11}C-acetate for hepatic PET study, computer simulation was performed as well. Two datasets representing HCC and non-tumor liver tissue were generated with two image-derived arterial input functions extracted from two clinical patients' data respectively. A pseudorandom number generator was applied to generate the Gaussian noise added to the calculated TAC and the variance structure was described as

$$\sigma^2(t_i) = \frac{\alpha \times c_T(t_i)}{\Delta t_i} \qquad i = 1,2,...,25 \qquad (13)$$

where t_i is the sampling time, which is the same as that of the clinical examination in this study, $c_T(t_i)$ is the calculated TAC, $\sigma^2(t_i)$ is the variance of $c_T(t_i)$, and α is the proportional constant representing the noise level, which is set to 0.1, 0.5 and 1 in this simulation.

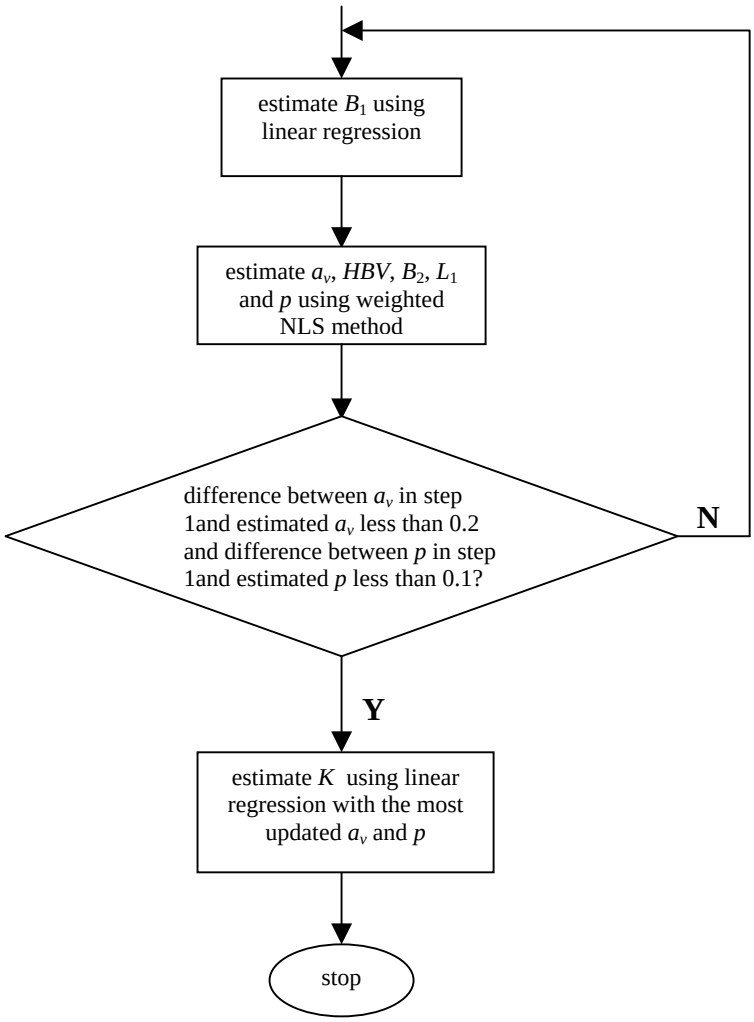

Figure 6- 2: The flow chart of the estimation procedure for the 6-P dual model of ^{11}C-acetate using GNLS method.

6.2.6 Data Analysis

To statistically examine this double modeling technique, coefficient of variation (*CV*) was used to access the reliability of parameter estimation, which is the computed measurements of the estimates' variability and given by

$$CV_P = \frac{SD_P}{P} \times 100\% \quad (14)$$

where P is the parameter estimate and SD_P is the standard deviation (SD) of P. In clinical study, SD was estimated as the square roots of the diagonal elements of the covariance matrix and the covariance matrix was estimated based on sensitivity functions. The correlation analysis was conducted in clinical study for the estimation of the two HCC indicators: the *LHMRAct* and a_v of the 6-P dual-model with image-derived arterial input and the 5-parameter (5-P) model presented previously with image-derived dual inputs with the help of experienced clinicians or the CT reference. The estimation accuracy of the 6-P dual-model in simulation study was evaluated by *bias*, which was calculated by

$$Bias = \left| \frac{P^{true} - \bar{P}}{P^{true}} \right| \times 100\% \quad (15)$$

where P^{true} is the true value of the parameter, and $\bar{P}$ is the mean value of the estimated parameter.

6.3 Results and Discussion

The aim of this study was to eliminate measuring the PV curve for quantitative hepatic studies with ^{11}C-acetate PET by modeling the dual hepatic blood supply with image-derived arterial input. The parameter estimates of a_v and p of the 6-P dual-model with image-derived TAC of HA and the estimation results of a_v of the 5-P model with image-derived TACs of both HA and PV by

GNLS method for clinical study were summarized in Table 6-1. Results were given as the estimated value ± *SD*. As shown in Table 6-1, the two sets of estimated a_v are approximated to each other. For the eight non-tumor liver tissue regions, the estimated a_v expressed by the mean value ± *SD* are 0.8304 ± 0.0942 and 0.8452 ± 0.0694 for the 5-P model and 6-P dual-model respectively; for the two HCC regions, the estimated a_v are 0.4547 ± 0.1575 and 0.4332 ± 0.1272 for the 5-P model and 6-P dual-model respectively. As revealed in Table 6-1, for the 6-P dual-model, the estimated a_v of the two HCC regions is much less than that of the non-tumor liver parenchyma, which is case of the 5-P model as well, and its significance by t-means test is 0.0002. The estimated *p* values listed in Table 6-1 are case-dependent. For each patient, the *p* values of the two ROIs show little difference as shown in Figure 6-3, which is of great value for the computation of parametric images since parameter *p* can be estimated only once for each serial dynamic images and set as a *prior* for thereafter pixel-by-pixel-based parameter estimation. Figure 6-4 depicts the PV curve calculated by equation (6) with the estimated *p* and image-derived arterial input of one clinical dataset. As seen in Figure 6-4, the calculated PV curve agrees well with the image-derived PV curve for the first 11 points and the last 4 points. Some unsatisfied fitted points might be partially due to the noisy measurements.

The parameter estimates of *K* of the two models by GNLS method for clinical study were listed in Table 6-2. For the eight nontumor liver tissue ROIs, the estimated *K* values for the 5-P model and 6-P dual-model are 0.1681 ± 0.0146 and 0.1592 ± 0.0190 respectively; whereas, for the two HCC ROIs, the estimated *K* are 0.3942 ± 0.1714 and 0.3799 ± 0.1184 for the 5-P model and 6-P

Table 6- 1: Results of the estimated a_v of the 5-P model with image-derived dual inputs and estimated a_v and p of the 6-P dual-model with image-derived arterial input for the clinical datasets using GNLS method.

Datasets Number[1]	5-P model	6-P dual-model	
	a_v	a_v	p
1	0.9085±0.0714	0.9127±0.6158	0.4743±0.2450
2	0.9117±0.1089	0.9194±0.2854	0.4109±0.2194
3	0.8899±0.0673	0.8482±0.1311	0.3292±0.0787
4	0.7196±0.1384	0.7620±0.4194	0.3019±0.2096
5	0.7192±0.0643	0.7618±0.6960	0.3414±0.1177
6	0.7127±0.0391	0.7798±0.7311	0.3620±0.1239
7	0.8978±0.0448	0.8605±0.4968	1.2046±1.1279
8[2]	0.3433±0.2514	0.3433±0.2238	1.1790±0.9876
9	0.8837±0.1012	0.9175±0.3065	0.4751±0.1583
10[2]	0.5661±0.1196	0.5231±0.3462	0.5029±0.8233

Notes:
1. Two ROIs were extracted from each patient. The datasets were numbered like this: 1 and 2 from patient 1, 3 and 4 from patient 2 and so on.
2. Datasets 8 and 10 represent HCC.

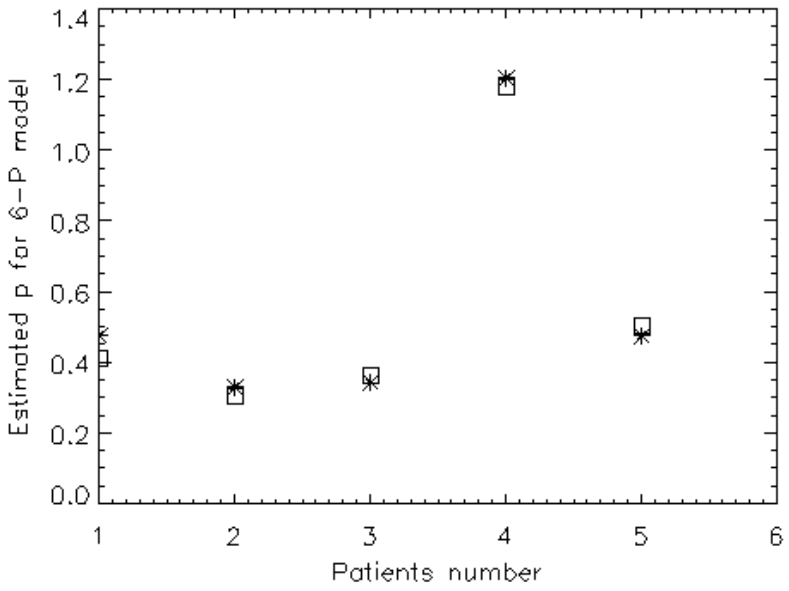

Figure 6- 3: The parameter estimates of p of the 6-P dual-model for clinical study. The estimated p of the two ROIs from the same patient was differentiated by symbols asterisk and square.

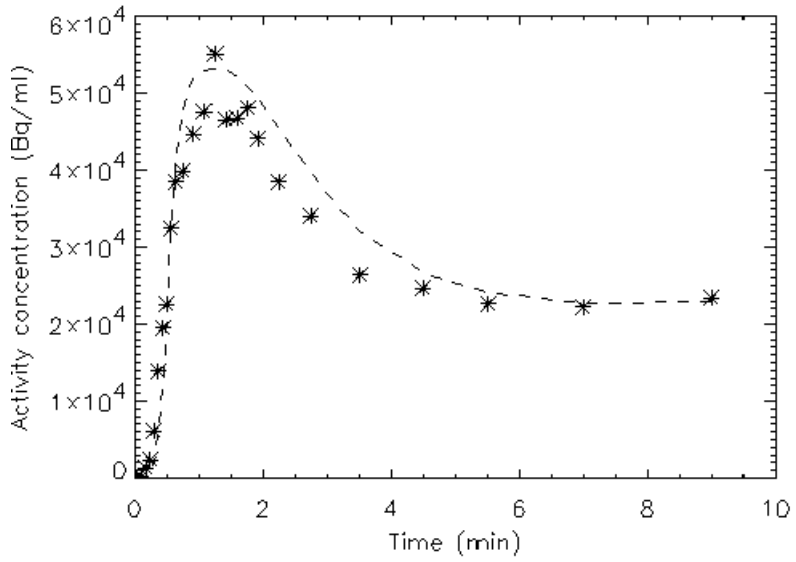

Figure 6- 4: Calculated PV curve (the dashed line) with the estimated *p* and image-derived TAC of HA of one clinical dataset. The points denoted by symbol asterisk are the image-derived PV measurements.

Table 6- 2: Estimation results of parameter *K* of the 5-P model with image-derived dual inputs and 6-P dual-model with image-derived arterial input for the clinical datasets using GNLS method.

Datasets Number	5-P model		6-P dual-model	
	K	*CV*	*K*	*CV*
1	0.1642	9.71	0.1651	2.26
2	0.1764	10.80	0.1765	2.70
3	0.1603	25.61	0.1496	6.88
4	0.1781	30.31	0.1605	16.99
5	0.1485	10.86	0.1291	4.92
6	0.1551	9.20	0.1391	3.75
7	0.1679	8.39	0.1859	4.52
8	0.2731	12.17	0.2962	9.53
9	0.1944	10.06	0.1682	5.43
10	0.5154	2.82	0.4636	1.19

Note: See notes of Table 6-1.

dual-model respectively. Same as the 5-P model, the estimated *LHMRAct* (the forward clearance *K*) of the two HCC regions of the 6-P dual-model is significantly higher than that of the nontumor liver tissue and its significance by t-means test is 0.0003.

As shown in Tables 6-1 and 6-2, the two sets of estimates of both a_v and *K* of the 5-P model and 6-P dual-model agree well with each other. The correlation coefficients by the correlation analysis of the two sets of estimated a_v and *K* for each defined ROI are 0.9784 and 0.9831 respectively. The regression equations relating a_v and *K* measured with the 5-P model and 6-P dual-model for the ten clinical ROIs were depicted in Figure 6-5. As illustrated in Figure 6-5, the estimated a_v and *K* of the two models correlate closely with each other. All the above findings might indicate that the tough issue of obtaining the PV curve for hepatic quantitative study might be addressed by the presented 6-P dual-model. The model fitted curves according to the 5-P model and 6-P dual-model for one patient data including one HCC ROI and one non-tumor liver tissue ROI, were shown in Figure 6-6. For the non-tumor liver tissue ROI, the two fitted curves of the two models show no much difference at the beginning and ending stages and some difference at the middle stages; while for the HCC ROI, the two fitted TACs show little difference with each other.

As revealed in Table 6.1, the *CVs* of the estimated a_v increase modestly when compared with those of the 5-P model, which could be explained that more number of parameters to be estimated reduces the estimation reliability. Nevertheless, the estimates of a_v of the 6-P dual-model are still generally reliably

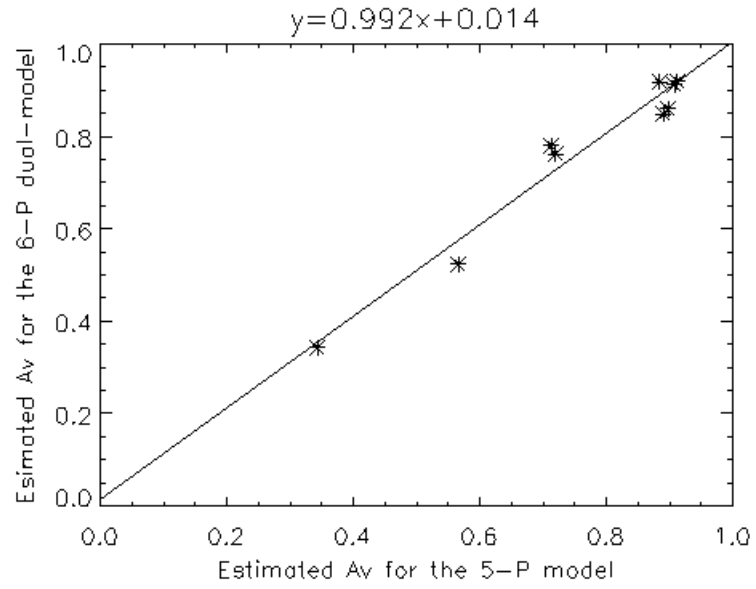

(a)

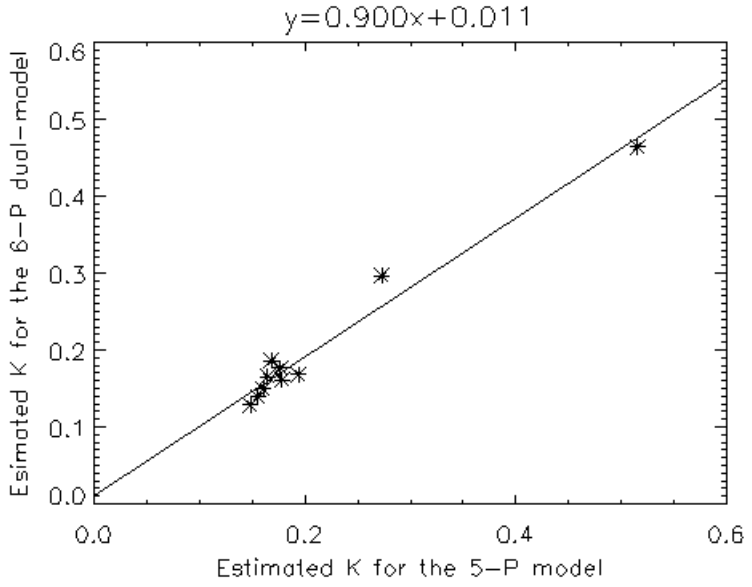

(b)

Figure 6- 5: Relationship between the estimated a_v (a) and K (b) of the 5-P model with image-derived TACs of both HA and PV and the 6-P dual-model with image-derived TAC of HA for the ten clinical ROIs.

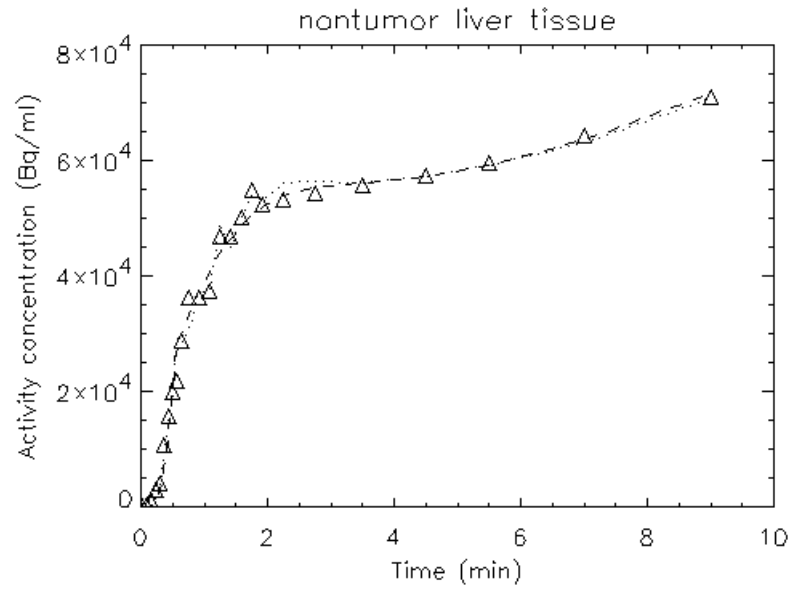

(a)

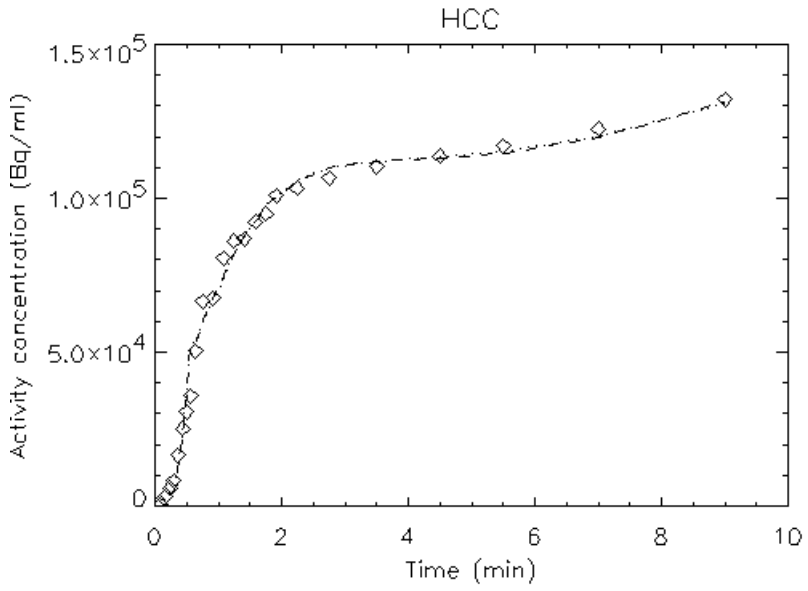

(b)

Figure 6- 6: Graphs show the generated TACs of the nontumor liver tissue ROI (a) and the HCC ROI (b). The points denoted by symbols triangle and diamond represent the nontumor liver tissue and HCC measurements respectively. The dashed lines are the fitted TACs using the 6-P dual-model; while the dotted lines are the fitted TACs using the 5-P model.

attainable. The reliability of the estimated *p* is acceptable as well since most *CVs* are less than or around 50%. As listed in Table 6-2, nine *CVs* of the estimated *K*

of the 6-P dual-model are less than 10%, indicating very reliable estimation. When compared with the *CVs* of the 5-P model, the estimated *K* derived from the 6-P dual-model are much more reliable as demonstrated in Figure 6-7. The average *CV* values of the estimated *K* of the 6-P dual-model and 5-P model are 5.82% and 12.99% respectively. In addition, as mentioned above, for each patient, parameter *p* need to be estimated only once and then could be set as a *prior* for other ROIs or pixels, therefore, the *CVs* of both a_v and *K* could be further reduced.

Computer simulation was performed to test the 6-P dual-model of ^{11}C-acetate as well. Two simulation studies, including one HCC study, were conducted with two image-derived arterial TACs from two patients. The GNLS estimation results of the mean values, *biases*, and *CVs* of the parameters K_1, k_2, k_3, *HBV*, a_v, *p* and *K* (*LHMRAct*) of the 6-P dual-model calculated from 100 simulation runs were presented in Table 6-3. As seen in Table 6-3, all *CVs* are less than 20% for non-tumor liver tissue case and less than 36% for HCC case. All *biases* are less than or around 5%. Therefore, reliable and accurate parameter estimation of the 6-P dual-model with image-derived arterial input could be achieved. As shown in Table 6-3, the reliability and accuracy of the estimated rate constant parameters K_1, k_2 and k_3 are comparable with one another for the same dataset. Though the estimation of *HBV* and *p* shows less reliable than that of other parameters (referred to Table 6-3), the reliability is still acceptable and the accuracy is satisfied especially for the estimated *p* of the nontumor liver tissue dataset. Concerning the two HCC indicators: the *LHMRAct* (the forward clearance *K*) and a_v, they could be accurately and reliably estimated according to the provided data

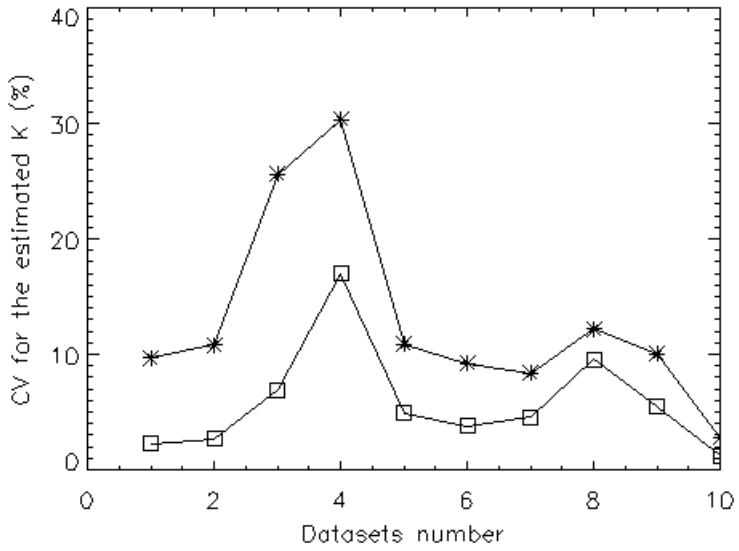

Figure 6- 7: Comparison of the *CVs* of the estimated *K* of the 5-P model with image-derived dual inputs and the 6-P dual-model with image-derived arterial input for the ten clinical ROIs. Solid line marked by asterisk stands for the results of the 5-P model and solid line marked by square stands for the results of the 6-P dual-model.

in Table 6-3. In particular, *K* is the most reliably and accurately estimated parameter among all of the parameters of the 6-P dual-model, since the *CVs* are all less than 5% and the *biases* are all less than 2.5%, furthermore, the *biases* of dataset 1 are even less than 0.5%. The presented results show that all the required parameters of this 6-P dual-model without the known PV curve could be identified and the parameter estimates are reliable and accurate. The fitting examples of the simulation study with different noise levels as 0.1, 0.5, and 1, were drawn in Figure 6-8. It could be seen that the simulation data of the 6-P dual-model could be fitted very well.

Table 6- 3: Estimation results of the parameters of the 6-P dual-model using GNLS method for two simulation studies, where the second dataset (b) represents HCC case. The estimated parameters in this table represent their mean values. The mean values, *biases*, and *CVs* were calculated from 100 simulation runs.

(a) true value: $K_1 = 0.85$, $k_2 = 0.75$, $k_3 = 0.20$, $HBV = 0.30$, $a_v = 0.75$, $p = 1.00$, $K = 0.1789$

Noise level	K_1	$bias_1$(%)	CV_1(%)	k_2	$bias_2$(%)	CV_2(%)	k_3	$bias_3$(%)	CV_3(%)
0.1	0.8666	1.96	0.64	0.7774	3.65	0.49	0.2027	1.33	0.71
0.5	0.8487	0.16	5.54	0.7643	1.90	3.66	0.2057	2.87	5.81
1.0	0.8304	2.31	8.98	0.7450	0.67	7.29	0.2074	3.70	9.31

Noise level	HBV	$bias_H$(%)	CV_H(%)	a_v	$bias_a$(%)	CV_a(%)	p	$Bias_p$(%)	CV_p(%)	K	$bias_K$(%)	CV_K(%)
0.1	0.2919	2.70	1.41	0.7459	0.54	0.54	0.9996	0.04	0.87	0.1792	0.14	0.25
0.5	0.3062	2.08	14.43	0.7565	0.87	4.28	0.9990	0.10	4.41	0.1795	0.29	1.30
1.0	0.3167	5.56	19.80	0.7662	2.16	6.51	1.0083	0.83	11.73	0.1796	0.35	2.43

(b) true value: $K_1 = 1.65$, $k_2 = 0.70$, $k_3 = 0.14$, $HBV = 0.30$, $a_v = 0.36$, $p = 0.40$, $K = 0.2750$

Noise level	K_1	$bias_1$(%)	CV_1(%)	k_2	$bias_2$(%)	CV_2(%)	k_3	$bias_3$(%)	CV_3(%)
0.1	1.6637	0.83	2.06	0.6899	1.44	1.64	0.1392	0.86	2.77
0.5	1.6780	1.69	9.22	0.6987	0.19	10.76	0.1401	0.09	7.97
1.0	1.7023	3.17	14.93	0.7157	2.24	15.33	0.1434	2.44	14.58

Noise level	HBV	$bias_H$(%)	CV_H(%)	a_v	$bias_a$(%)	CV_a(%)	p	$Bias_p$(%)	CV_p(%)	K	$bias_K$(%)	CV_K(%)
0.1	0.2994	0.21	2.88	0.3607	0.18	2.81	0.3830	4.24	7.24	0.2792	1.53	0.67
0.5	0.3038	1.28	15.63	0.3674	2.04	13.89	0.3930	1.75	20.59	0.2793	1.58	2.29
1.0	0.3120	3.99	29.30	0.3824	6.22	21.30	0.4209	5.23	35.90	0.2808	2.10	4.09

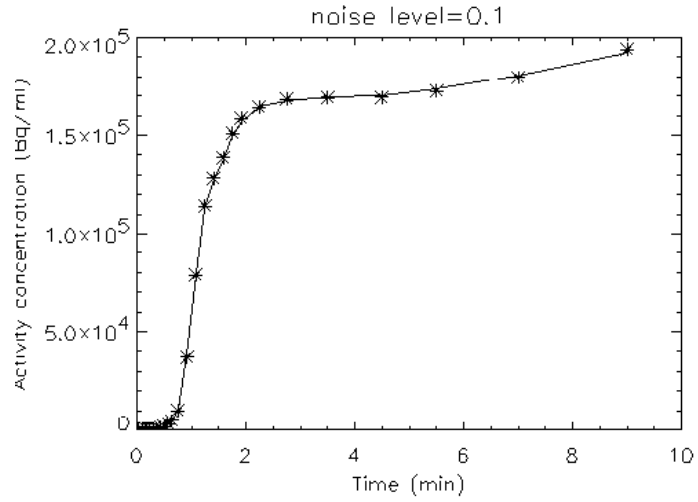

(a)

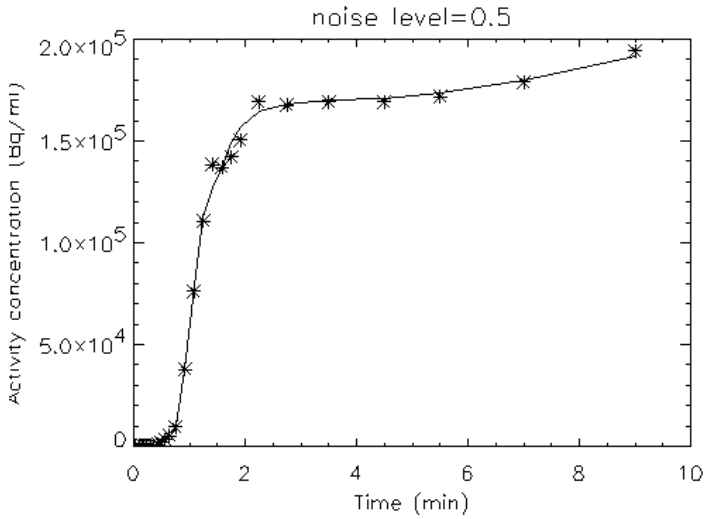

(b)

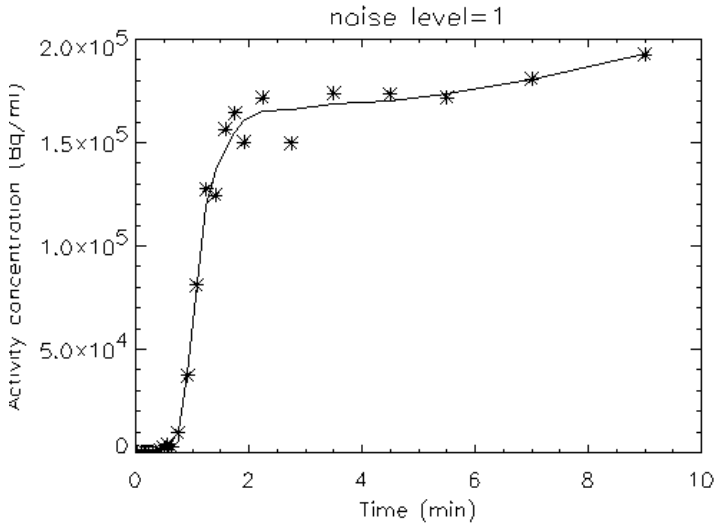

(c)

Figure 6- 8: Fitting results of the randomly chosen simulation data denoted by asterisk with the noise levels 0.1 (a), 0.5 (b) and 1 (c) for HCC study.

6.4 Conclusion

In this chapter, modeling the dual hepatic blood supply was proved very effective with respect to the adequacy of fitting the clinical ^{11}C-acetate PET data in liver, to eliminate the PV curve extraction for the hepatic quantitative study, which is a very challenging task in the literature. The parameter estimates of the 6-P dual-model are approximated and closely related with the fitting results of the 5-P model with image-derived dual inputs, which might indicate that the 6-P dual-model could successfully account for the hepatic dual blood supply. In addition, it allows more reliable estimation of the parameter *LHMRAct*. The simulation study suggests that all the parameters of the 6-P dual-model could be estimated reliably and accurately, especially for the two HCC indicators: the *LHMRAct* and a_v. Therefore, this new model structure is an appropriate representation of the system and proposes a better way for the early detection of HCC *in vivo*. Besides, with the obtainment of the parameter *p*, the described modeling approach shows great potency for providing the functional physiological parametric images of the two HCC indicators.

Chapter 7 Automatic Detection Approaches for Hepatocellular Carcinoma Using ^{11}C-Acetate Positron Emission Tomography

7.1 Introduction

As mentioned in the previous chapters that the model input function BTAC, is usually represented by a sequence of arterial or arterialized blood samples, which is in general very invasive and requires extra personnel and processing time. Moreover, the liver has a dual source of blood supply: the hepatic artery (HA) and the portal vein (PV), it is highly invasive and virtually impossible in clinical settings to count the radioactivity of the portal venous blood by direct catheterization and sampling. Therefore, regions-of-interest (ROIs) delineation of HA and PV is required from the dynamic PET images. However, PET cannot provide precise anatomic localization due to its relatively poor spatial resolution and high noise level. Manual placement of ROIs is subject to operator's skill and lacks of reproducibility [101]. It is also time consuming. Furthermore, the sizes of both HA and PV are very small, which makes the delineation even more difficult. Therefore, automatic segmentation should be our preliminary step for enhancement of visualization and ROI analysis. In addition, automatic

segmentation could provide consistent and reproducible results and an overall reduction in time for data analysis [101].

Clustering algorithms [102] achieve region segmentation by partitioning the image into sets of clusters of pixels that have strong similarity in the feature space. This approach has been used with some success in segmentation of PET images [103] - [106]. For dynamic PET images, each pixel of a slice could be represented by a time-activity curve (TAC). In our study, cluster analysis is used to segment the dynamic PET images by merging a number of TACs according to their shapes and magnitudes into a small number of distinct characteristic classes so that the TACs within a cluster showing the greatest similarity to each other but are dissimilar to those extracted from other clusters [101]. Little published data in the literature regarding segmenting the clinical dynamic ^{11}C-acetate PET images in liver by cluster algorithms. In this chapter, we would perform cluster analysis to these clinical images and fit the curves of the segmented regions of HCC and non-tumor liver tissue with the TAC of the segmented arterial region for the 6-P dual-model proposed in Chapter 6. The effectiveness of this method would be evaluated by the comparison between the fitting results of the manual-drawn ROIs and auto-drawn ROIs.

As mentioned in Chapter 2, the tracer arriving at the PV is delayed and dispersed in comparison with that of the HA, which makes its activity in PV similar to that in the normal liver tissue. If the number of clusters is insufficient, the region of PV would be merged into the surrounding hepatic parenchyma and cannot be distinguishable; if the number of clusters is adequate to identify the PV,

several “meaningless” clusters would appear. A two-step segmentation method based on clustering algorithm and with the combination of spatial and temporal information provided by the dynamic PET liver images, was proposed as well.

7.2 Segmentation Schemes

The data acquisition procedure is the same as that in the previous chapters. Our aims of the segmentation are to differentiate image pixels of the pathological regions: HCC, from other liver masses, at the same time extract the specific anatomic structures: blood vessels, liver *etc* from the dynamic images.

7.2.1 Cluster Algorithm Applied to Segment the Clinical Dynamic ^{11}C-Acetate PET Images in Liver

The presented segmentation method based on cluster analysis was applied to the clinical dynamic ^{11}C-acetate PET images in liver. The segmentation was performed independently on each slice. The basic idea of the segmentation method is to utilize clustering algorithm to merge all the pixels’ TACs according to their shapes and magnitudes into a small number of distinct characteristic clusters. The cluster centroid is the average of all pixels’ TACs in the cluster. Assume that there are totally n pixels’ TACs of p time frames in the dynamic PET data and m distinct characteristic curves ($m << n$). Each pixel’s TAC belongs to only one of the m curves. The clustering algorithm can segment the

dynamic PET data into *m* curves automatically based on a least squares distance *D*

$$D\{z_{i,}\mu_j\} = \sum_{j=1}^{m}\sum_{i=1}^{n}\left\|z_i - \mu_j\right\|^2 \quad (1)$$

where z_i is the *i*th pixel's TAC in the PET data; μ_j is the centroid of *j*th cluster [101]. Each pixel's TAC is allocated to its nearest cluster centroid according to

$$\left\|z_l - \mu_i\right\|^2 < \left\|z_l - \mu_j\right\|^2 \; i, j = 1,2,...,m, i \neq j \quad (2)$$

where z_l is the *l*th pixel's TAC in the PET data; μ_i and μ_j are the *i*th and *j*th cluster centroid respectively. The cluster centroids will be updated by averaging all pixels' TACs in the cluster after each round of allocation based on equation (2) to minimize *D*. Then, the *n* TACs are needed to be reallocated according to the new cluster centroids. The allocation and updating iteration wouldn't cease until no TAC is needed to be reallocated from a cluster to another. The number of clusters was assumed as 8 (excluding the background) as a *prior* in this segmentation according to [101].

7.2.2 Two-Step Segmentation Method Based-on Cluster Analysis

In the first step of the segmentation, we aim to extract the PV, which has very similar characteristic with the surrounding liver tissue. An option to cluster the similar objects is to increase the number of clusters. Therefore, we performed the segmentation on the dynamic ^{11}C-acetate PET liver images with a relatively large number of clusters *k* by using the above-mentioned method in section 7.2.1. *k*

was assigned to a value that the PV can be distinguished from its surroundings. The segmented PV may be validated by the spatial information: its invariable anatomical position being posterior to the pancreatic head that shows the most intense physiological uptake of ^{11}C-acetate, or by direct reference to the CT images. Since PV could not be recognized clearly on the ^{11}C-acetate PET liver images, contrast enhancement techniques were conducted to help validate the segmentation result. After the first round of segmentation, the PV would be identified; all the clusters will be labeled and isolated. The remaining clusters were then put into a queue. In this stage, the PET images were over-segmented.

In the first step of segmentation, each cluster has equal significance to the result, however it is unnecessary to retain all the other clusters and some clusters are even “meaningless”. Therefore, in the second step, cluster analysis was again performed, but only to the pixels belong to the clusters inside the queue. This time, the number of clusters was set to be 8 (excluding the background) as well. Since the cluster of the PV was labeled and isolated, it would not affect the result of the second step segmentation. In addition, it will not be interfered. Finally, 9 clusters would be obtained and all the ROIs needed for the quantitative analysis of the ^{11}C-acetate PET liver images could be extracted.

7.3 Parameter Estimation

With the extraction of HA curves, the two HCC indicators: the "local hepatic metabolic rate-constant of acetate (*LHMRAct*)" (the forward clearance *K*) and the "relative portal venous contribution to the hepatic blood flow (a_v)" would be estimated by the GNLS algorithm presented in Chapter 5 for the 6-P dual-model. The data points chosen for the graphical analysis in GNLS are from 3 - 10 min.

7.4 Results

7.4.1 Segmentation and Estimation Results for the 6-P Dual-Model Using Cluster Analysis

Figure 7-1 depicts the console for segmenting the clinical dynamic ^{11}C-acetate PET images in liver using cluster analysis. Figure 7-2 displays its segmentation results for one slice of clinical dataset suffered from HCC. The enclosed region in the center of the image is the HA region and the enclosed region in the left upper of the image represents HCC region. As shown in Figure 7-2, the anatomic structures such as the liver, kidney, spleen *etc.* could be well recognized. The region of PV could not be segmented using this method. The activity concentration value for each region could be obtained by clicking any area in that region and the results would be displayed in the blank area of the right bottom of Figure 7-2.

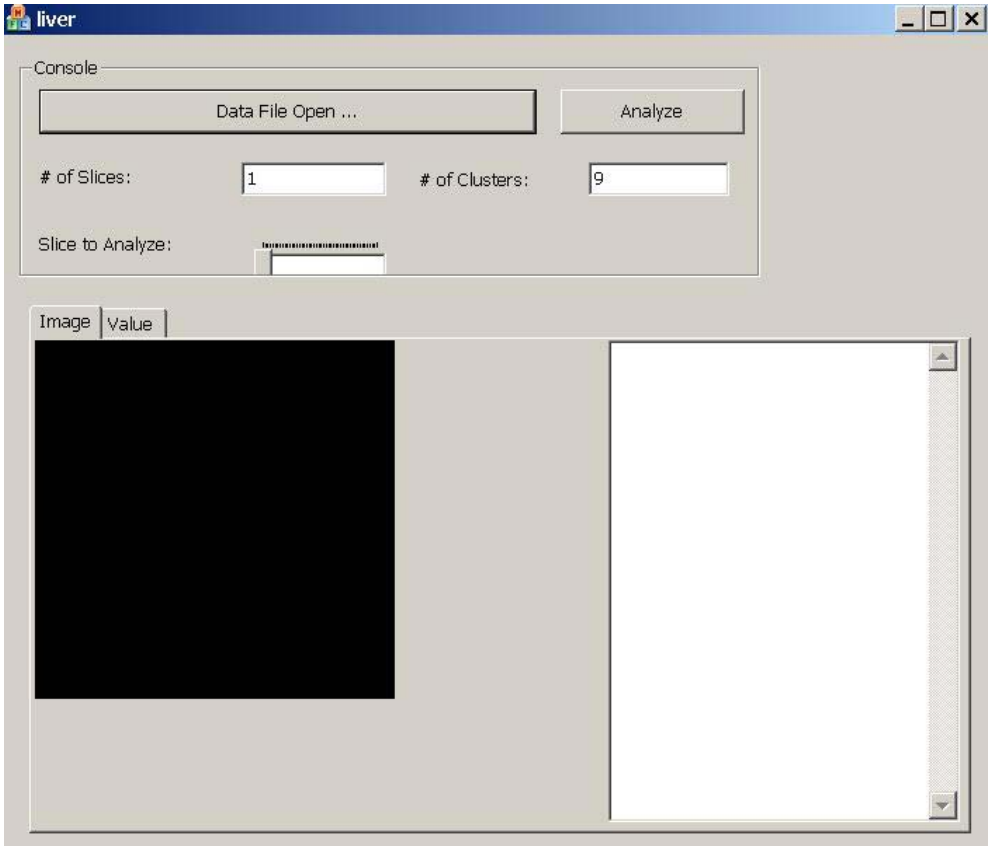

Figure 7- 1: The console for segmenting the clinical dynamic ^{11}C-acetate PET images in liver using cluster analysis.

The extracted HCC and non-tumor liver tissue curves were then fitted to the 6-P dual-model by GNLS algorithm with the auto-extracted TAC of HA. Table 7-1 summarized the estimation results of a_v, K and p of the 6-P dual-model with the manual-delineated and auto-delineated HA region respectively. As listed in Table 7-1, the two sets of estimated values with the two kinds of TACs of HA are comparable with each other.

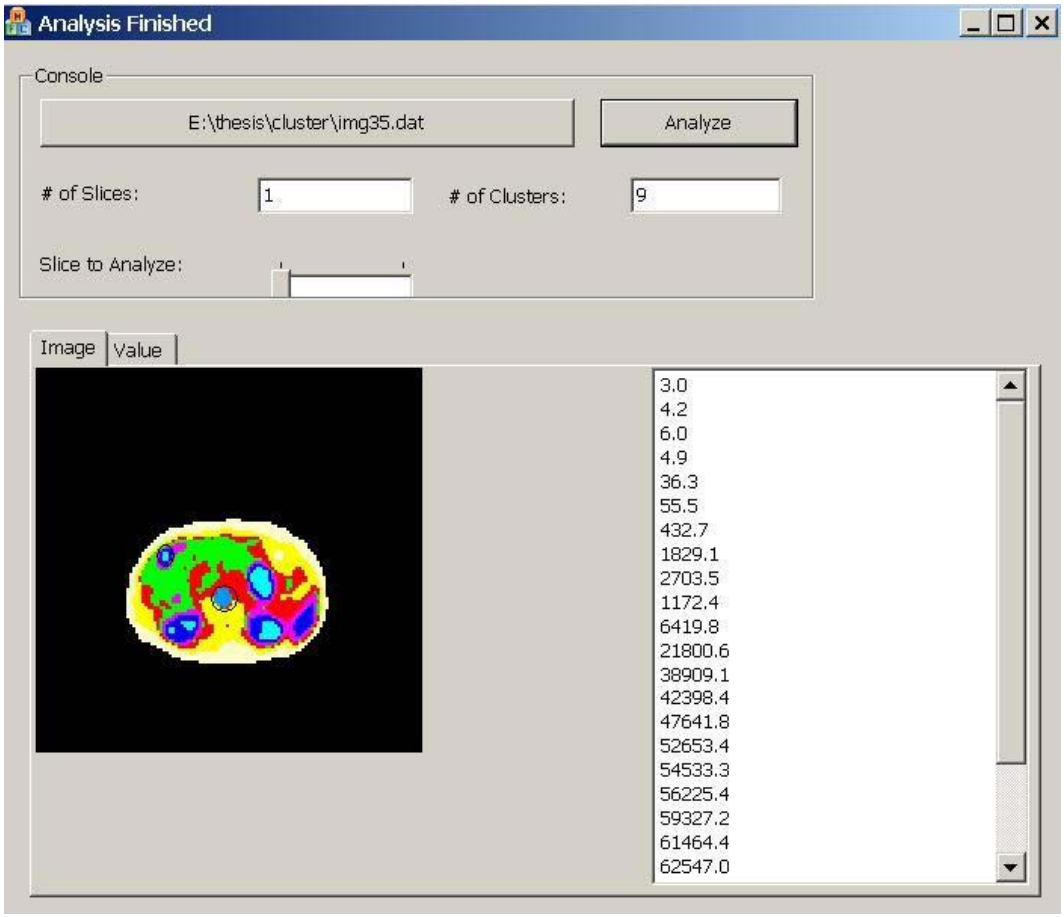

Figure 7- 2: The segmentation results of one slice of clinical dynamic ^{11}C-acetate PET images in liver using cluster analysis.

Table 7- 1: The parameter estimates of a_v, K and p of the 6-P dual-model.

ROIs	manual			auto		
	a_v	K	p	a_v	K	p
Liver	0.9175	0.1682	0.4751	0.8818	0.1490	0.5043
HCC	0.5065	0.3768	0.4358	0.4226	0.3175	0.4006

7.4.2 Results of the Two-Step Segmentation Method Based-on Cluster Analysis

Figure 7-3 demonstrates the proposed two-step segmentation results of another slice of clinical dynamic ^{11}C-acetate PET liver images in comparison to the segmentation results by using the first segmentation method. From Figure 7-3 (a), it could be seen that the liver, HA, HCC *etc.* could be identified, but the PV were merged into the surrounding hepatic parenchyma. The results are also of 8 clusters. 24 clusters were adopted in the first step segmentation whose result was shown in Figure 7-3 (b). The PV can be differentiated clearly, however, some anatomical structures were distorted and some clusters were even "meaningless" compared to Figure 7-3 (a). Figure 7-3 (c) illustrates the result for the two-step segmentation using 9 clusters totally. The PV still could be seen; other ROIs in Figure 7-3 (a) also appear in Figure 7-3 (c) and their respective locations and shapes are nearly unchanged when compared with Figure 7-3 (a). Therefore, all the ROIs needed for the quantitative study could be extracted. Figure 7-4 shows the TACs of the clusters of HA, PV, HCC and non-tumor liver tissue obtained from the segmentation results.

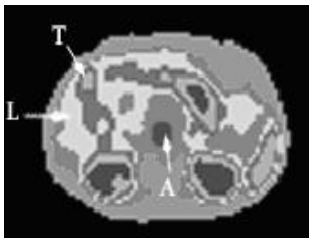

(a)

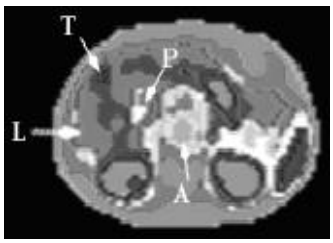

(b) (c)

Figure 7- 3: (a) The segmentation result of another slice of clinical dynamic ^{11}C-acetate PET images using the first segmentation method; (b) result of the first step segmentation of the two-step segmentation method; (c) final result of the two-step segmentation. A = HA, L = liver, P = PV, T = HCC.

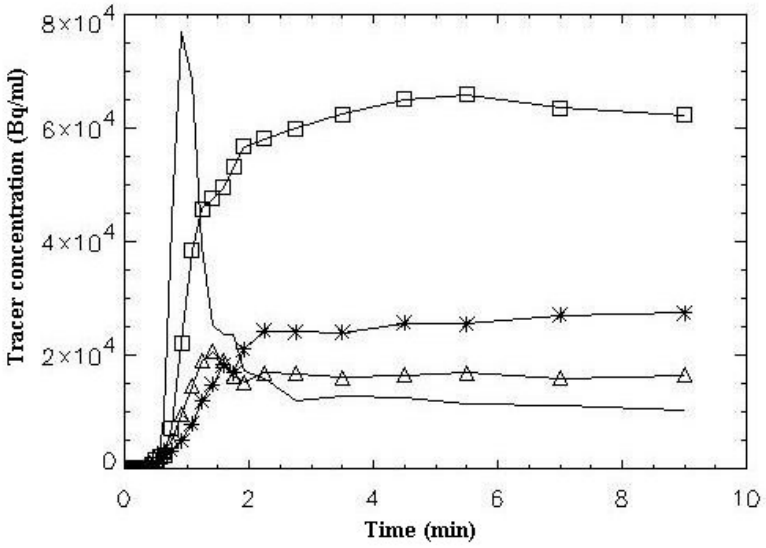

Figure 7- 4: TACs extracted from the results of the proposed two-step segmentation method. Pure solid line stands for the curve of HA; solid line marked by triangle is for the PV, square for HCC and asterisk for the non-tumor liver tissue.

7.5 Conclusion

The approaches presented in this chapter could segment the dynamic ^{11}C-acetate PET liver images automatically. All the ROIs for the quantitative study of ^{11}C-acetate liver characteristics could be obtained by using the proposed segmentation methods. This segmentation may also be useful as a preprocessing step before fast generation of the parametric images of these two physiological parameters of the liver, which could be of great value to detect HCC automatically. Additionally, the proposed segmentation methods may open a window for automatic detection of other PET studies.

Chapter 8 Conclusions and Future Works

8.1 Conclusions

Functional imaging techniques such as positron emission tomography (PET) have been proven very promising for the evaluation of distribution of malignant tumors. Hepatocellular carcinoma (HCC), the most frequent malignant tumor in liver, is the most common malignancy worldwide in males. Most cases of HCC are discovered late and less than 10% are cured with surgical resection. Therefore, early and accurate detection of HCC will greatly increase the chance of cure and survival in patients. However, 40-50% of HCC could not be detected by the well-established FDG-PET. The investigation of ^{11}C-acetate on HCC by Ho *et al*. [6] revealed that the detection of HCC could be greatly aided by the introduction of this tracer. No data exist in the literature regarding this study before Ho and preliminary results are highly encouraging, along with the dual hepatic blood supply (hepatic artery and portal vein). Therefore, further studies on the tracer kinetic modeling, model validation and discrimination; quantification of ^{11}C-acetate metabolism in the liver and the dual hepatic blood supply so as to extract the maximum quantitative information during the scan period; computer assisted diagnosis; efficient and reliable algorithms to estimate

the model parameters, are essential for the detection of HCC, and form the major objectives of this study.

Quantitative studies are crucial for accurately applying techniques for the evaluation of HCC. In theory, dynamic data may add an incremental value to earlier disease detection than simple static data acquisition. Thus a suitable dynamic compartment model describing the kinetics of ^{11}C-acetate in liver is the premise for quantification. Resolving the model-related functional (kinetic) parameters will provide a better understanding on and correlation with the variable histopathology of this devastating tumor. In Chapter 2, a three-compartment model consisting of four parameters with dual inputs was proposed and compared with that of five parameters. Estimation of the adequacy of these models is based on some statistical study. A new physiological parameter called the "local hepatic metabolic rate-constant of acetate (*LHMRAct*)" was introduced. It was concluded that this three-compartment four-parameter model with dual input functions was suitable in mapping the kinetic characters of ^{11}C-acetate in a 10 min dynamic PET imaging of the liver. The model has provided a better understanding of the complexity and biochemistry of the behavior of this tracer in HCC and non-tumor liver tissue. A 10 min dynamic acquisition of ^{11}C-acetate PET imaging may provide enough valuable quantitative data. The parameter *LHMRAct* could be considered as potential indicator of metabolism (other than SUV) for evaluating HCC. ^{11}C-acetate is not just a complementary tracer to FDG, in fact a better tracer than FDG for detection of HCC.

Since in real pathology, both tumor and non-tumor liver tissue can be heterogeneous in the distribution and proportion of the two blood supplies. To further improve the accuracy of quantitative analysis, Chapter 3 presents a new model structure to investigate the individual proportion of the hepatic artery (HA) and portal vein (PV) in different regions of interest (ROIs). An extra parameter a_v was included in the model input function to describe the contribution of PV to the total liver blood flow. This study suggests that the differential portal and arterial contribution to the liver blood supply could be extracted from the dynamic PET measurements noninvasively using tracer kinetic modeling techniques. The estimated a_v value is reasonable and concordant with the clinical, radiological and pathological conditions. It adds supportive evidence to the observation that liver metastases derive a much greater proportion of their blood supply from the hepatic arterial flow when neovascularization is a common cancer growth characteristic, with a smaller proportion from the portal venous flow. Whether the estimated a_v value might have an alternative role as a vascular indicator that can reflect subtle neovascularization in early HCC tumor growth requires more research. In the presence of pathological changes of cirrhosis, the background liver parenchyma shows heterogeneous vascular changes such as significant arterioportal and portovenous systemic shunting. All these confounding factors will add to the complexity of background noise, making it difficult to evaluate for small and well- differentiated HCC lesions. This is the same reason for a low detection accuracy even by the most advanced triple-phase CT technology when severe hepatic cirrhosis is encountered. The measurement of a_v, however, may directly provide a measure of the "vascular deviation" status from the normal liver

vasculature, and, therefore, may provide an indirect way of reflecting cirrhosis using PET (which is normally evaluated by CT). The presented results show that all the required parameters can be quantified simultaneously and the parameter estimates are reliable and accurate. The three-compartment four-parameter model plus an extra weight parameter in the dual-input function is a more appropriate representation of the physiological system by describing the kinetic characters of ^{11}C-acetate in a 10-minute dynamic PET imaging of the liver, including a more consistent estimation of *LHMRAct*. In summary, the above findings and proposal may provide a better understanding of the perfusion and metabolic function of normal liver and liver cancer.

In Chapters 2 and 3, the model parameters were estimated by the classic nonlinear least squares regression (NLS) algorithm. Nevertheless, when the number of parameters to be estimated is relatively large, “good” initial guess is required and the computational burden is considerable, which limits its application in clinical environments for image-wide parameter estimation. Although a variety of fast parametric imaging techniques have been developed, most of them focus on single input systems, which do not provide optimal solution for dual-input liver system parameter estimation. In Chapter 4, a dual-input-generalized linear least squares (D-I-GLLS) algorithm was proposed to identify the model parameters including the parameter in the dual-input function. It achieves a comparable estimation quality in terms of coefficient of variance (*CV*) with NLS method by computer simulation. The accuracy of most of the parameter estimates for ^{11}C-acetate liver kinetic model is satisfactory. This computationally efficient algorithm could reliably identify all the parameters

including the parameter in the dual-input function. Only one initial guess is required for the fitting procedure and the results are not sensitive to this initial guess. Therefore, this D-I-GLLS algorithm is potentially useful for the construction of parametric images from ^{11}C-acetate dynamic PET liver images and is generally applicable to other dual-input biomedical system parameter estimation.

Chapter 5 proposes two novel parameter estimation techniques: graphed NLS (GNLS) and graphed dual-input generalized linear least squares (GDGLLS) algorithms, for ^{11}C-acetate liver kinetic model with dual hepatic blood supply using dynamic PET images. Clinical and simulated data were utilized to test the proposed algorithms by a systematic statistical analysis. When compared with the NLS approach, more reliable parameter estimates could be provided by GNLS method for clinical study. Due to the reduced number of parameters to be estimated by NLS regression, the computational burden of GNLS is reduced when compared with the standard NLS method and the fitting results are less affected by the initial guess because the predetermined B_1 was considered as a *prior*. GDGLLS algorithm could generally identify all the parameters more reliably including the parameter in the dual-input function and the fitting procedure is drastically faster than NLS method. Compared with NLS fitting, both presented algorithms could achieve a comparable estimation accuracy of the two HCC indicators. When the noise level is high, both methods could even achieve better fitting accuracy of Parameter *K*. Due to the robustness and computational efficiency, the two presented algorithms might be promising for providing the functional physiological parametric images of the two HCC

markers. Therefore, the two estimation algorithms could provide better ways in the noisy clinical environment for the early detection of HCC.

For quantification of the ^{11}C-acetate liver studies, both time-activity curves (TACs) of HA and PV are desired. However, directly measuring them by the widely adopted blood sampling or cannulation procedure is invasive. Moreover, accurate measuring the TAC of PV in the human liver is difficult to achieve, as the tracer arriving at the PV is delayed and dispersed, and furthermore, the TAC of PV is considerably contaminated by the surrounding liver tissue, which makes it virtually impractical to differentiate the PV curve by the currently developed techniques. To noninvasively and efficiently access the portal venous blood flow, Chapter 6 investigates the effectiveness of modeling the dual hepatic blood supply with dynamic ^{11}C-acetate PET. Clinical data fitting results revealed that the proposed double modeling technique could successfully account for the hepatic dual-input. The presented 6-P dual-model allows more reliable estimation of the *LHMRAct*. The simulation study suggests that all the parameters of the 6-P dual-model could be estimated reliably and accurately, especially for the two HCC indicators: a_v and *LHMRAct*. Therefore, this new model structure is an appropriate representation of the system and proposes a better way for the early detection of HCC *in vivo*. Besides, with the obtainment of parameter *p*, the described modeling approach shows great potency for providing the functional physiological parametric images of the two HCC indicators.

To avoid manual placement of ROI, Chapter 7 proposes two approaches to extract the target ROIs on the dynamic ^{11}C-acetate PET images in liver

automatically. All the ROIs for the quantitative study of ^{11}C-acetate liver characteristics could be obtained by using the proposed segmentation methods. This segmentation may also be useful as a preprocessing step before fast generation of the parametric images of these two physiological parameters of the liver, which is of great value to detect HCC automatically. Additionally, the proposed segmentation methods may open a window for automatic detection of other PET studies.

8.2 Future Works

It is anticipated that the following works can be built based on the theory and the results reported in this thesis.

As stated in the previous chapters, series of quantitative studies have been conducted and state-of-the-art quantitative diagnostic information could be provided by applying series functional imaging technologies proposed in this thesis to the dynamic ^{11}C-acetate PET images in liver. In the future, more clinical data would be used to further validate our whole quantification procedure for its potential role of clinical diagnosis. The comparison between the two-step segmentation approach and the PV modeling (referred to Chapter 6) for the quantitative hepatic study using ^{11}C-acetate PET would be performed. Finally, parametric images (pixel-by-pixel based) of the two HCC indicators: the

LHMRAct and a_v would be generated in a computationally feasible way for routine clinical diagnosis.

The previous exciting outcome in this thesis is not the end of this research but the beginning for applying information techniques in oncology. In the future, suitable mathematical models for the quantification of specific characteristics of cancers to provide objective (quantitative) diagnostic information for the evaluation of a variety of cancers, such as lung cancer, prostate cancer [37] *etc*. would be developed. Lung cancer is the most frequent cancer in the world, and the prevalence of lung caner is increasing globally. The survival rate is poor, largely because lung cancer is usually diagnosed at an advanced stage. The overall 5-year survival of patients with lung cancer is approximately 14%. A cure may be achieved by surgery, which is feasible only in patients who present at an early stage and approximately 75% patients will die of recurrent diseases. The biochemical differences of FDG between normal and neoplastic tissue have resulted in its routine use for characterizing lesions that are indeterminate by conventional imaging modalities and to stage the tumors [107]-[108]. Quantification is very important for characterizing tumor kinetics, therefore further studies on computer-aided kinetic modeling describing the kinetics of FDG in lung cancer are essential. Efficient and reliable algorithms would be investigated to generate accurate quantitative physiological (parametric) images for the detection of cancer, staging and monitoring treatment of response.

Medical imaging is an essential aspect of radiological sciences for visualization of anatomical structures and metabolic information of the human

body. Structural and functional imaging of a human body is important for understanding human anatomy, function of organs and associated physiological processes. PET have been proven very promising for the evaluation of diseases far earlier, whereas lack of anatomical information to locate the disease accurately. To both identify disease earlier and anatomically localize disease to optimize therapy, a highly powerful diagnostic imaging system PET/CT was created to collect both anatomical and biological information during a single examination [109]-[112]. This integrated information permits accurate tumor detection and localization for a variety of cancers and the duration of transmission scan is much reduced with CT in place of Germanium, therefore, it is more practical to perform whole-body scan than the conventional PET-alone imaging.

Whole-Body PET/CT has recently attracted a significant amount of interest for its application in oncology providing comprehensive diagnostic information to the patient's health care team quickly, as shown in Figures 8-1 and 8-2. It has been proven very promising for the evaluation of the whole-body distribution of malignancies. We believe that quantification is very important for the proper evaluation of whole-body PET/CT particularly in characterizing tumor kinetics. Nowadays, the most commonly used method for estimating tumor metabolism is by using a semiquantitative parameter called the SUV (standardized uptake value, a decay-corrected measurement of activity per unit volume of tissue adjusted for administered activity per unit body weight). This parameter suffers from known

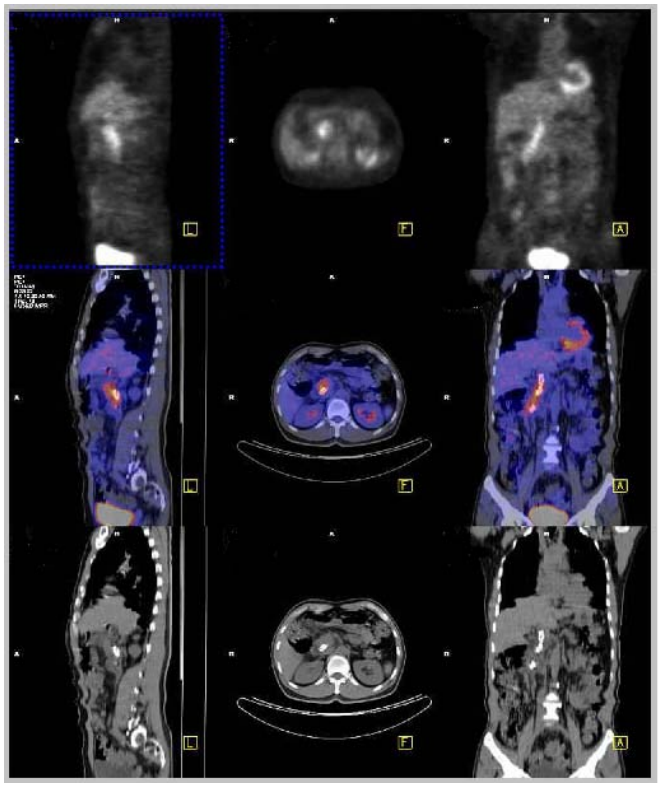

Figure 8- 1: Pancreatic carcinoma in the head of pancreas.

quantitative inaccuracies [113]. In addition, it has been reported by many clinical doctors that the measurement of SUV is less stable than the traditional PET-alone imaging. Therefore, use of the semiquantitative SUV is considered a simple but suboptimal approach for differentiating benignity from malignancy. A more rigorous approach involving accurate quantification with efficient and reliable algorithms for the detection of cancers would be investigated soon. We believe that the combined modality PET/CT technique would result in both enhanced diagnosis and identification of early response by therapy. The outcome of the continuing research would have a significant scientific and social impact.

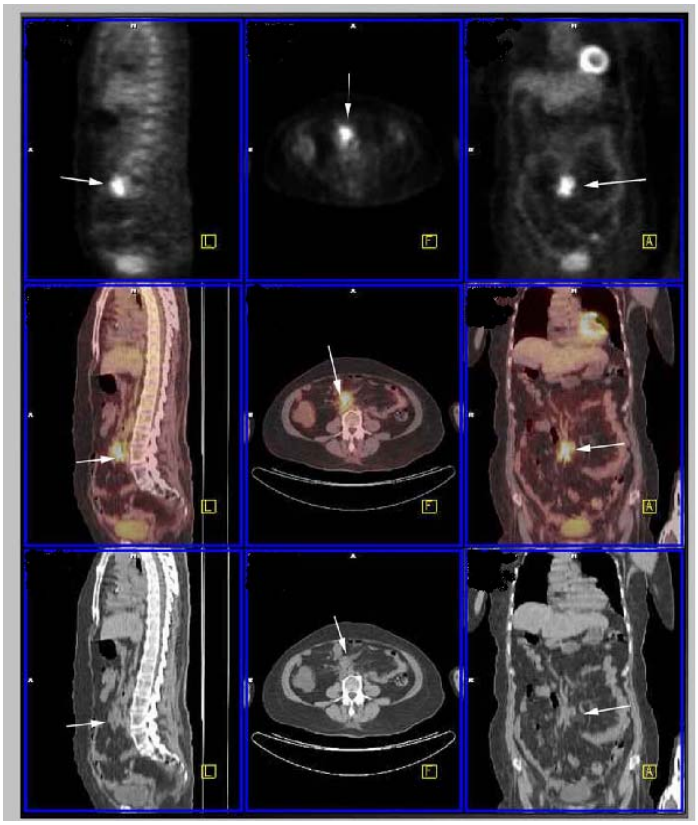

Figure 8- 2: Metastatic lymph note at the root of mesentery.

Reference

1. E. E. Kim and E. F. Jackson, *Molecular Imaging in Oncology*. Berlin Heidelberg: Springer-Verlag, 1999.
2. J. M. Ollinger and J. A. Fessler, "Positron-emission tomography," *IEEE Signal Processing Magazine*, pp. 43-55, Jan., 1997.
3. E. E. Kim, M.-C. Lee, T. Inoue, and W. H. Wong, *Clinical PET: Principles and Applications*. New York: Springer-Verlag, 2004.
4. O. L. Munk, L. Bass, K. Roelsgaard, D. Bender, S. B. Hansen, and S. Keiding, "Liver kinetics of glucose analogs measured in pigs by PET: Importance of dual-input blood sampling," *J. Nucl. Med.*, vol. 42, no. 5, pp. 795-801, 2001.
5. R. Bares and G. Lucignani, *Clinical PET*. Netherlands: Kluwer Academic Publishers, 1996.
6. C.-L. Ho, C. Yu, and D. Yeung, "^{11}C-acetate PET imaging in hepatocellular carcinoma and other liver masses," *J. Nucl. Med.*, vol. 44, no. 2, pp. 213-221, 2003.
7. D. Delbeke and C. Pinson, "^{11}C-acetate: A new tracer for the evaluation of hepatocellular carcinoma (invited commentary)," *J. Nucl. Med.*, vol. 44, no. 2, pp. 222-223, 2003.
8. M. E. Phelps, J. Mazziotta, and H. Schelbert, *Positron Emission Tomography and Autoradiography: Principles and Applications for the Brain and Heart*. New York: Raven Press, 1986.

9. M. E. Phelps, *PET: Molecular Imaging and Its Biological Applications*. New York: Springer-Verlag, 2004.
10. K. Godfrey, *Compartmental Models and Their Applications*. London: Academic Press, 1983.
11. C. Cobelli and M. P. Saccomani, "Accessible pool and system parameters: Assumptions and models," *J Parenter Enteral Nutr.*, vol. 15, pp. 45S-50S, 1991.
12. C. Cobelli, D. Foster, and G. Toffolo, *Tracer Kinetics in Biomedical Research from Data to Model*. New York: Kluwer Academic Publishers, 2000.
13. E. R. Carson, C. Cobelli, L. Finkelstein, "Modeling and identification of metabolic systems," *Am J Physiol*, vol. 240, pp. R120-129, 1981.
14. M. E. Phelps, E. J. Hoffman, C. Selin, S. C. Huang, and D. E. Kuhl, "Investigation of (F-18)2-fluoro-2-deoxyglucose for the measurement of myocardial glucose metabolism," *J. Nucl. Med.*, vol. 19, pp. 1311-1319, 1978.
15. T. Ohtake, N. Kosaka, T. Watanabe, I. Yokoyama, T. Moritan, M. Masuo, M. Iizuka, K. Kozeni, T. Momose, S. Oku, J. Nishikawa, Y. Sasaki, and M. Iio, "Noninvasive method to obtain input function for measuring tissue glucose utilization of thoracic and abdominal organs," *J. Nucl. Med.*, vol. 32, no. 7, pp. 1432-1438, 1991.
16. G. Germano, B. C. Chen, S. C. Huang, S. S. Gambhir, E. J. Hoffman, and M. E. Phelps, "Use of the abdominal aorta for arterial input function determination in hepatic and renal PET studies," *J. Nucl. Med.*, vol. 33, no. 4, pp. 613-620, 1992.

17. R. R. Raylman, J. M. Caraher, and G. D. Hutchins, “Sampling requirements for dynamic cardiac PET studies using image-derived input functions,” *J. Nucl. Med.*, vol. 34, no. 3, pp. 440-447, 1993.
18. K. Chen, D. Bandy, E. Reiman, S. C. Huang, M. Lawson, D. Feng, L. Yun, and A. Palant, “Noninvasive quantification of the cerebral metabolic rate for glucose using positron emission tomography, ^{18}F-fluoro-2-deoxyglucose, the patlak method, and an image-derived input function,” *J. Cereb. Blood Flow Metab.*, vol. 18, pp. 716-723, 1998.
19. X. Li, D. Feng, K. Lin, and S. C. Huang, “Estimation of myocardial glucose utilisation with PET using the left ventricular time-activity curve as a noninvasive input function,” *Med. Biol. Eng. Computing*, vol. 36, no. 1, pp.112-117, 1998.
20. D. M. Bates and G. W. Watt, *Nonlinear Regression Analysis and its Application*. New York: John Wiley & Sons, 1988.
21. H. El-Serag, “Epidemiology of hepatocellular carcinoma,” *Clin. Liver Dis.*, vol. 5, pp. 87-107, 2001.
22. T. Tobe, H. Kameda, M. Okudaira, M. Ohto, Y. Endo, M. Mito, E. Okamoto, K. Tanikawa, and M. Kojiro, *Primary Liver Cancer in Japan*. Tokyo, Japan: Springer-Verlag, 1992.
23. T. Tsuzuki, A. Sugioka, and M. Ueda, “Hepatic resection for hepatocellular carcinoma,” *Surgery*, vol. 107, pp. 511-520, 1990.
24. K. T. Watkins and S. A. Curley , “Liver and bile ducts,” in *Clinical Oncology*, 2nd ed, M. D. Abeloff, J. O. Armitage, A. S. Lichter, and J. E. Niederhuber, Eds. Harcourt Asia: Science Press, 2000, pp. 1681-1748.

25. S. Okazumi, K. Isono, K. Enomoto, T. Kikuchi, M. Ozaki, H. Yamamoto, H. Hayashi, T. Asano, and M. Ryu, “Evaluation of liver tumors using fluorine-18-fluorodeoxyglucose PET: Characterization of tumor and assessment of effect of treatment,” *J. Nucl. Med.*, vol. 33, no. 3, pp. 333-339, 1992.
26. M. A. Brown, D. W. Myears, and S. R. Bergmann, “Validity of estimates of myocardial oxidative metabolism with Carbon-11 acetate and positron emission tomography despite altered patterns of substrate utilization,” *J. Nucl. Med.*, vol. 30, no. 2, pp. 187-193, 1989.
27. C. G. Henes, S. R. Bergmann, M. N. Walsh, B. E. Sobel, and E. M. Geltman, “Assessment of myocardial oxidative metabolic reserve with positron emission tomography and Carbon-11 acetate,” *J. Nucl. Med.*, vol. 30, no. 9, pp. 1489-1499, 1989.
28. M. N. Walsh, E. M. Geltman, M .A. Brown, C. G. Henes, C. J. Weinheimer, B. E. Sobel, and S. R. Bergmann, “Noninvasive estimation of regional myocardial oxygen consumption by positron emission tomography with Carbon-11 acetate in patients with myocardial infarction,” *J. Nucl. Med.*, vol. 30, no. 11, pp. 1798-1808, 1989.
29. J. Kotzerke, R. J. Hicks, E. Wolfe, W. H. Herman, E. Molina, D. E. Kuhl, and M. Schwaiger, “Three-dimensional assessment of myocardial oxidative metabolism: A new approach for regional determination of PET-derived Carbon-11-acetate kinetics,” *J. Nucl. Med.*, vol. 31, no. 11, pp. 1876-1893, 1990.
30. A. Buck, H. G. Wolpers, G. D. Hutchins, V. Savas, T. J. Managner, N. Nguyen, and M. Schwaiger, “Effect of carbon-11-acetate recirculation on

estimates of myocardial oxygen consumption by PET," *J. Nucl. Med.*, vol. 32, no. 10, pp. 1950-1957, 1991.

31. R. J. Gropler, B. A. Siegel, and E. M. Geltman, "Myocardial uptake of carbon-11-acetate as an indirect estimate of regional myocardial blood flow," *J. Nucl. Med.*, vol. 32, no. 2, pp. 245-251, 1991.
32. T. Torizuka, N. Tamaki, K. Kasagi, T. Misaki, M. Kawamoto, E. Tadamura, Y. Magata, Y. Yonekura, T. Mori, and J. Konishi, "Myocardial oxidative metabolism in hyperthyroid patients assessed by PET with carbon-11-acetate," *J. Nucl. Med.*, vol. 36, no. 11, pp. 1981-1986, 1995.
33. J. Hoff, W. Burchert, H. G. Wolpers, G. J. Meyer, and H. Hundeshagen, "A kinetic model for cardiac PET with [1-Carbon-11]-acetate", *J. Nucl. Med.*, vol. 37, no. 3, pp. 521-529, 1996.
34. K. T. Sun, K. Chen, S. C. Huang, D. B. Buxton, H. W. Hansen, A. S. Kim, S. Siegel, Y. Choi, P. Muller, M. E. Phelps and H. R. Schelbert, "Compartment model for measuring myocardial oxygen consumption using [1-^{11}C] acetate," *J. Nucl. Med.*, vol. 38, no. 3, pp. 459-466, 1997.
35. K. T. Sun, L. A. Yeatman, D. B. Buxton, K. Chen, J. A. Johnson, S. C. Huang, K. F. Kofoed, S. Weismueller, J. Czernin, M. E. Phelps, and H. R. Schelbert, "Simultaneous measurement of myocardial oxygen consumption and blood flow using [1-carbon-11]acetate," *J. Nucl. Med.*, vol. 39, no. 2, pp. 272-280, 1998.
36. R. R. Sciacca, O. Akinboboye, R. L. Chou, S. Epstein, and S. R. Bergmann, "Measurement of myocardial blood flow with PET using 1-^{11}C-acetate," *J. Nucl. Med.*, vol. 42, no. 1, pp. 63-70, 2001.

37. N. Oyama, H. Akino, H. Kanamaru, Y. Suzuki, S. Muramoto, Y. Yonekura, N. Sadato, K. Yamamoto, and K. Okada, "^{11}C-acetate PET imaging of prostate cancer," *J. Nucl. Med.*, vol. 43, no. 2, pp. 181-186, 2002.

38. D. Feng, S. C. Huang, and X. Wang, "Models for computer simulation studies of input functions for tracer kinetic modeling with positron emission tomography," *Int. J. Biomed. Computing*, vol. 32, pp. 95-110, 1993.

39. D. Feng, K. P. Wong, C. M. Wu, and W. C. Siu, "A technique for extracting physiological parameters and the required input function simultaneously from PET image measurements: Theory and simulation study," *IEEE Trans. Inform. Technol. Biomed.*, vol. 1, no. 4, pp. 243-254, 1997.

40. K. P. Wong, D. Feng, S. R. Meikle, and M. J. Fulham, "Simultaneous estimation of physiological parameters and the input function: In-vivo PET data," *IEEE Trans. Inform. Technol. Biomed.*, vol. 5, no. 1, pp. 67-76, 2001.

41. K. Chen, D. Bandy, E. Reiman, S. C. Huang, M. Lawson, D. Feng, L. Yun, and A. Palant, "Noninvasive quantification of the cerebral metabolic rate for glucose using positron emission tomography, ^{18}F-fluoro-2-deoxyglucose, the patlak method, and an image-derived input function," *J. Cereb. Blood Flow Metab.*, vol. 18, pp. 716-723, 1998.

42. R. R. Raylman, J. M. Caraher, and G. D. Hutchins, "Sampling requirements for dynamic cardiac PET studies using image-derived input functions," *J. Nucl. Med.*, vol. 34, no. 3, pp. 440-447, 1993.

43. X. Li, D. Feng, K. Lin, and S. C. Huang, "Estimation of myocardial glucose utilisation with PET using the left ventricular time-activity curve as a noninvasive input function," *Med. Biol. Eng. Computing*, vol. 36, no. 1, pp.112-117, 1998.

44. D. Feng, X. Li, and S. C. Huang, "A new double modeling approach for dynamic cardiac PET studies using noise and spillover contaminated LV measurements," *IEEE Trans. Biomed. Eng.*, vol. 43, no. 3, pp. 319-327, 1996.

45. L. P. Dartner and J. L. Hiatt, *Color textbook of histology*. Philadelphia: Saunders, 1997.

46. C. E. Shonk, H. P. Morris, and G. E. Boxer, "Patterns of glycolytic enzymes in rat liver and hepatoma," *Cancer Res.*, vol. 25**,** pp. 671-676, 1965.

47. L. Sokoloff, M. Reivich, C. Kennedy, M. H. Des Rosiers, C. S. Patlak, K. D. Pettigrew, O. Sakurada, and M. Shinohara, "The [^{14}C] Deoxyglucose method for the measurement of local cerebral glucose utilization: Theory, procedure, and normal values in the conscious and anesthetized albino rat," *J. Neurochem.*, vol. 28, pp. 897-916, 1977.

48. M. E. Phelps, S. C. Huang, E. J. Hoffman, C. Selin, L. Sokoloff, and D. E. Kuhl, "Tomographic measurement of local cerebral glucose metabolic rate in humans with (F-18)2-Fluoro-2-Deoxy-D-Glucose: Validation of method," *Ann. Neurol.*, vol. 6, pp. 371-388, 1979.

49. S. C. Huang, M. E. Phelps, E. J. Hoffman, K. Sideris, C. J. Selin, and D. E. Kuhl, "Noninvasive determination of local cerebral metabolic rate of glucose in man," *Amer. J. Physiol.*, vol. 238, pp. E69-E82, 1980.

50. L. Stryer, *Biochemistry*, 4th ed. New York: Freeman, 1995, pt. III, ch. 20.

51. M. Yoshimoto *et al.*, "Characterization of acetate metabolism in tumor cells in relation to cell proliferation: Acetate metabolism in tumor cells," *Nucl. Med. Biol.*, vol. 28, pp. 117-122, 2001.

52. H. Akaike, “A new look at the statistical model identification,” *IEEE Trans. Automat. Contr.*, AC-19, pp. 716-723, 1974.

53. G. Schwarz, “Estimating the dimension of a model,” *Ann. Statist.*, vol. 6, pp. 461-564, 1978.

54. C. S. Patlak, R. G. Blasberg, and J. D. Fenstermacher, “Graphical evaluation of blood-to-brain transfer constants from multiple-time uptake data,” *J. Cereb. Blood Flow Metab.*, vol. 3, pp. 1-7, 1983.

55. S. Chen, C. Ho, D. Feng, and Z. Chi, “Tracer kinetic modeling of ^{11}C-acetate applied in the liver with positron emission tomography,” *IEEE Trans. Med. Imag.*, vol. 23, no. 4, pp. 426-432, 2004.

56. C. Bartolozzi and R. Lencioni, *Liver Malignancies: Diagnostic and Interventional Radiology*. Berlin, Germany: Springer-Verlag, 1999.

57. D. L. Morris, C. S. McArdle, and G. M. Onik, *Hepatic Metastases: Diagnosis and Management.* Bath, U.K.: The Bath Press, 1996.

58. H.-M. Hoogewoud, *Hepatocellular Carcinoma and Liver Metastases: Diagnosis and Treatment*. Berlin, Germany: Springer-Verlag, 1993. A. Rohner.

59. W. W. Lautt and C. V. Greeway, “Conceptual review of the hepatic vascular bed,” *Hepatology*, vol. 7, pp. 952-963, 1987.

60. W. H. H. Andrews, *Liver*. London, U.K.: Edward Arnold, 1979.

61. C. Breedis and G. Young, “The blood supply of neoplasms in the liver,” *Amer. J. Pathol.* vol. 30, pp. 969-985, 1954.

62. G. Lin *et al.*, “Postmortem examination of the blood supply and vascular pattern of small liver metastases in man,” *Surgery*, vol. 96, pp. 517-526, 1984.

63. R. Sarper *et al.*, "A noninvasive method for measuring portal venous/total hepatic blood flow by hepatosplenic radionuclide angiography," *Radiology*, vol. 141, pp. 179-184, 1981.

64. M. K. O'Connor, P. MacMathuna, and P. W. N. Keeling, "Hepatic arterial and portal venous components of liver blood flow: A dynamic scintigraphic study," *J. Nucl. Med.*, vol. 29, no. 4, pp. 466-472, 1988.

65. S. Shiomi, T. Kuroki, O. Kurai, K. Kobayashi, N. Ikeoka, T. Monna, and H. Ochi, "Portal circulation by Technetium-99m pertechnetate per-rectal portal scintigraphy," *J. Nucl. Med.*, vol. 29, no. 4, pp. 460-465, 1988.

66. J. Martin-Comin, J. Mora, J. Figueras, R. Puchal, E. Jaurrieta, F. Badosa, and M. Ramos, "Calculation of portal contribution to hepatic blood flow with ^{99m}Tc-microcolloids. A noninvasive method to diagnose liver graft rejection," *J. Nucl. Med.*, vol. 29, no. 11, pp. 1776-1780, 1988.

67. B. C. Chen, S. C. Huang, G. Germano, W. Kuhle, R. A. Hawkins, D. Buxton, R. C. Brunken, H. R. Schelbert, and M. E. Phelps, "Noninvasive quantification of hepatic arterial blood flow with nitrogen-13-ammonia and dynamic positron emission tomography," *J. Nucl. Med.*, vol. 32, no. 12, pp. 2199-2206, 1991.

68. J. Correia, "Editorial: A bloody future for clinical PET," *J. Nucl. Med.*, vol. 33, pp. 620-622, 1992.

69. S. Chen, L. Wong, and D. Feng, "A new automatic detection approach for hepatocellular carcinoma using ^{11}C-acetate positron emission tomography," in *Proc. IEEE Int. Conf. Image Processing*, Barcelona, Spain, Sept. 14-17, 2003, pp. 1065-1068.

70. D. Feng, “Information technology applications in biomedical functional imaging,” *IEEE Trans. Inform. Technol. Biomed.*, vol. 3, no. 3, pp. 221-230, 1999.

71. D. Ho and D. Feng, “Rapid algorithms for the construction of cerebral blood flow and oxygen utilization images with oxygen-15 and dynamic positron emission tomography,” *Computer Methods and Programs in Biomedicine*, vol. 58, pp. 99-117, 1999.

72. D. Feng and W. Cai, “Bound generalized linear least square (B-GLLS) algorithm for parametric imaging with PET,” *Proc. 4th IFAC Biomedical Symposium on Modeling & Control in Biomedical Systems*, Karlsburg/Greifswald, Germany, March 30-April 1, 2000, pp.327-329.

73. K.-P. Wong, D. Feng, and W.C. Siu, “Generalized linear least squares algorithm for non-uniformly sampled biomedical system identification with possible repeated eigenvalues,” *Computer Methods and Programs in Biomedicine*, vol. 57, pp. 167-177, 1998.

74. D. Feng, S. C. Huang, Z. Wang, and D. Ho, “An unbiased parametric imaging algorithm for nonuniformly sampled biomedical system parameter estimation,” *IEEE Trans. Med. Imag.*, vol. 15, no. 4, pp. 512-518, 1996.

75. K.-P. Wong, D. Feng, “Fast system identification algorithm for non-uniformly sampled noisy biomedical signal,” *Proc. IEEE Region Ten Conference*, Perth, Australia, Nov 27-29, 1996, pp. 559-564.

76. H. Unbehauen and G. P. Rao, *Identification of Continuous Systems*. Amsterdam, the Netherlands: North-Holland, 1987.

77. G. C. Goodwin and R. L. Payne, *Dynamic System Identification: Experiment Design and Data Analysis*. New York: Academic, 1977.

78. D. Feng, D. Ho, K. K. Lau, and W. C. Siu, "GLLS for optimally sampled continuous dynamic system modeling: Theory and algorithm," *Computer Methods and Programs in Biomedicine*, vol. 59, pp. 31-43, 1999.

79. Y. L. Yamamoto, C. J. Thompson, E. E. Meyer, J. S. Robertson, and W. Feindel, "Dynamic positron emission tomography for study of cerebral hemodynamics in a cross section of the head using positron emitting ^{68}Ga-EDTA and ^{77}Kr," *J. Comput. Assist. Tomogr.*, vol. 1, pp. 43-56, 1977.

80. K. Chen, M. Lawson, E. Reiman, A. Cooper, D. Feng, S. C. Huang, D. Bandy, D. Ho, L. Yun, and A. Palant, "Generalized linear least squares method for fast generation of myocardial blood flow parametric images with N-13 Ammonia PET," *IEEE Trans. Med. Imag.*, vol. 17, no. 2, pp. 236-243, 1998.

81. S. C. Huang, R. E. Carson, and M. E. Phelps, "Measurement of local blood flow and distribution volume with short-lived isotopes: A general input technique," *J. Cereb. Blood Flow Metab.*, vol. 2, pp. 99-108, 1982.

82. R. E. Carson, S. C. Huang, and M. V. Green, "Weighted integration method for local cerebral blood flow measurements with positron emission tomography," *J. Cereb. Blood Flow Metab.*, vol. 6, pp. 245-258, 1986.

83. S. Chen, D. Feng, "Noninvasive quantification of the differential portal and arterial contribution to the liver blood supply from PET measurements using ^{11}C-acetate kinetic model," *IEEE Trans. Bio. Engi.*, vol. 51, no. 9, pp.1579-1585, 2004.

84. H. Minn, S. Leskinen-Kallio, P. Lindholm, J. Bergman, U. Ruotsalainen, M. Teras, and M. Haaparanta, "[^{18}F]Fluorodeoxyglucose uptake in tumors:

Kinetic vs. steady-state methods with reference to plasma insulin," *J. Comput. Assist. Tomogr.*, vol. 17, no. 1, pp. 115-123, 1993.

85. T. Torizuka, N. Tamaki, T. Inokuma, Y. Magata, Y. Yonekura, A. Tanaka, Y. Yamaoka, K. Yamamoto, and J. Konishi, "Value of fluorine-18-FDG-PET to monitor hepatocellular carcinoma after interventional therapy," *J. Nucl. Med.*, vol. 35, no. 12, pp. 1965-1969, 1994.
86. H. Iida, P. M. Bloomfield, S. Miura, I. Kanno, M. Murakami, K. Uemura, M. Amano, K. Tanaka, Y. Hirose, and S. Yamamoto, "Effect of real-time weighted integration system for rapid calculation of functional images in clinical positron emission tomography," *IEEE Trans. Med. Imag.*, vol. 14, no. 1, pp. 116-121, 1995.
87. D. Feng, Z. Wang, and S.-C. Huang, "A study on statistically reliable and computational efficient algorithms for generating local cerebral blood flow parametric images with positron emission tomography," *IEEE Trans. Med. Imag.*, vol. 12, no. 2, pp. 182-188, 1993.
88. D. Feng, D. Ho, K. Chen, L.-C Wu, J.-K. Wang, R.-S. Liu, and S.H. Ueh, "An evaluation of the algorithms for determining local cerebral metabolic rages of glucose using positron emission tomography dynamic data," *IEEE Trans. Med. Imag.*, vol. 14, no. 4, pp. 697-710, 1995.
89. T. Torizuka, N. Tamaki, T. Inokuma, Y. Magata, S. Sasayama, Y. Yonekura, A. Tanaka, Y. Yamaoka, K. Yamamoto, and J. Konishi, "In vivo assessment of glucose metabolism in hepatocellular carcinoma with FDG-PET," *J. Nucl. Med.*, vol. 36, no. 10, pp. 1811-1817, 1995.
90. G. Brix, S. I. Ziegler, M. E. Bellemann, J. Doll, R. Schosser, R. Lucht, H. Krieter, D. Nosske, and U. Haberkorn, "Quantification of [^{18}F]FDG uptake

in the normal liver using dynamic PET: Impact and modeling of the dual hepatic blood supply," *J. Nucl. Med.*, vol. 42, no. 8, pp. 1265-1273, 2001.

91. Y. Choi, R.A. Hawkins, S.C. Huang, R.C. Brunken, C.K. Hoh, C. Messa, E.U. Nitzsche, M.E. Phelps, and H.R. Schelbert, "Evaluation of the effect of glucose ingestion and kinetic model configurations of FDG in the normal liver," *J. Nucl. Med.*, vol. 35, no. 5, pp. 818-823, 1994
92. L. N. Weinberg, S. C. Huang, E. J. Hoffman, L. Araujo, C. Nienaber, M. GroverMcKay, M. Dahlbom, and H. Schelbert, "Validation of PET-acquired input functions for cardiac studies," *J. Nucl. Med.*, vol. 29, no. 2, pp. 241-247, 1988.
93. L. M. Wahl, M.-C. Asselin, and C. Nahmias, "Regions of interest in the venous sinuses as input functions for quantitative PET," *J. Nucl. Med.*, vol. 40, no. 10, pp. 1666-1675, 1999.
94. H. Iida, C. G. Rhodes, R. Silva, L. I. Araujo, P. M. Bloomfield, A. A. Lammertsma, and T. Jones, "Use of the left ventricular time-activity curve as a noninvasive input function in dynamic oxygen-15-water positron emission tomography," *J. Nucl. Med.*, vol. 33, no. 9, pp. 1669-1677, 1992.
95. H.-M. Wu, C. K. Hoh, Y. Choi, H. R. Schelbert, R. A. Hawkins, M. E. Phelps and S.-C. Huang, "Factor analysis for extraction of blood time-activity curves in dynamic FDG-PET studies," *J. Nucl. Med.*, vol. 36, no. 9, pp. 1714-1721, 1995.
96. M. Naganawa, Y. Kimura, and A. Matani, "Modification of ICA for extracting blood vessel-related component in nuclear medicine: Contrast function and nonnegative constraints," *Proc. the 4th International*

Symposium on Independent Component Analysis and Blind Signal Separation (ICA2003), pp. 65-70.

97. M. I. Gurelli and C. L. Nikias, "EVAM: an eigenvector-based algorithm for multichannel blind deconvolution of input colored signals," *IEEE Trans. Sign. Proc.*, vol. 43, no. 1, pp. 134-149, 1995.
98. A. M. Peters and M. J. Myers, *Physiological Measurements with Radionuclides in Clinical Practice*. Oxford, U. K.: Oxford University Press, 1998.
99. J. O. Rowan, *Physics and the Circulation*. Bristol, U. K.: Adam Hilger Ltd, 1981.
100. S. Chen and D. Feng, "Novel parameter estimation methods for ^{11}C-acetate dual-input liver model with dynamic PET," 2nd revision resubmitted to *IEEE Trans. Bio. Engi.*, July, 2005.
101. K. P. Wong, D. Feng, S. R. Meikle, and M. J. Fulham, "Segmentation of dynamic PET images using cluster analysis," *IEEE Trans. Nucl. Sci.*, vol. 49, no. 1, pp. 200-207, 2002.
102. J. A. Hartigan, *Clustering Algorithms*. New York, U.S.A.: Wily, 1975.
103. F. O' Sullivan, "Imaging radiotracer model parameters in PET: A mixture analysis approach," *IEEE Trans. Med. Imag.*, vol. 12, pp. 399-412, 1993.
104. D. Ho, D. Feng, and K. Chen, "Dynamic image data compression in spatial and temporal domains: Theory and algorithm," *IEEE Trans. Info. Tech. Biomed.*, vol. 1, pp. 219-228, 1997.
105. Y. Kimura, H. Hsu, H. Toyama, M. Senda, and N. M. Alpert, "Improved signal-to-noise ratio in parametric images by cluster analysis," NeuroImage, vol. 9, pp. 554-561, 1999.

106. H. Guo, R. Renaut, K. Chen, and E. Reiman, "Clustering huge data sets for parametric PET imaging," *Biosystems*, vol. 71, pp. 81-92, 2003.

107. T. Inoue *et al.*, "Detecting recurrent or residual lung caner with FDG-PET," *J. Nucl. Med.*, vol. 36, pp. 788-793, 1995.

108. R. J. Hicks *et al.*, "^{18}F-FDG-PET provides high-impact and powerful prognostic stratification in staging newly diagnosed non-small cell lung cancer," *J. Nucl. Med.*, vol. 42, pp. 1596-1604, 2001.

109. R. Bar-Shalom, N. Yefremov, L. Guralnik, D. Gaitini, A. Frenkel, A. Kuten, H. Altman, Z. Keidar, and O. Israel, "Clinical performance of PET/CT in evaluation of cancer: Additional value for diagnostic imaging and patient management," *J. Nucl. Med.*, vol. 44, no. 8, pp. 1200-1209, 2003.

110. B. Bagheri. A. H. Maurer, L. Cone, M. Doss, and L. Adler, "Characterization of the normal adrenal gland with ^{18}F-FDG PET/CT," *J. Nucl. Med.*, vol. 45, no. 8, pp. 1340-1343, 2004.

111. O. Mawlawi, D. A. Podoloff, S. Kohlmyer, J. J. Williams, C. W. Stearns, R. F. Culp, and H. Macapinlac, "Performance characteristics of a newly developed PET/CT scanner using NEMA standards in 2D and 3D modes," *J. Nucl. Med.*, vol. 45, no. 10, pp. 1734-1742, 2004.

112. E. M. Kamel, M. Thumshirn, K. Truninger, M. Schiesser, M. Fried, B. Padberg, D. Schneiter, S. J. Stoeckli, G. K. von Schulthess, and K. D. M. Stumpe, "Significance of incidental ^{18}F-FDG accumulations in the gastrointestinal tract in PET/CT: Correlation with endoscopic and histopathologic results," *J. Nucl. Med.*, vol. 45, no. 11, pp. 1804-1810, 2004.

113. S. K. Sundaram, N. M. T. Freedman, J. A. Carrasquillo, J. M. Carson, M. Whatley, S. K. Libutti, D. Sellers, and S. L. Bacharach, "Simplified kinetic

analysis of tumor ^{18}F-FDG uptake: A dynamic approach," *J. Nucl. Med.*, vol. 45, no. 8, pp. 1328-1333, 2004.